1-1-2013

A Multidisciplinary Analysis of Evaporite Rocks from the Mid-Neoproterozoic Browne Formation, Officer Basin, Western Australia

Natalie Spear
University of Pennsylvania, natalie.nahill@gmail.com

A Multidisciplinary Analysis of Evaporite Rocks from the Mid-Neoproterozoic Browne Formation, Officer Basin, Western Australia

Abstract
During Neoproterozoic time an irreversible increase in the oxygen levels present in Earth's atmosphere resulted in the emergence of complex life forms at the end of Proterozoic time. The processes whereby this increase in oxygen occurred has not been explained. To begin to understand the reasons for this rise in oxygen concentration, we must study the global cycles of carbon, oxygen, and sulfur, which are inextricably linked. I studied the ~830 Ma Browne Formation of the Officer Basin, Western Australia to reconstruct the marine chemistry, the sulfur cycle, and the depositional environment during this enigmatic period in geologic history.

I performed a petrographic study of the Browne Formation using optical and electron microscopy (SEM-EDS) and X-ray diffraction (XRD). To document the marine origin of the Browne Formation evaporites, I measured the bromine content of several rock-salt samples using X-Ray Fluorescence. The Browne Formation was deposited within an extensive, subcontinental-scale shallow saline system, or "saline giant", a geologic province not represented on Earth today.

I present the first direct characterization of seawater chemistry from the Mid-Neoproterozoic, and can thus impose a tighter constraint on the much-debated level of oceanic sulfate than has been possible heretofore. My results extend documentation of seawater chemistry by ~300 Ma, and hence represent chemical characterization of the oldest seawater ever measured by fluid-inclusion analysis. I analyzed primary fluid inclusions in primary halite using the CRYO-SEM-EDS technique. The major-ion composition of mid-Neoproterozoic seawater was very different from present-day seawater chemistry; the concentration of Ca^{2+} exceeded that of SO_4^{2-}, such as it did in Cambrian, Silurian, Devonian, Jurassic, and Cretaceous seawater.

From a review of the literature describing the isotopic composition of marine sulfate for this Mid-Neoproterozoic time, and using the same petrographic and sedimentologic criteria I applied to my samples, I was able to narrow the known range of isotopic data on seawater sulfate for this period of time. I measured the isotopic composition of marine sulfur from primary anhydrite crystals associated with primary halite using a Mass Spectrometer (Finnigan MAT CHN 1108 Analyzer).

My research offers far-reaching implications concerning Proterozoic marine-sulfate and oxygen levels, and the chemical co-evolution of the early oceans, atmosphere, and biosphere. These data make it possible to explore the relationships between major-ion chemistry of seawater and the evolution of marine life during this important interval of Earth history.

Degree Type
Dissertation

Degree Name
Doctor of Philosophy (PhD)

Graduate Group
Earth & Environmental Science

A MULTIDISCIPLINARY ANALYSIS OF EVAPORITE ROCKS FROM THE MID-NEOPROTEROZOIC BROWNE FORMATION, OFFICER BASIN, WESTERN AUSTRALIA

Natalie Spear

A DISSERTATION

in

Earth and Environmental Science

Presented to the Faculties of the University of Pennsylvania

in

Partial Fulfillment of the Requirements for the

Degree of Doctor of Philosophy

2013

Supervisor of Dissertation

_____

Dr. Robert Giegengack, Professor, Earth and Environmental Science

Graduate Group Chairperson

_____

Dr. Art Johnson, Professor, Earth and Environmental Science

Dissertation Committee

Dr. Hermann Pfefferkorn, Professor, Earth and Environmental Science

Dr. Tim Lowenstein, Professor, Professor of Geology, Binghamton University

A MULTIDISCIPLINARY ANALYSIS OF EVAPORITE ROCKS FROM THE MID-NEOPROTEROZOIC BROWNE FORMATION, OFFICER BASIN, WESTERN AUSTRALIA

DEDICATION

This work is dedicated to the memory of Dick Holland who was one of the most interesting, intriguing, and inspiring people I have had the pleasure of knowing. Dick not-so-gently nudged me towards this project and line of research, for which I am grateful. I deeply miss our lunches where I left feeling slightly smarter while simultaneously realizing how little I really knew.

And

To my Mom. Greatest. Mom. Ever.

ACKNOWLEDGMENTS

I must begin with my adviser, Dr. Bob Giegengack. Gieg, your field course in Montana set me on a path for which I will be forever grateful. You've given me freedom to explore my interests, provided me with plenty of new ones, and sent me around the world in the process. It is hard to explain the importance of your influence in my life but it lies somewhere between that of a fairy godmother and Santa Claus. Thanks.

I owe many thanks to Dr. Tim Lowenstein. You have been an incredibly supportive mentor. I've learned so much from your classes, field excursions, and chats over beer. Thanks for adopting me into your Binghamton crew.

I am also appreciative of the insights and discussions provided by Dr. Hermann Pfefferkorn, Dr. Ken Lande, Dr. Gomaa Omar, and Dr. Ed Doheny.

A very special thanks to my collaborator Dr. Javier García-Veigas. Thank you for being a kind and gentle editor and a patient teacher.

This research was supported by grants form the National Science Foundation and the Geological Society of America. Support for analytical work was provided by the project CGL-2009-11096 of the Spanish Government. Additional sources of support include the Greg and Susan Walker Endowment and the University of Pennsylvania's Benjamin Franklin Fellowship.

Joan Buccilli and Arlene Mand – thank you for being the sources for all information and making things happen.

I would like to thank Mike Timofeeff for sharing his time and creative approaches to extracting tiny bits of fluid from halite; Alexandra Krull Davatzes at Temple University for the generous use of her microscopes; Kath Grey for her enlightening hospitality and insights on Proterozoic Australia; and Heide Peters for passing her samples on to me.

And lastly my family…To Maggie - thanks for taking care of Weston so I could work. To Mum Mum and Mike – thanks for being proud of me. To Mom, Phil, Danielle, and Ellise – thanks for being my field assistants, my childcare, my confidantes, and the best family ever. To Jeff, Weston, and baby Spear – thanks for being patient while I finished this and thanks for making my life such a happy and complete one.

ABSTRACT

A MULTIDISCIPLINARY ANALYSIS OF EVAPORITE ROCKS FROM THE MID-NEOPROTEROZOIC BROWNE FORMATION, OFFICER BASIN, WESTERN AUSTRALIA

Natalie Spear

Dr. Robert Giegengack

During Neoproterozoic time an irreversible increase in the oxygen levels present in Earth's atmosphere resulted in the emergence of complex life forms at the end of Proterozoic time. The processes whereby this increase in oxygen occurred has not been explained. To begin to understand the reasons for this rise in oxygen concentration, we must study the global cycles of carbon, oxygen, and sulfur, which are inextricably linked. I studied the ~830 Ma Browne Formation of the Officer Basin, Western Australia to reconstruct the marine chemistry, the sulfur cycle, and the depositional environment during this enigmatic period in geologic history.

I performed a petrographic study of the Browne Formation using optical and electron microscopy (SEM-EDS) and X-ray diffraction (XRD). To document the marine origin of the Browne Formation evaporites, I measured the bromine content of several rock-salt samples using X-Ray Fluorescence. The Browne Formation was deposited within an extensive, subcontinental-scale shallow saline system, or "saline giant", a geologic province not represented on Earth today.

I present the first direct characterization of seawater chemistry from the Mid-Neoproterozoic, and can thus impose a tighter constraint on the much-debated level of oceanic sulfate than has been possible heretofore. My results extend documentation of seawater chemistry by ~300 Ma, and hence represent chemical characterization of the oldest seawater ever measured by fluid-inclusion analysis. I analyzed primary fluid inclusions in primary halite using the CRYO-SEM-EDS technique. The major-ion composition of mid-Neoproterozoic

seawater was very different from present-day seawater chemistry; the concentration of Ca^{2+} exceeded that of SO_4^{2-}, such as it did in Cambrian, Silurian, Devonian, Jurassic, and Cretaceous seawater.

From a review of the literature describing the isotopic composition of marine sulfate for this Mid-Neoproterozoic time, and using the same petrographic and sedimentologic criteria I applied to my samples, I was able to narrow the known range of isotopic data on seawater sulfate for this period of time. I measured the isotopic composition of marine sulfur from primary anhydrite crystals associated with primary halite using a Mass Spectrometer (Finnigan MAT CHN 1108 Analyzer).

My research offers far-reaching implications concerning Proterozoic marine-sulfate and oxygen levels, and the chemical co-evolution of the early oceans, atmosphere, and biosphere. These data make it possible to explore the relationships between major-ion chemistry of seawater and the evolution of marine life during this important interval of Earth history.

Table of Contents

LIST OF TABLES

LIST OF FIGURES

CHAPTER TWO

CHAPTER 3

CHAPTER 4

CHAPTER 1: INTRODUCTION

1.1 RESEARCH GOALS

The goal of this research is to reconstruct the chemistry of Neoproterozoic seawater and to refine the isotopic signature of seawater sulfate for this period in geologic history. To do so, I obtained samples from the Mid-Neoproterozoic Browne Formation from the Empress 1A and Lancer 1 cores, both from the western part of the Officer Basin, Western Australia. First, I determined that the halite of the Browne Formation is a primary marine halite and was suitable for my research goals. This work is described in chapter 1: "The sedimentology, depositional environment, and inflow waters of a Mid-Neoproterozoic saline "giant": the Browne Formation Evaporites, Officer Basin, Western Australia". Another goal of chapter 1 was to describe the environment and depositional conditions of the Officer Basin, and to compare the sedimentary environment of the Officer Basin with the coeval evaporite Amadeus Basin of Western and Northern Australia. There are no modern analogs of the ancient saline giants that these basins represent.

Based on my work described in chapter 1, I selected samples of primary halite that contained Mid-Neoproterozoic seawater trapped in primary fluid inclusions. In chapter 2, entitled "Evidence from fluid inclusions extends the record of seawater chemistry by ~300 Million years from ~544 Ma to 830 Ma", I present the first direct measurements of Neoproterozoic seawater chemistry. Until these measurements were made, our direct understanding of seawater chemistry began with fluid-inclusion data from the ~544 Ma Ara Formation evaporites in Oman. With the results from the ~830 Ma Browne Formation fluid inclusions, I have extended our knowledge of seawater chemistry by ~300 Ma, and I have constrained the much-debated seawater-sulfate values for this period of geologic time.

The halite of the Browne Formation contains primary anhydrite crystals that contain an unaltered isotopic signature of seawater sulfate. From these primary anhydrite crystals, I determined the $\delta^{34}S$ composition of Mid-Neoproterozoic seawater sulfate. It is difficult to interpret

the isotopic results from samples of this age because of the long post-depositional history about which we know very little. Using the petrographic and sedimentologic data I acquired for the samples I studied, I evaluated the published data for evaporite samples that were altered by diageneitic processes or that were not demonstrated to be of marine origin. This allowed me to refine the range of plausible values for the isotopic composition of Mid-Neoproterozoic seawater sulfate. I present this work in chapter 3, entitled: "Re-evaluation of the δ^{34}S-isotopic composition of marine sulfates from Mid-Neoproterozoic Evaporites: New data from the Browne Formation (~830 Ma), Officer Basin, Australia".

1.2 DISSERTATION STRUCTURE

Each chapter is written following the guidelines for the journal to which I intended to submit that chapter for publication. The first chapter, "The sedimentology, depositional environment, and inflow waters of a Mid-Neoproterozoic saline "giant": the Browne Formation Evaporites, Officer Basin, Western Australia" is written for the journal *Precambrian Research*. The second chapter, "Evidence from fluid inclusions extends the record of seawater chemistry by ~300 Million years from ~544 Ma to 830 Ma", was submitted to *Geology*. The third chapter, "Re-evaluation of the δ^{34}S-isotopic composition of marine sulfates from Mid-Neoproterozoic Evaporites: New data from the Browne Formation (~830 Ma), Officer Basin, Australia", will be submitted to *Chemical Geology*. Due to restrictions set forth by those journals, the sections containing my research methods and data in all three chapters are abbreviated; therefore, in Appendix I I have included expanded descriptions of my research method, and in Appendix II I have included my full dataset.

CHAPTER 2: THE SEDIMENTOLOGY, DEPOSITIONAL ENVIRONMENT, AND INFLOW WATERS OF A MID-NEOPROTEROZOIC SALINE "GIANT": THE BROWNE FORMATION EVAPORITES, OFFICER BASIN, WESTERN AUSTRALIA

2.1 ABSTRACT

Ancient evaporite deposits contain a wealth of information pertaining to paleogeography and seawater chemistry and can be used to make inferences regarding paleoclimatic conditions. By comparing ancient evaporite deposits with modern evaporites, we can distinguish primary syndepositional features, which house valuable information about the depositional environment, from post-burial features, which contain information about the subsurface burial environment. The Mid-Neoproterozoic Browne Formation deposited in the large intracratonic Officer Basin of Western Australia, consists of a thick (up to 200 m) sedimentary succession bearing evaporites precipitated ~830 Ma. The Browne Formation is laterally continuous for hundreds of kilometers in the western part of the Officer Basin. Similar evaporitic facies and thicknesses are documented in the coeval Gillen Member, Bitter Springs Formation, of the adjacent Amadeus Basin that covers part of Western Australia and the Northern Territory. We have used petrography, sedimentology, geochemical analysis, and fluid-inclusion chemistry to characterize the depositional environment, paleogeographic setting, and source of parent waters of the Browne Formation.

2.2 INTRODUCTION

Our work centers on core samples from the exploratory stratigraphic wells, Empress 1A and Lancer 1, of the western part of the Officer Basin, Western Australia (Figure 2.1). Both wells fully core the ~830 Ma Browne Formation, which consists of halite-dominated evaporite successions. This study uses petrographic and geochemical criteria established either from modern and ancient evaporite deposits in order to determine the depositional environments, the origin of parent waters, and to hypothesize about paleoclimate conditions prevailing during

deposition of the Browne Formation, using petrography, sedimentology, geochemical analysis, and fluid-inclusion chemistry.

2.3 GEOLOGIC SETTING

The Officer Basin is the third largest onshore basin in Australia, and covers an area of ~525,000 km^2 in Western and South Australia (Figure 2.1). The stratigraphic succession in the western part of the Officer Basin ranges in age from Neoproterozoic to Cambrian. This sedimentary succession unconformably overlies Mesoproterozoic mafic igneous rocks, and is unconformably overlain by the Paleozoic-Cretaceous strata of the Gunbarrel Basin (Grey et al., 2005). The rocks of the Officer Basin have been divided into three supersequences, whose boundaries are defined by regional unconformities that are associated with major tectonic events in the basin, including the Areyonga Movement and the Petermann and Delamerian Orogenies (Apak and Moors, 2000; Apak et al., 2002). Supersequence 1 consists of the Buldya Group, which has been divided into the lower (Townsend Quartzite and Lefroy Formation), the middle (Browne Formation), and the upper (Hussar, Kanpa, and Steptoe Formations).

This study focuses on the evaporite record of the Browne Formation, cored by the stratigraphic wells Empress 1A and Lancer 1 (Figure 2.1). The Empress 1A stratigraphic core was drilled in 1997 through the Neoproterozoic sequence, reaching basement at a total depth of 1,624.6 m (Stevens and Apak, 1999). The Browne Formation in this well begins at a depth of 1,521.8 m and ends at 1,2471 m. The Lancer 1 well was drilled in 2003 to a total depth of 1,501.3 m, and the Browne Formation was intersected in the interval between 1,479 m and 1,202 m. In both wells, the lower part of the Browne Formation is missing, meanwhile the middle and upper parts consist of up to 275 m of red beds, evaporites, dolomite, and stromatolotic dolomite (Carlsen et al., 1999). In spite of the distance between the two studied wells (~264 km), a remarkably similarity in lithology and thicknesses is observed throughout the sedimentary succession of the Browne Formation encountered. The major difference is a sandstone unit of eolian origin at the top of the Browne Formation in Lancer 1 (the interval between 1,201.9 – 1,297.7 m) that is not present in Empress 1A. This unit, named the Lancer Member, correlates

with the halite-dominated evaporites found in the Empress 1A, Yowalga 3, and Kanpa 1A wells (Figure 2.1). The halite sequences in the Yowalga 3 and Kanpa 1A were not recovered during drilling.

Both the Empress 1A and the Lancer 1 wells are located on the "western platform" of the Officer Basin (Figure 2.1). The western platform is interpreted from seismic data to be a semi-emergent, broad structural shelf, which has been tectonically stable and basically unaffected by salt-tectonic deformation since the deposition of the Browne Formation (Haines et al., 2004; Simeonova and Lasky, 2005). This lateral continuity extends from the Lancer 1 into the Northwestern Officer Basin as documented in the Boondawari 1 well (separated by ~300 km), and south from the Empress 1A to the NJD1 well, covering hundreds of kilometers (Figure 2.1) (Grey et al., 2005). Stratigraphic and lithological continuities along all wells drilled on the western platform, indicate a low topographic gradient across the western platform during deposition of the Browne Formation. The Browne Formation increases in thickness moving northeast from the western platform toward the tectonically active Musgrave Complex (Figure 2.1), as evident from various seismic, sonic, and drill-core data (Apak and Moors, 2000). The predominant source of coarse clastic material entering the basin was from the northeastern margin, and current-direction indicators from the Empress 1A vicinity indicate that water came from the south (Stevens and Apak, 1999).

The Amadeus Basin is a broad, shallow, intracratonic basin, northeast of the Officer Basin, and oriented parallel to that basin. The Amadeus Basin lies at the center of the Australian continent in the Northern Territory and extends into parts of Western Australia (Figure 2.1). The Basin covers an area of ~158,000 km^2.

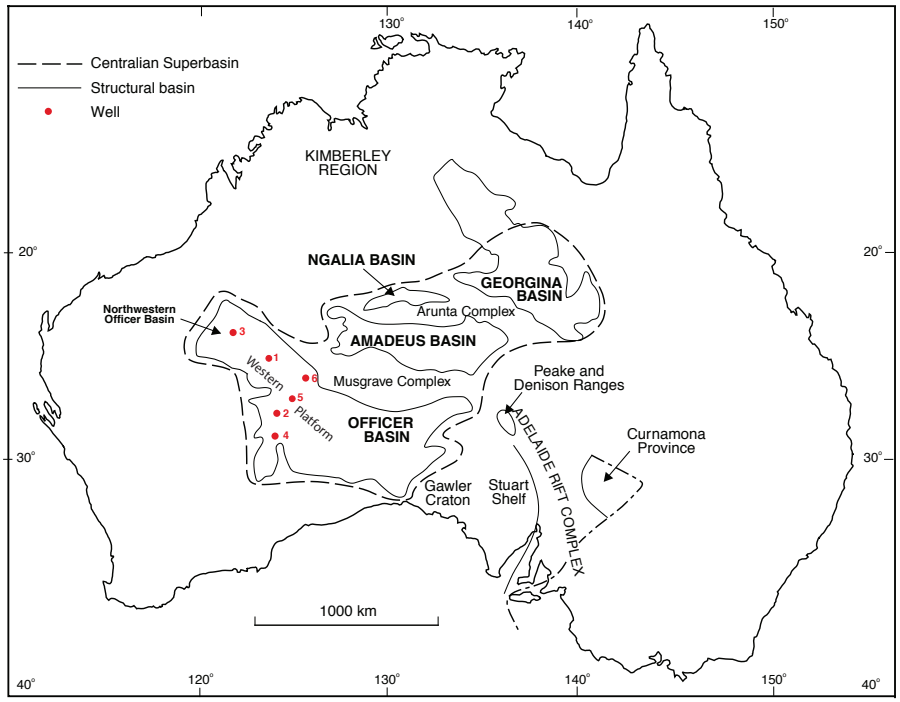

FIGURE 2.1 The Neoproterozoic intracratonic basins and Adelaide Rift Complex of Australia. The Lancer 1 (1) and Empress 1A (2) wells are located in the western part of the Officer Basin, Western Australia. Other wells identified include: (3) Boondawari 1, (4) NJD 1, (5) Kanpa 1, (6) Yowalga 3. Dashed line represents the extent of the Centralian Superbasin. Modified from Hill, 2005.

The Officer and Amadeus Basin were thought to have originated within the Centralian superbasin (Walter et al, 1995). This intracratonic superbasin was one continuous deposition system during Neoproterozoic time for the Officer, Amadeus, Ngalia, and Georgina Basins. While the timing of the structural breakup of the superbasin has not been established (Camacho et al. 2002), the remarkable similarities in the distribution of sediments and depositional styles between the Officer and Amadeus Basins suggest the basins were at least linked during the deposition of the Browne Formation and the Gillen Member of the Bitter Springs Formation. The Gillen Member is a marine sequence that consists of evaporite and clastic rocks (Wells, 1970; Hill et al. 2000). According to subsurface data, salt is likely present under most, if not the entire, Amadeus basin (Lindsay, 1987). Thicknesses of salt vary significantly as a consequence of tectonic activity that caused the less-dense salt to flow between denser rocks, resulting in structures such as large salt-cored anticlines and diapirs (Lindsay, 1987). Estimates of salt thickness, based on current seismic data, range from ~200 m to a maximum of 4,000 m in the Parrara Anticline (Young and Ambrose, 2007). With an areal extent of ~500,000 km^2, the evaporite deposits of the Browne Formation and the Gillen Member are the relicts of a “giant” ancient saline body that persisted across much of Western Australia during Mid-Neoproterozoic time.

The Gillen Member has been correlated with the Browne Formation on the basis of lithology, isotope stratigraphy, and biostratigraphy (Hill et al. 2000; Hill and Walter 2000; Walter and Hill 1999; Grey, 2005). Carbon-isotope analyses and the distribution of the *Acaciella australica* stromatolite assemblage (Grey, 1995; Walter et al., 1995) have enabled stratigraphic correlation among the Amadeus Basin and the Officer Basin, and the Adelaide Rift Complex.

2.4 METHODS

This study focused on the evaporites of the Browne Formation sampled from the Empress 1A and Lancer 1 cores, which were provided by the Geological Society of Western Australia. The sampled intervals correspond to depths between 1,521.8-1,460 m in the Empress 1A and 1,441-1,472 m in the Lancer 1. Mineral identification was performed by optical and electron microscopy (SEM-EDS) and X-ray diffraction (XRD). Thick and thin sections were

prepared using a 0.3mm diamond wire saw, and mounted on glass slides with clear epoxy for analysis by conventional optical and scanning-electron microscopy (ESEM, FEI Quanta-2000) with an energy-dispersive microanalysis (EDS, EDAX-Genesis). All ESEM work was performed at the University of Barcelona, Spain.

The bromine content of several rock-salt samples was determined using X-Ray Fluorescence with a Phillips PW2400 XR-Spectrometer. Samples and standards were measured on pressed powder tablets. Bromine standards were prepared from mixtures of KBr and NaCl ranging in concentration from 1.3 to 690 ppm. Analytical errors were below 5%. Selected halite crystals were powdered in ethanol to eliminate the contribution of the brines retained in fluid inclusions and grain boundaries (Moretto, 1988).

The major-ion chemistry (Na^+, Mg^{2+}, SO_4^{2-}, Cl^-, K^+, and Ca^{2+}) of fluid inclusions in primary halite was determined using the Cryo-SEM-EDS technique (Ayora et al., 1994; Timofeeff et al., 2000; García-Veigas et al., 2009).

2.5 RESULTS AND DISCUSSION

2.5.1 Basics rock types, petrology, and syndepositional features of the Browne Formation

The basic rock types of the Browne Formation include dolomite, anhydrite, fluid-inclusion rich halite, and muddy halite; sandstone occurs as a minor component (Figure 2.2). Both syndepositional and post-burial features can be found in the evaporites of the Browne Formation. Primary syndepositional features are those formed at or after the time of deposition, but before burial, and include: sedimentary structures such as lamination and ripple marks; detrital framework textures, both traction and settle-out; crystalline framework fabric documenting open-space, competitive growth; dissolution and re-precipitation features, such as smooth truncation

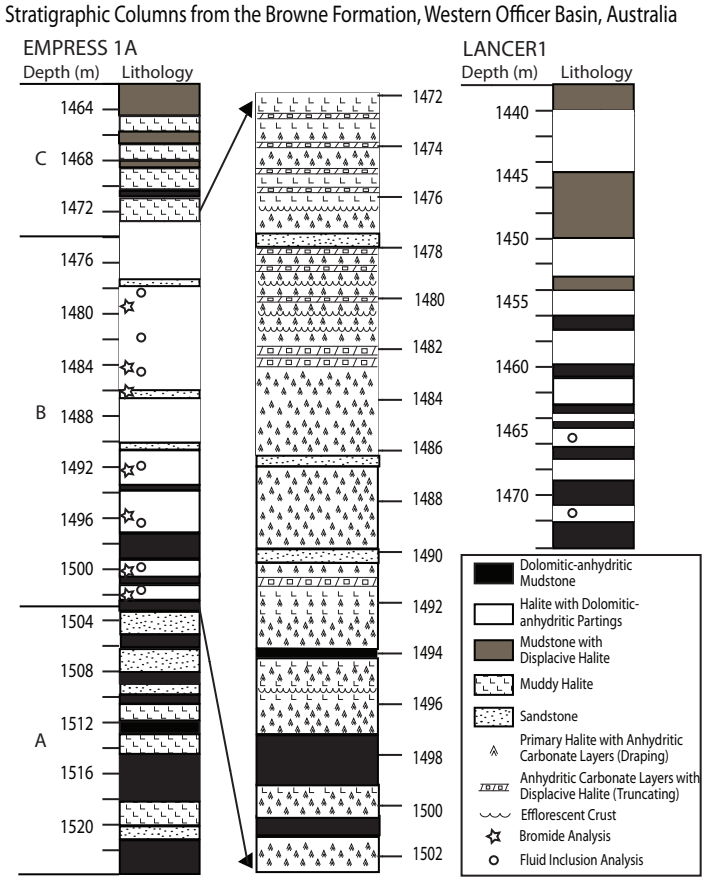

FIGURE 2.2 Measured sections of the Browne Formation from the Empress 1A well (~70 m) and from the Lancer 1 well (~44 m). The basic rock types of the Browne Formation are dolomite, anhydrite, halite, mudstone, and sandstone. Sections are divided on the basis of lithology and depositional environments.

surfaces and rounded crystal terminations; and fluid-inclusion banding (Hardie et al. 1985). Examples of post-burial features include: massive crystalline mosaics that lack bedding; polygonal mosaic textures; and fluid inclusions that have been purged to grain boundaries. It is important to distinguish syndepositional from post-burial features when reconstructing the environment and stratigraphy of an ancient evaporite deposit; as in the case of the Browne Formation, these features provide clues to changes in depositional environment.

The basic rock types of the Browne Formation, based on petrographic observations, are described below in order of their appearance in the core.

a) Dolomite

The dolomite is laminated, fine-grained, and occasionally silty. The color ranges from light greenish-grey to light grey. The texture is micritic, which is typical of dolomite deposited during Neoproterozoic time. Macroscopically visible precipitate structures are rare in carbonates deposited during Neoproterozoic time (Grotzinger and James, 2000). The dolomite is often cemented by halite. In the lower part of the cores (depth 1,525-1,498 m in Empress 1A; depth 1,474-1,456 m in Lancer 1), dolomite commonly occurs finely laminated with anhydrite. Dolomite is rare in the upper part of the sampled core (depth 1,498-1,460 m in Empress 1A; depth 1,454-1438 m in Lancer 1) of the Browne Formation.

b) Anhydrite

Microscopically, anhydrite occurs as aphanitic, blocky, and lath-shaped crystals. Dispersed throughout the anhydrite beds are detrital grains of quartz, K-feldspar, and mica, with minor traces of Fe- and Ti-oxides (hematite and ilmenite) (Figures 2.3A and B). The detrital fraction is not grain-supported, suggesting that the detrital fraction consists of wind-carried grains dropped into a sulfate precipitating brine. There is no evidence of precursor gypsum. Anhydrite also appears as radiating swirls composed of microscopic, lath-shaped crystals (Figure 2.4).

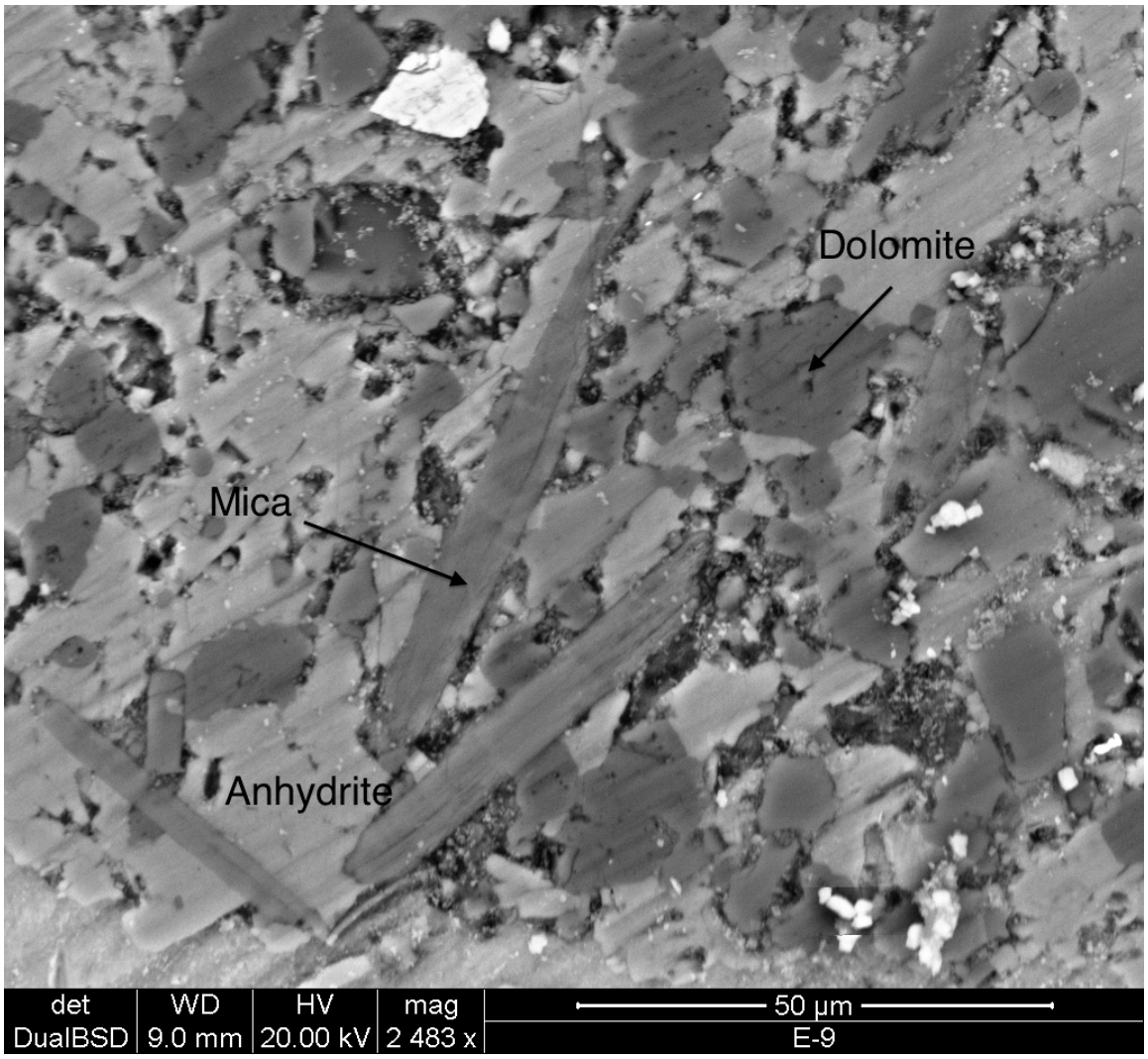

FIGURE 2.3A Photomicrographs of detrital content found in anhydrite beds of the Browne Formation. Detrital fraction consists of quartz, K-feldspar, and mica, with minor traces of Fe- and Ti-oxides (hematite and ilmenite).

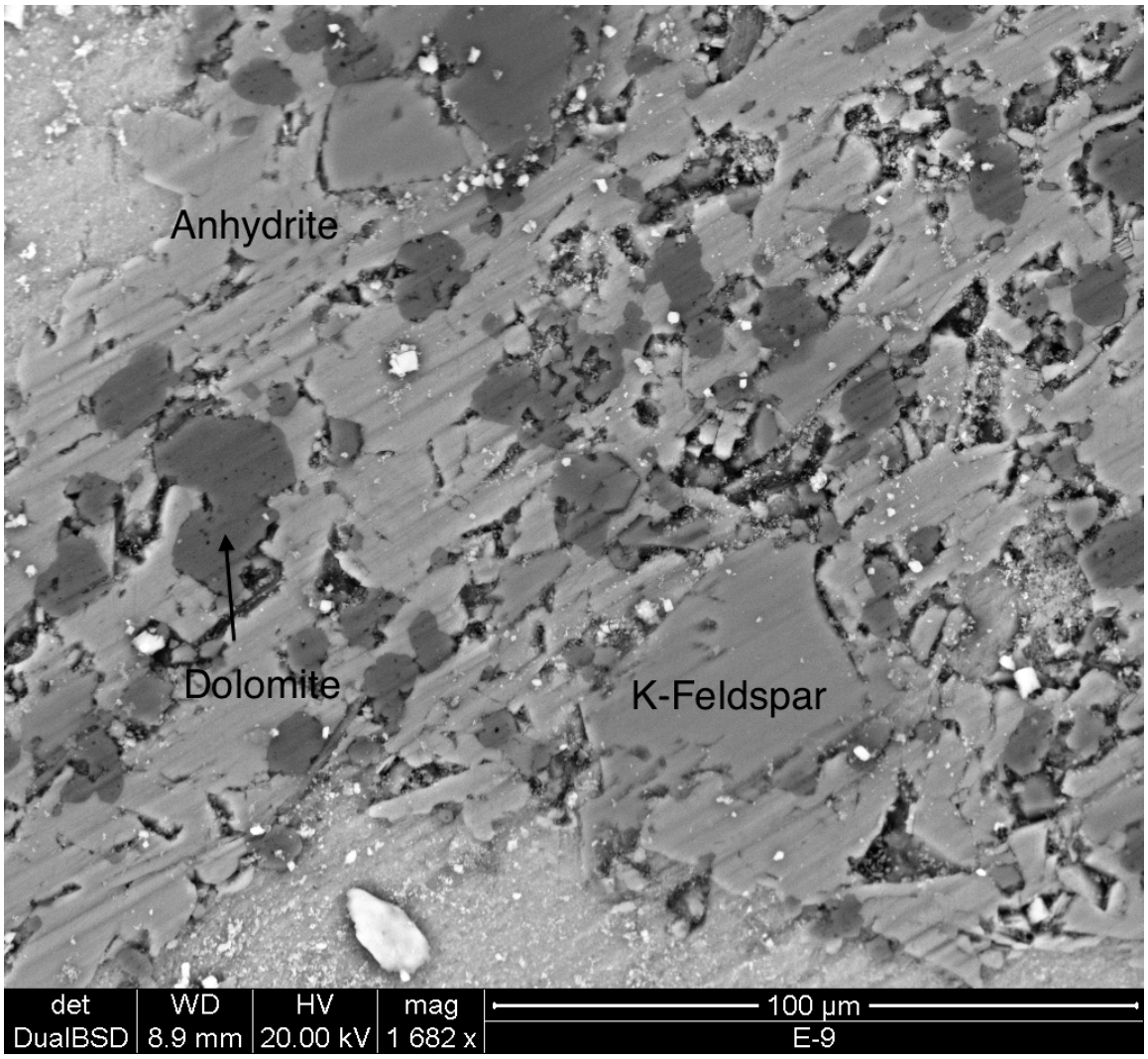

FIGURE 2.3B Photomicrographs of detrital content found in anhydrite beds of the Browne Formation. Detrital fraction consists of quartz, K-feldspar, and mica, with minor traces of Fe- and Ti-oxides (hematite and ilmenite).

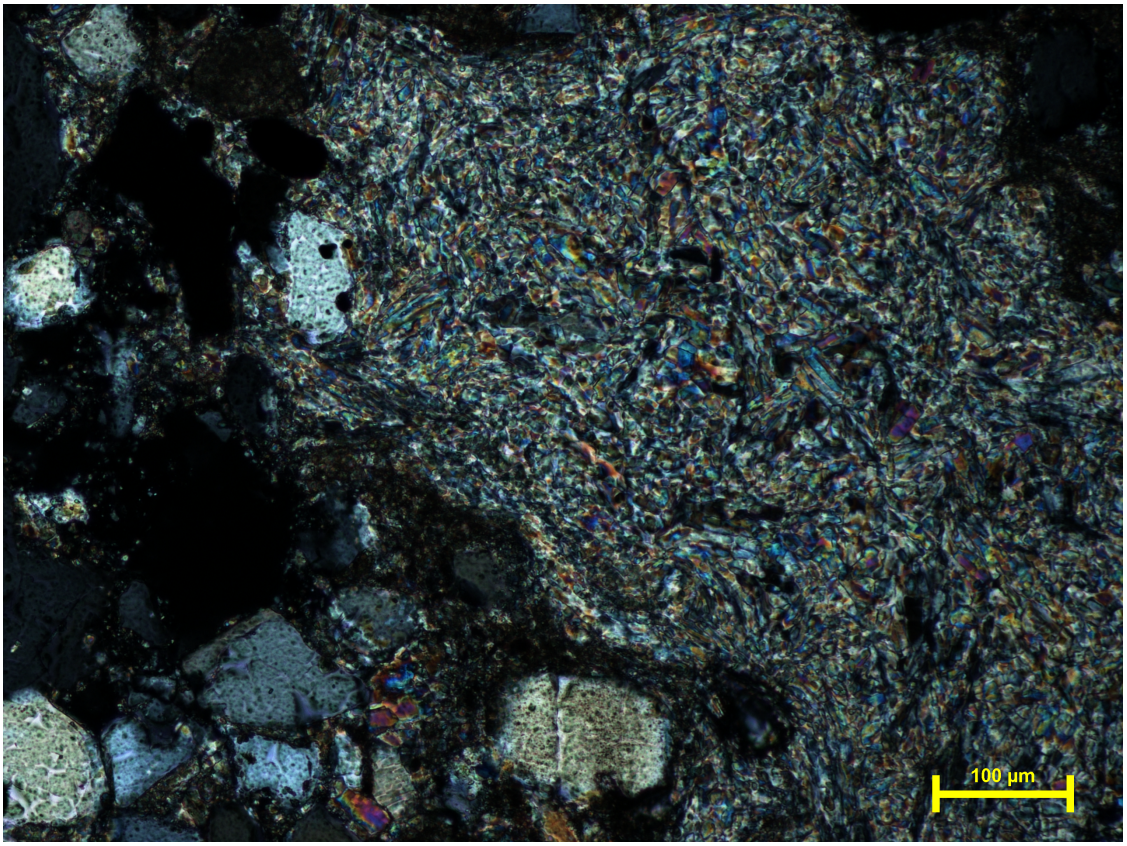

FIGURE 2.4 Photomicrograph of microscopic, lath-shaped anhydrite crystals arranged in a radiating swirl. Sheets of microscopic anhydrite crystals occur in the boundaries between halite crystals and laminated with dolomite.

Anhydrite and dolomite are almost always associated with each other; however, the amount of dolomite is lower in the higher part of the succession.

c) Muddy halite

In the Browne Formation, muddy halite, also called displacive halite, consists of a structureless mix of halite and dolomitic-anhydritic and siliciclastic muds. The mud is either incorporated within the halite, where it approximately follows the crystal growth planes, or incorporated interstitially between halite crystal boundaries (Figure 2.5). Muddy halite grows displacively into unconsolidated sediment beneath the brine table as isolated euhedra crystals or interlocking aggregates of randomly oriented cubes (Lowenstein and Hardie, 1985). In thin section, the halite is clear, fluid-inclusion free and lacks primary features.

d) Fluid-inclusion rich halite

Halite in the Browne Formation occurs interbedded with layers of microcrystalline anhydrite and dolomite that vary on the millimeter-centimeter scale. Isolated crystals of anhydrite and dolomite are present along the grain-boundaries of individual halite crystals as well as trapped crystals (solid inclusions) in halite. The fluid-inclusion rich halite contains syndepositional growth textures and fabrics, such as vertically oriented chevron textures, air-brine-interface nucleated rafts, and bottom-accumulated hopper crystals. These syndepositional features confirm that the fluid-inclusion rich halite is a primary precipitate.

Chevron crystals are composed of alternating dark, fluid-inclusion-rich bands and clear, inclusion-free bands produced by the preferential growth of the crystal edges nucleated on the sediment-water interface (Figure 2.6). These crystals grew upward in a very shallow brine body. The chevron crystals show evidence of syndepositional dissolution and re-precipitation, such as smooth dissolution surfaces that truncate and round the crystals, and are overgrown by clear, inclusion-free halite.

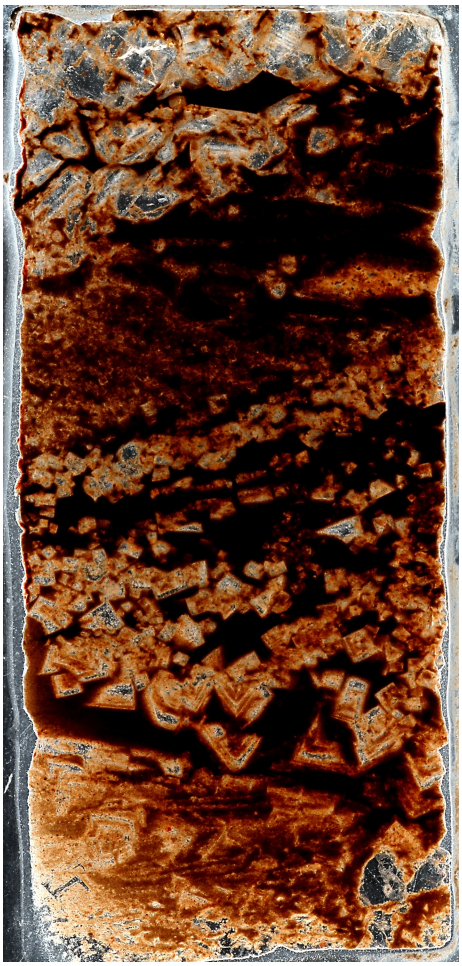

FIGURE 2.5 Thin section of muddy halite showing growth of displacive halite crystals in sediment.

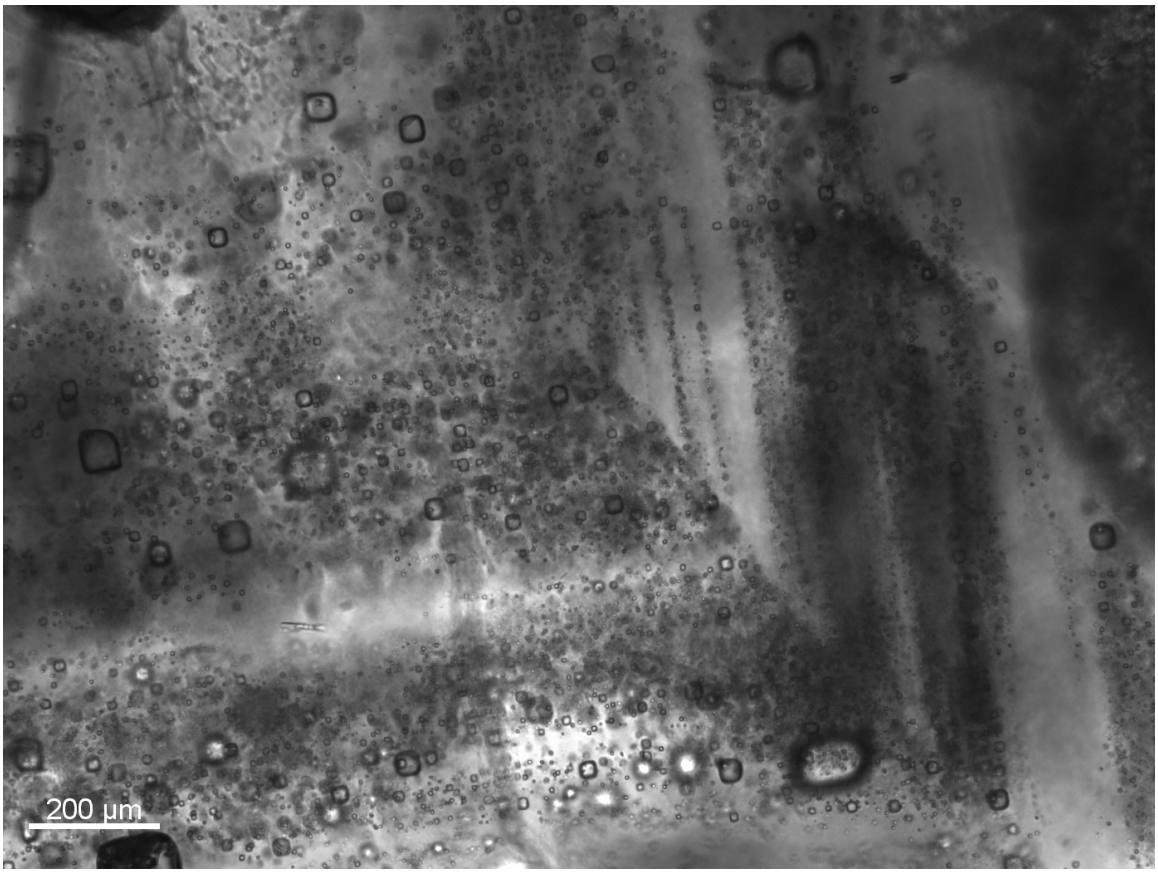

FIGURE 2.6 Photomicrograph of a primary chevron crystal from halite in Section B. Chevrons are distinguished by alternating dark, inclusion-rich and clear, inclusion-poor bands that represent relict growth surfaces. Chevrons are ideal for fluid-inclusion analysis because of the high concentration of primary fluid inclusions.

Cumulate crystals consist of millimeter-scale cubic halite crystals that formed rafts at the air-brine interface. Once the density of the cumulate crystals exceeded that of the brine, they sank and formed layers of loosely packed crystals. The sunken cumulates provided nucleation surfaces for the upward growth of inclusion-rich chevron crystals. Bottom-growth crystalline frameworks are characterized by vertically oriented, vertically elongated, upward-widening crystals (Lowenstein and Hardie 1985). The resultant crystals are typically large (several mm to cm) and contain abundant fluid inclusions. While chevron textures are common in the Browne Formation halite, cumulates are much more difficult to distinguish.

The core also contains intervals of halite resembling efflorescent halite crusts formed by the evaporation of subsurface brines in subaerial, exposed conditions that are commonly present in salt pan environments (Lowenstein and Hardie, 1985). Efflorescent crusts lack any sedimentary textures, fabrics, or bedding, which indicates the halite did not grow from suspension or from the bottom of a halite saturated brine. Post-burial features, such as polygonal mosaic textures and clear massive halite lacking fluid-inclusion banding, were also observed in thin section.

2.5.2 The depositional environments of the Browne Formation evaporites

To accumulate a succession of evaporites of significant thickness, a sedimentary basin must maintain roughly steady-state conditions, meaning a constant volume and solute concentration, for some time (Sanford and Wood, 1991). Water that is lost to evaporation is refreshed by inflow waters, which are mixed with the brine and subsequently concentrated by evaporation. Therefore, changes in lithology indicate different degrees of restriction of circulation within the basin.

The evaporitic succession that accumulated on the shallow western platform of the Officer Basin displays three dominant environmental regimes (sections A, B, and C; Figure 2.2) that influenced the depositional systems of the Browne Formation. Each of these regimes is differentiated by changes in mineralogy and sedimentary textures and structures, and ultimately

represent varying degrees of basin restriction. These regime changes are also due to variations in the prevailing source of inflow waters, changing the chemical composition of the basin brine. This change could be the result of an influx of undersaturated water (marine, meteoric or mixed marine-meteoric) or from syndepositional recycling. Syndepositional recycling occurs when dilute inflow waters dissolve previously deposited halite, thus altering the brine composition.

a) Section A

Section A (depth 1,525-1,503 m: Empress 1A) consists mostly of dolomite, with minor amounts of anhydrite, sandstone, and muddy halite. Anhydrite occurs associated with dolomite in finely laminated layers or as lenses consisting of masses of acicular crystals arranged in swirls (Figures 2.3 and 2.7-2.9). In the Gillen Member, Hill et al. (2000) reported that gypsum was the primary sulfate, and was subsequently dehydrated to anhydrite after burial. The anhydrite layers of the Browne Formation most likely replaced gypsum as well; however, pseudomorphs after primary gypsum have not been recognized. In the Browne Formation, sandstone occurs in thin, finely laminated intervals and is typically cemented with halite and minor amounts of anhydrite. The detrital component consists of quartz, K-feldspar, and muscovite.

The dolomite and dolomitic-anhydritic mudstone layers represent deposition in subaqueous conditions. Since the dolomite is so closely associated with anhydrite, the brine body at this time was not concentrated beyond gypsum saturation. The dolomitic mud with displacive halite crystals suggests periodic dry conditions. Section A represents a marginal marine, shallow lagoon environment.

b) Section B

Section B (depth 1,503-1,473 m; Empress 1A) consists predominantly of halite, containing acicular anhydrite crystals trapped as solid inclusions along grain boundaries. There are several thin beds of finely laminated sandstone cemented by halite and anhydrite that appear

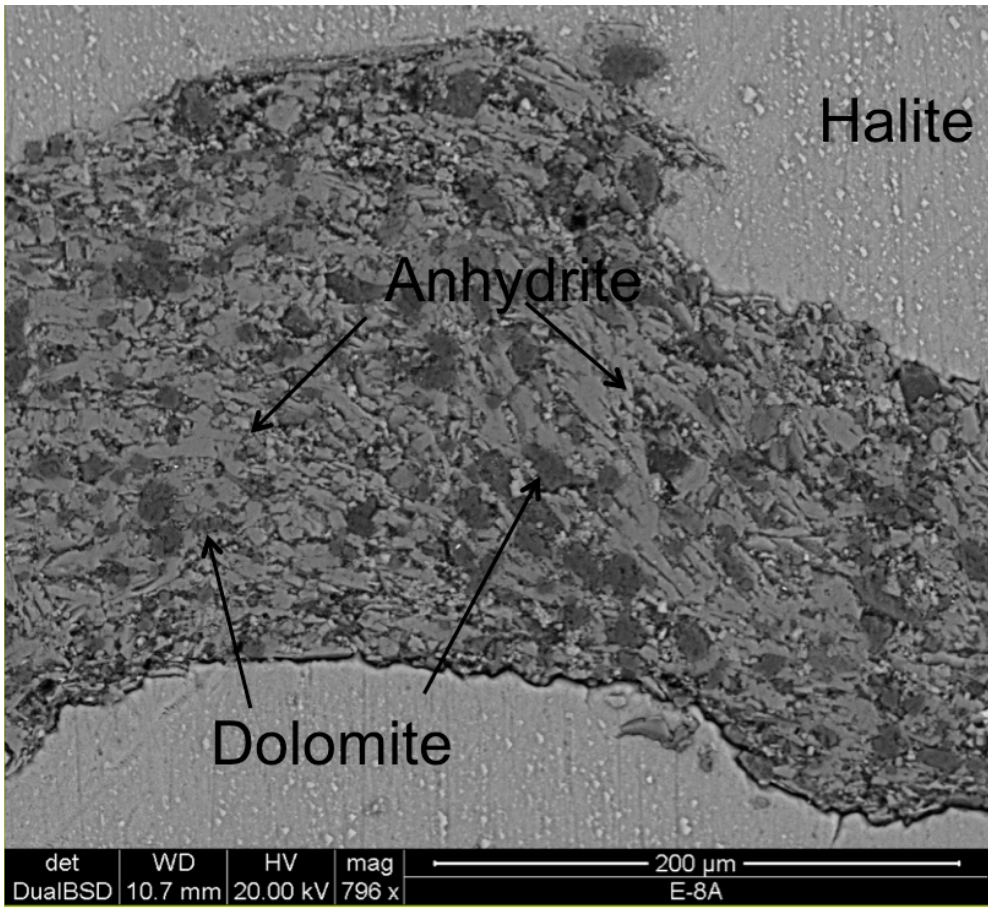

FIGURE 2.7 Photomicrograph of the mm-cm scale anhydritic-dolomitic mud layers that appear as either truncating or draping surfaces at cm-scale intervals throughout the halite layers.

FIGURE 2.8 Thin section photo illustrating a draping mud layer indicative of settle-out from a perennial water body.

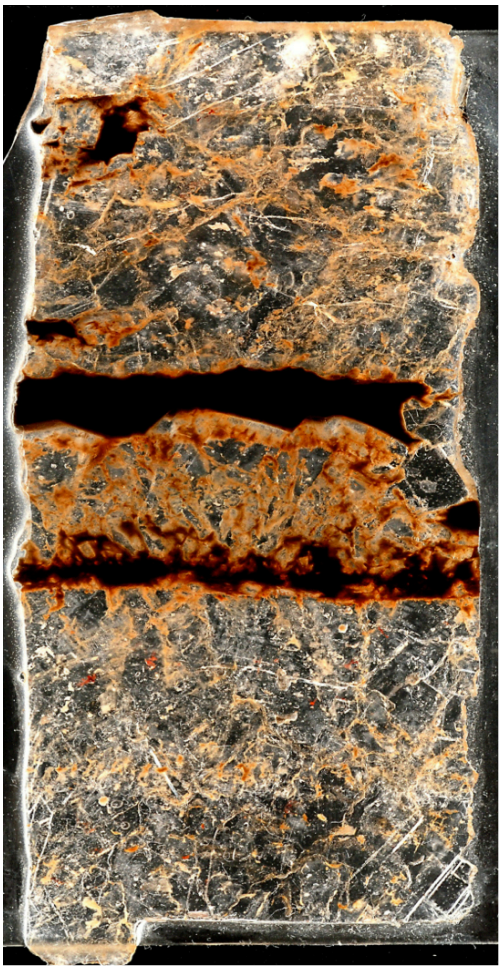

FIGURE 2.9 Thin section photo illustrating a truncating anhydritic-dolomitic mud layer representing an influx of diluted water.

within the bedded halite layers. Strata of anhydrite and dolomite, which range in thickness from less than a millimeter to several millimeters, appear irregularly throughout the bedded halite layers (Figure 2.7). Some of these layers drape over the halite crystals and indicate that those strata have settled out of a perennial brine body (Figure 2.8). Some of these layers truncate the top of the halite crystals and represent dissolution surfaces caused by flooding that inundated the basin with undersaturated water (Figure 2.9). These dissolution surfaces are indicative of a shallow, non-stratified brine body. If the brine were stratified, the lower density of the undersaturated water would keep it at the top of the brine column, without coming into contact with the halite located on the basin floor.

The halite in the lower part of Section B (depth 1,503-1,483 m; Empress 1A) contains well-preserved primary chevron crystals. The halite in the upper part of Section B (depth 1,483-1,472 m; Empress 1A) contains primary halite as well, but with a greater abundance of post-burial features, such as efflorescent crusts and clear, recrystallized halite. Intervals of muddy halite appear throughout Section B.

Section B represents a marginal marine environment in which the thicker layers of halite and dolomitic-anhydritic mud are the result of subaqueous deposition in a saline lagoon. This setting evolves toward ephemeral conditions in which the muddy halite and efflorescent crusts were formed. Basin restriction and environmental conditions oscillated from a shallow lagoon to an ephemeral, marine salt pan.

c) Section C

Section C (depth 1,473-1,460 m; Empress 1A) of the Browne Formation consists of large, clear halite crystals mixed with siliciclastic mudstone and massive, recrystallized halite, all lacking primary features. The detrital component consists of quartz, K-feldspar, and muscovite. The detrital content is higher in sections A and C than in section B.

Although muddy halite occurs in both sections A and C, the major difference in the two environments is the absence of evidence for subaqueous conditions in section C. The muddy

halite found in Section C is texturally similar to halite found growing diagenetically in the subsurface of brine-soaked muds of modern salt pans and fringing saline mudflats (Lowenstein and Hardie, 1985). In section A, anhydrite was typically associated with dolomite, whereas in section C dolomite is scarce and anhydrite is typically associated with silicates. The absence of subaqueous deposits and the increase in siliciclastic material indicates a general transition from salt pan to mudflat.

2.5.3 Bromine Concentrations in Halite

The bromine (Br) values (avg. 102 ± 14 ppm) (Table 2.1) are in the range of those expected for halite precipitated from seawater (Valyashko, 1956; Holser, 1966; Braitsch, 1971; Siemann, 2003). The first halite to precipitate from modern evaporated seawater contains 68-75 ppm and reaches 200 ppm near the onset of K-bearing chloride mineral precipitation (Valyashko, 1956; Holser, 1966).

The Empress 1A section shows a clear decreasing upward trend in bromine concentration, from 122 to 73 ppm. Bromine content in samples from the Lancer 1 well are within a very narrow range (from 111 to 107 ppm) and could be correlated with the lower part (depth 1,503-1,494 m) of the Empress 1A section. The Br profile is consistent with our petrographic observations that show a transition from a hypersaline marine lagoon to a salt-pan environment. The decrease in Br content could be the result of an influx of dilute water (fresh seawater or meteoric water) or syndepositional recycling of halite. The halite precipitated from these altered brines will have lower Br concentrations. The Browne Formation shows evidence of both syndepositional recycling and influx of diluted water, especially in Section C, and a combination of the two processes are likely the cause of the decreasing Br profile.

TABLE 2.1 BROMINE VALUES FOR ROCK SALT

Sample Depth (m)	Br (ppm)
Empress 1A	
1479	73
1484.5	91
1486	87
1492	93
1496	103
1500	106
1501	119
1502	122
Lancer 1	
1465.5	107
1471.5	111

2.5.4 Fluid-inclusion composition

Fluid inclusions trapped in chevron bands of primary halite crystals were analyzed to determine the major-ion chemistry of Mid-Neoproterozoic seawater (Spear et al., in preparation). Results fall in the range of seawater concentrations documented by other fluid-inclusion studies (Lowenstein et al., 2001, 2003, 2005; Horita et al., 2002; Brennan et al., 2004; Timofeeff et al., 2006). The evaporation path of the Mid-Neoproterozoic seawater closely resembles that of modern seawater. The fluid-inclusion composition confirms petrographic and geochemical evidence indicating that the Browne Formation was deposited in a marine setting.

2.5.5 Summary of Depositional Environment of the Browne Formation

The dolomite and dolomitic-anhydritic muds of section A were deposited in a shallow lagoon fed by seawater. Intervals of muddy halite indicate occasional desiccation conditions in which halite crystals grew displacively in the muds from halite-saturated ground water. The halite of section B contains syndepositional textures indicative of deposition in environments ranging from shallow lagoon to a subaerially exposed salt pan. These conditions must have persisted for a prolonged period of time in order to produce such a thick halite deposit. The muddy halite and siliciclastic mudstones of Section C represent episodes of complete basin restriction and evolution from a salt pan to a saline mudflat with a larger influx of dilute inflow waters. Overall, the Browne Formation in Empress 1A and Lancer 1 was characterized by basin shallowing and increase in brine concentration that led to basin desiccation. These general upward-shallowing sequences repeat several times in the Browne Formation (Apak and Moors, 2000).

2.5.6 Evidence for widespread halite precipitation from an ancient “saline” giant

The salt of the Browne Formation thickens and is found at deeper depths moving northeast from the Empress 1A well towards the Kanpa 1A and Yowalga 3 wells and the Musgrave Complex (Figure 2.1). In the southern part of the Officer Basin, the Browne Formation consists of dolomite and shale and current-direction indicators from the Empress-1A vicinity point to a southern source for marine inflow (Stevens and Apak, 1999). This suggests deeper water

and the open ocean was to the south and the Empress 1A and Lancer 1 wells lay on the perimeter of a vast shallow sea. This agrees with our petrographic observations that the Browne Formation in Empress 1A and Lancer 1 was deposited in a marginal marine setting.

The similarity in the characteristics and thicknesses of the facies of the Browne Formation indicate that the rate of accommodation kept pace with sedimentation rates (Apak and Moors, 2000). This implies that the Browne Formation was deposited over a large, shallow, tectonically stable area. The repetition of deposition cycles seen in the Empress 1A core indicates these conditions persisted for a long period of time. Our interpretation of the depositional environment of the Browne Formation correlates with interpretations of the coeval the Gillen Member, Bitter Springs Formation of the Amadeus Basin (Lindsay, 1987; Hill et al., 2000; Walter et al., 2000). The widespread deposition of halite (~500,000 km^2) and the similarities in thicknesses, facies, and depositional environments strongly suggest that the Browne Formation of the Officer Basin and the Gillen Member of the Amadeus Basin were deposited from a “giant” hypersaline body of water, on a scale that is not found at present.

2.6 CONCLUSION

Mineralogic, petrographic, and isotopic data from the Browne Formation clearly points to a marine origin. Br measurements fall within the range characteristic of halite precipitated from seawater. The stratigraphy is consistent with a marginal marine environment (bedded carbonate/sulfates, halite, muddy halite) with changes in lithology representing changes in basin restriction. There is a clear evolution from marine lagoon to hypersaline lagoon to salt pan to saline mudflat represented in the stratigraphy, petrography and geochemical data of the Browne Formation.

Based on biostratigraphic and isotopic correlations, similarities in lithology and depositional environment, and the geographic extent and magnitude of halite deposition, the Browne Formation of the Officer Basin and the Gillen Member of the Bitter Springs Formation, Amadeus Basin, are relicts of an ancient saline giant that covered hundereds of thousands of

kilometers of Neoproterozoic Australia. The mass of halite deposited, and the preservation of syndepositional features within halite crystals, indicate the climate was arid and must have remained so for a long period of time.

CHAPTER 3: EVIDENCE FROM FLUID INCLUSIONS EXTENDS THE RECORD OF SEAWATER CHEMISTRY BY ~300 MILLION YEARS FROM ~544 MA TO ~830 MA

3.1 ABSTRACT

We analyzed primary fluid inclusions in halite from marine evaporites in the ~830 Ma Browne Formation of the Officer Basin in Western and Southern Australia by the Cryo-SEM-EDS technique. The parent seawater in the inclusions contained ~565 mM Cl^-, ~456 mM Na^+, ~50 mM Mg^{2+}, ~9-12 mM Ca^{2+}, ≥ 3 mM SO_4^{2-}, and ~1 mM K^+. The concentrations of the major ions, except K^+, are within the range of Phanerozoic seawater in which the concentration of Ca^{2+} exceeds that of SO_4^{2-} such as it did in Cambrian, Silurian, Devonian, Jurassic, and Cretaceous seawater. This is the first direct measurement of the composition of Mid-Neoproterozoic seawater and extends present-day knowledge of seawater chemistry by ~300 Ma. Our results allow us to place a tighter constraint on the concentration of Mid-Neoproterozoic seawater sulfate than was previously possible.

3.2 INTRODUCTION

The major-ion composition (Na^+, K^+, Ca^{2+}, Mg^{2+}, Cl^-, SO_4^{2-}, and HCO_3^-) of seawater has varied considerably during Phanerozoic time. These variations have been documented by changes in: a) the primary mineralogy of oolites (Sandberg, 1983); b) the mineralogy of dominant reef-building taxa (Stanley and Hardie, 1998); c) the mineralogy of marine evaporites (Hardie, 1996), d) the Mg/Ca ratio of benthic foraminiferal calcite and echinoderms (Lear et al., 2000; Dickson, 2002); and e) the composition of fluid inclusions trapped in halite (Lowenstein et al., 2001, 2003, 2005; Horita et al., 2002; Brennan et al., 2004; Timofeeff et al., 2006). In many ways the fluid inclusion evidence is the most definitive. The current record of seawater chemistry derived from fluid inclusions begins at the Precambrian-Cambrian boundary (544 Ma) with data from the Ara Formation, Oman (Brennan et al., 2004). Here we present measurements of the major-ion chemistry of Mid-Neoproterozoic seawater based on the composition of primary fluid inclusions trapped ~830 million years ago (Ma) during deposition of the Browne Formation halite,

Officer Basin, Western Australia. Our results extend the record of seawater chemistry by ~300 million years.

The amount of sulfate in the early ocean was closely linked to the amount of oxygen in the atmosphere and deep ocean. The concentration of seawater sulfate in the Mid-Neoproterozoic was much lower than the concentrations of sulfate in the Late Proterozoic, Permian, and Cenozoic oceans (Kah et al., 2004). By imposing a tighter constraint on the sulfate levels of Proterozoic seawater, we can better define the circumstances and timing of the oxygenation of the Earth's atmosphere and oceans.

3.3 GEOLOGY

The Officer Basin covers an area of ~525,000 km^2 in Western and South Australia and is the third largest preserved onshore basin in Australia (Figure 3.1). The rock section in the Officer Basin consists of three supersequences whose boundaries are defined by regional unconformities associated with major tectonic events that include the Areyonga Movement and the Petermann and Delamerian Orogenies (Apak and Moors, 2000). Supersequence 1 consists of the Buldya Group, which has been divided into the lower (Townsend Quartzite and Lefroy Formation), the middle (Browne Formation), and the upper (Hussar, Kanpa, and Steptoe Formations).

We sampled the Browne Formation from two cores: Empress 1A and Lancer 1, both of which were drilled on the Western Platform of the Basin (Figure 3.1). The Western Platform is interpreted to have been a semi-emergent, broad, structural shelf that has been tectonically stable since Neoproterozoic time. The halite of the Browne Formation in this portion of the Officer Basin has not been mobilized or deformed. The lack of deformation has helped to preserve syndepositional primary textures that are ideal for fluid-inclusion analysis.

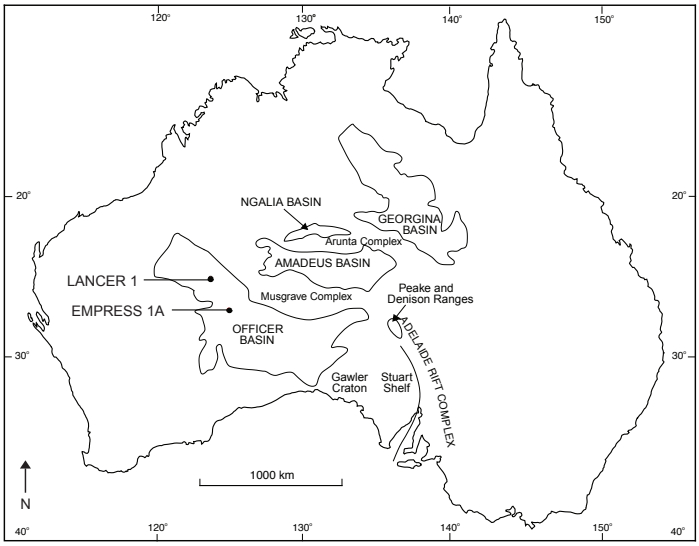

FIGURE 3.1 Locations of the Empress 1A and Lancer 1 drill cores on the tectonically stable Western Platform, Officer Basin, Western Australia. The wells are ~264 km apart. Modified from Hill et al., 2000.

The Browne Formation is well dated at ~830 Ma on the basis of correlation with other Neoproterozoic successions in Canada, Spitsbergen, Namibia, and with the Gillen Member of the Bitter Springs Formation in the adjacent Amadeus Basin, Australia using lithology, isotope stratigraphy, biostratigraphy, and radiometric dating (Hill et al., 2000b; Hill and Walter, 2000; Preiss, 2000). Collectively, the halite deposits of the Browne Formation and Gillen Member underlie an area ~500,000 km^2, and were deposited when an extensive epeiric sea covered parts of Western and Northern Australia. Isotopic and geochemical evidence points unequivocally to a marine origin for the Browne Formation and the equivalent Gillen Member (Claypool et al., 1980; Hill et al., 2000a). The evaporites of the Browne Formation follow the predicted sequence for salts precipitated from seawater: marine carbonates (dolomite) followed by calcium sulfate rocks (gypsum/anhydrite) followed by halite, without reaching the later stages of evaporation in which potash salts (Mg-sulfates and K-Mg-chlorides) precipitate.

3.4 STRATIGRAPHY & PETROGRAPHY

The major rock types of the Browne Formation are dolomite, anhydrite, and halite; sandstone is a minor component. The formation can be divided into three sections (A, B, and C), each deposited in a distinct paleoenvironment (Figure 3.2). In Empress 1A, section A (depth of 1,525-1,503 m) consists of layered dolomicrite, anhydrite, sandstone, and muddy halite. Section B (depth of 1,503-1,473 m) consists mainly of halite, interbedded with dolomicrite and anhydrite, and thin beds of sandstone. The halite contains syndepositional growth textures and fabrics, such as vertically oriented chevron textures, air-brine-interface nucleated rafts, and bottom-accumulated hopper crystals, all primary features similar to those observed in modern halite precipitated in shallow, non-stratified bodies of water (Lowenstein and Hardie, 1985). Section C (depth of 1,473-14,60 m) of the Browne Formation consists of a chaotic mixture of large, clear halite crystals interbedded with mudstone and massive, recrystallized, efflorescent halite, all lacking primary features.

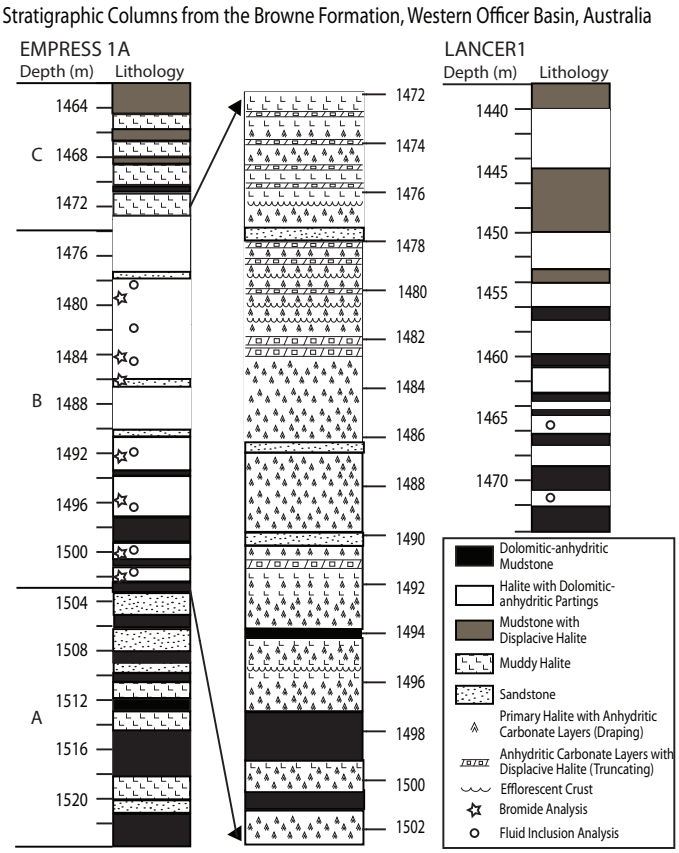

FIGURE 3.2 Measured sections of the Browne Formation from the Empress 1A well (~70 m) and from the Lancer 1 well (~44 m). The basic rock types of the Browne Formation are dolomite, anhydrite, halite, mudstone, and sandstone. Sections are divided on the basis of lithology and depositional environments. Halite from depths of 1,503-1,483 m contains primary structures such as chevron and cumulate crystals ideal for fluid-inclusion analysis.

The dolomite and anhydrite strata of section A were deposited in a shallow body of water not concentrated beyond gypsum-anhydrite saturation. These chemical sediments were deposited in subaqueous conditions, influenced by the inflow of seawater and evaporative concentration. The halite of section B formed during a hypersaline stage of a brine body. In contrast, the halites of section A and C formed interstitially within brine-saturated muds during desiccation episodes. The Browne Formation displays a general trend from a shallow marine body in which carbonate and sulfate rocks precipitated to a restricted hypersaline body precipitating halite and finally to a desiccated mudflat wherein halite formed interstitially.

3.5 ANALYTICAL TECHNIQUES

The major-ion chemistry of fluid inclusions in halite was analyzed using the Cryo-SEM-EDS technique (García-Veigas et al., 2009). Inclusions larger than 15 microns were analyzed for Na^+, Mg^{2+}, S (SO_4^{2-}), Cl^-, K^+, and Ca^{2+} using a SEM JEOL-840 with an EDS Si(Li) equipped with an INCA X-ray processor (Oxford Instruments Ltd.). Precision error is lower than 10%. Analyses were performed at the Scientific and Technological Centers at the University of Barcelona, Spain. The EQL/EVP computer program, based on the Pitzer ion-interaction model, was used to model the potential evaporation paths of the evolving parent brine (Risacher and Clement, 2001).

3.6 RESULTS

In Figures 3.3 (A, B, C, and D) we plot the major-ion compositions (Ca^{2+}, Mg^{2+}, K^+, and Na^+ v. Cl^-) of individual Browne Formation fluid inclusions, as determined by Cryo-SEM-EDS analysis (Table 3.1), against the evaporation paths calculated by the computer program EQL/EVP. EQL/EVP is a brine-evaporation equilibrium model that calculates the ion concentrations of evaporating water and the amounts of salts precipitated at each evaporation step (Risacher and Clement, 2001). Dashed lines NP1, NP2, and NP3 in Figure 3.3 represent the evaporation paths calculated by the program EQL/EVP that best fit the fluid-inclusion data from the Browne Formation. We list the calculated initial concentrations used in the modeling in Table 3.2, and we describe the steps taken to determine these initial concentrations below. The solid

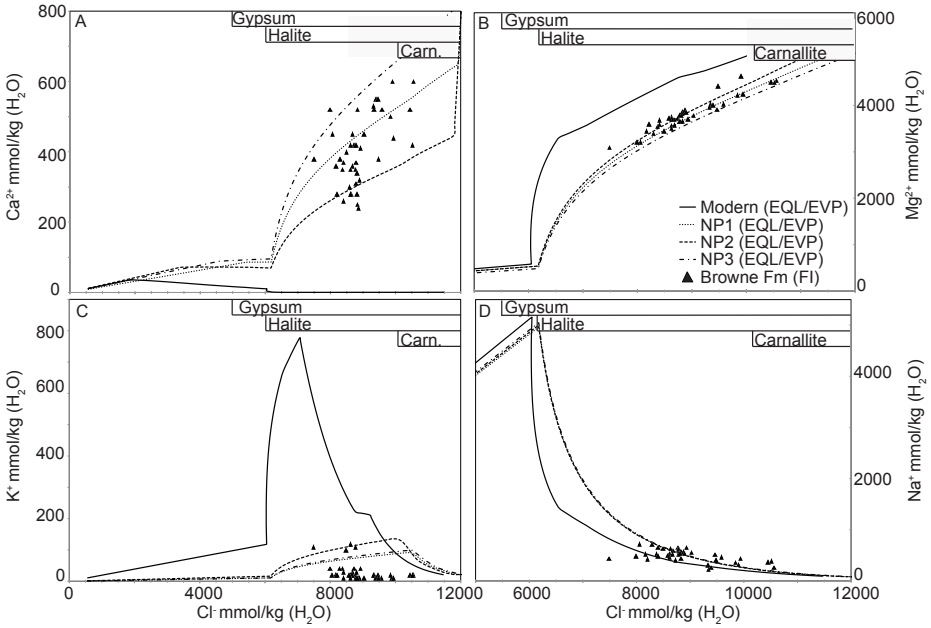

FIGURE 3.3 (A, B, C and D) Concentrations of (A) Ca^{2+}, (B) Mg^{2+}, (C) K^{+}, and (D) Na^{+} v. Cl^{-} in the Browne Formation fluid inclusions. The solid black line shows the chemical evolution during the evaporation of modern seawater. NP1, NP2, and NP3 represent the evaporation paths predicted by EQL/EVP that best fit the fluid inclusion data. Minerals predicted to precipitate during the evaporation of the Browne Formation brine are listed in the upper bars.

TABLE 3.1 THE MAJOR-ION COMPOSITION OF BROWNE FM FLUID INCLUSIONS AS DETERMINED BY CRYO-ESEM-EDS.

Depth (m)	Na^+	K^+	Ca^{2+}	Mg^{2+}	Cl^-
1478 (E)	530	40	350	3550	8370
1478 (E)	410	40	420	3720	8730
1478 (E)	650	30	370	3590	8400
1478 (E)	720	20	450	3210	8060
1478 (E)	660	20	350	3680	8770
*1482 (E)	320	10	600	4640	9900
*1482 (E)	370	20	520	4510	10450
1482 (E)	220	20	520	4030	9340
*1482 (E)	260	20	600	4540	10560
1482 (E)	310	20	530	3970	9330
1482 (E)	260	10	550	4010	9390
1492 (E)	630	110	370	3650	8780
1492 (E)	630	100	400	3450	8490
1492 (E)	520	120	420	3570	8620
1492 (E)	440	110	380	3090	7490
1497 (E)	620	20	420	3650	8780
1497(E)	590	30	450	3580	8680
1497 (E)	710	40	380	3390	8290
1497 (E)	490	40	520	3210	7990
1497 (E)	650	40	410	3710	8930
1497 (E)	530	20	360	3450	8170
1501.8 (E)	630	20	280	3500	8630

1501.8 (E)	540	20	280	3750	8620
1501.8 (E)	570	10	280	3840	8820
1501.8 (E)	580	10	250	3870	8830
1501.8 (E)	490	10	260	3690	8400
1501.8 (E)	580	10	240	3900	8870
1502.2 (E)	530	20	360	3700	8670
1502.2 (E)	430	20	280	3600	8210
1502.2 (E)	530	10	310	3810	8780
1502.2 (E)	470	10	350	3720	8620
1502.2 (E)	500	20	300	3730	8580
1502.2 (E)	540	30	340	3780	8810
1502.2 (E)	540	10	320	3850	8890
1466.25 (L)	520	20	550	3910	9460
1466.25 (L)	440	10	520	3670	8830
1466.25 (L)	560	10	450	3780	9030
1466.25 (L)	470	10	520	4030	9580
*1466.25 (L)	360	20	500	4230	9840
1443.6(L)	440	10	440	4250	9940
1443.6(L)	410	10	380	4420	9480
1443.6(L)	390	20	420	4490	10520

Note: Concentrations in mmol/kg H_2O. Samples from Empress 1A designated by (E) and from Lancer 1 by (L).

*Depths correspond to fluid-inclusions that fall in the potash zone.

TABLE 3.2 THE INITIAL COMPOSITION OF THE MODEL SEAWATERS NP1, NP2, AND NP3

Ion	NP1	NP2	NP3
Na^+	452	457	460
K^+	1	1.5	1
Mg^{2+}	50	50	45
Cl^-	565	566	565
Ca^{2+}	9	12	11
SO_4^{2-}	3	8	4

Note: Concentrations in mmol/kg H_2O. Calculated using the computer program EVP/EQL (Risacher and Clement 2001).

lines labeled *Modern* show the evaporation paths and salts precipitated from modern seawater. Minerals predicted by EQL/EVP to precipitate during the evaporation of the Browne Formation brine are listed in the upper bars in Figure 3.3.

The initial composition of the Browne Formation seawater can be defined, at least roughly, on the basis of the diagrams in Figure 3.3 and the requirement of electrical neutrality. We must make several assumptions concerning the paleosalinity and chlorinity of Neoproterozoic seawater, as there are currently no data on either. The freezing-point depression of aqueous fluid inclusions in marine calcites by microthermometric analysis can be used to determine the paleosalinity of ancient seawater (Goldstein and Reynolds, 1994). Microthermometric measurements from primary fluid inclusions in Cambrian (Johnson and Goldstein, 1993) and Upper Devonian marine calcites (Kwong, 1995; Ward, 1996) indicate a salinity of 31-47‰. This is in the range of present-day seawater in shallow, open to slightly restricted, marine environments, similar to the depositional environment we have reconstructed for the Browne Formation. Assuming that the salinity and chlorinity of Mid-Neoproterozoic seawater was similar to modern seawater. Given this prerequisite, we set an initial Cl^- concentration of 565 mmol/kg H_2O (mM). The concentration of bicarbonate (HCO_3^-) in modern seawater (2.5 mM) is low compared to the other major ions, and it is likely that this was also true during the Mid-Neoproterozoic, so HCO_3^- is ignored in the EQL/EVP modeling and in our calculations.

Based on the principle of chemical divides, there is either excess Ca^{2+} or excess SO_4^{2-} after the precipitation of gypsum/anhydrite. After $CaCO_3$ and $CaSO_4$ precipitate, the effective Ca^{2+} concentration (mCa^*) is defined as:

$$mCa^* = mCa^{2+} - (mSO_4^{2-} + \tfrac{1}{2}mHCO_3^-). \qquad (1)$$

According to fluid-inclusion compositions in the Browne Formation, halite-saturated brines correspond to a Ca^{2+}-rich type with sulfate concentrations lower than detection limit (< 30 mM; García-Veigas et al., 2009). Consequently, Ca^{2+} concentration in parent seawater, before $CaCO_3$

and $CaSO_4$ precipitation, was greater than the sum of initial sulfate and bicarbonate. Figure 3.3B indicates that Mg^{2+} concentrations in halite-saturated brines of the Browne Formation were lower than those of present-day saturated marine brines. An initial Mg^{2+} concentration of 50 mM, slightly lower than the modern value (55 mM) fits well with the calculated trends. The Mg/Ca^* ratio determined from Browne Formation fluid inclusions falls in the range of 7 to 13, with an average value of 10. Assuming a Mg^{2+} value of 50 mM and $Mg/Ca^* = 10 \pm 3$, then $Ca^* = 4$ to 7 mM.

The initial concentrations of Ca^{2+} and SO_4^{2-} can be approximated from this range of Ca^* values. If the solubility product of Ca^{2+} and SO_4^{2-} is less than 25 mM, then, during the evaporation of seawater, halite will precipitate before $CaSO_4$. Since $CaSO_4$ precipitated in the Officer Basin after $CaCO_3$ and before halite, the product $(mCa^{2+})(mSO_4^{2-})$ was greater than 25 mM (Holland, 1984). Hence, the minimum possible value of Ca^{2+} is ~9 mM and the minimum possible value of SO_4^{2-} is ~3 mM. These values are also the lowest possible values of Ca^{2+} and SO_4^{2-} in the EQL/EVP simulations in which $CaSO_4$ precipitates before halite. Figure 3.3A shows that the calculated evaporation path of seawater with $(mCa^{2+})_i$ values between 9 and 12 mM includes most of the fluid-inclusion analyses. If the $(mCa^{2+})(mSO_4^{2-})$ product of Neoproterozoic seawater was in the vicinity of the $(mCa^{2+})(mSO_4^{2-})$ product of present-day seawater (~300 mM; Horita et al., 2002), then Ca^{2+} was ~19 ± 1 mM and SO_4^{2-} was ~13 ± 1 mM.

K^+ vs. Cl^- concentrations (Figure 3.3C) in the Browne Formation fluid inclusions indicate a low concentration of K^+ in the parent seawater. K^+ concentration in seawater throughout the Phanerozoic has remained relatively constant at ~10 mM (Horita et al., 2002). In the Browne Formation brine, which was evaporated 56-84 times beyond the concentration of modern seawater, K^+ concentrations ranged from 10-120 mM, much lower than expected if the parent seawater had K^+ anywhere near modern seawater values. Either Mid-Neoproterozoic seawater had lower K^+ values than modern seawater, or K^+ was removed from the brine during evaporative concentration and precipitation of potash salts.

The most precise way to estimate the Na^+ concentration of the parent seawater of the Browne Formation evaporites is the electrical neutrality constraint. Electrical neutrality demands a Na^+ concentration between 452-460 mM. As shown in Figure 3.3D, the evaporation path of seawater, with this narrow range of Na^+ concentrations, passes through the Na^+ concentration in the inclusion fluids.

We can then use the evaporation simulation EQL/EVP to predict the evolution of the evaporating Browne Formation brine with the following values serving as boundary conditions: Cl^- = 565-566 mM, $Mg^{2+} \leq 50$ mM, $K^+ < 10$ mM, $Ca^{2+} \geq 9$ mM, $SO^{2-}_4 \geq 3$ mM, and Na^+ = 452-460 mM (Table 3.2). We present the inferred major-ion compositions for Phanerozoic and Neoproterozoic seawater, as calculated from fluid-inclusion data, in Table 3.3.

TABLE 3.3 MAJOR-ION CONCENTRATIONS OF SEAWATER DETERMINED FROM FLUID-INCLUSION ANALYSES

	Age	Na^+	K^+	Mg^{2+}	Cl^-	Ca^{2+}	SO_4^{2-}
Modern[a]	0	485	11	55	565	11	29
Early-Late Cretaceous[b]	112.2-93.5	462	11	34	565	26	14
Early Cretaceous[b]	121-112.2	416	11	42	565	35.5	8.5
Late Jurassic[c]	150			28-33		20-26	7-14
Late Triassic[c]	230		9.3	28-32		16-17	13-14
Late Permian[a]	258-251	469	10	52	565	14	23
Mid Permian[a]	283-274	439	10	60	565	17	19
Lower Permian[a]	296-283	461	10	52	565	15	20
Mid Devonian[c]	380		10	31-41		25-35	5-11
Mid-Late Silurian[d]	428-416	445	12	48	601	35	11
Cambrian[e]	515	450	9	44	605	37	8
Late Proterozoic[e]	550	479	11	52	581	14	20.5
Mid-Neoproterozoic	830	456	1*	50	565	9-12	≥ 3

Note : Concentrations in mmol/kg H_2O.

Sources: [a]Lowenstein et al. 2005; [b]Timofeeff et al. 2006; [c]Horita et al. 2002; [d]Brennan and Lowenstein 2002; [e]Brennan et al. 2004

*Due to the likely loss of K^+ to late-stage salts, this may not be representative of K^+ in Neoproterozoic seawater

3.7 INTERPRETATION AND DISCUSSION

The relative concentrations of Ca^{2+} and SO_4^{2-} in Mid-Neoproterozoic seawater differed significantly from modern seawater. In modern seawater the concentration of SO_4^{2-} greatly exceeds the concentration of Ca^{2+}, and, on evaporation, the concentration of Ca^{2+} sharply decreases as a consequence of the precipitation of gypsum, anhydrite, and polyhalite while the concentration of SO_4^{2-} increases. The reverse was true for the parent brine of the Browne Formation and for seawater during much of the Phanerozoic (Table 3.3). While SO_4^{2-} levels were far below modern concentrations, there was enough available SO_4^{2-} in the oceans to support the deposition of extensive bedded marine sulfate evaporites, such as are found in the Browne Formation and Gillen Member.

The preservation of chevron structures shows that the halite has not recrystallized, and that the brines we analyzed were trapped as primary fluid inclusions at the time of crystal growth. Halite crystals also contain larger secondary fluid inclusions, not oriented with respect to primary growth bands and without evidence of the time of trapping. These secondary fluid inclusions are not suitable for reconstructing the composition of seawater; however, they may be used to determine the essential “flavor” of the parent brines, which will be either Ca-rich or SO_4-rich (Horita et al., 2002). Kovalevych et al. (2005) analyzed fluid inclusions of recrystallized halite from the coeval Gillen Member, Amadeus Basin. As in the Browne Formation, no SO_4^{2-} was detected in these fluid inclusions; thus the parent brine of the Gillen Member most likely had major-ion chemistry similar to that of the Browne Formation sampled from the Empress 1A and Lancer 1 cores. The halites sampled from the Gillen Member and Browne Formation cover an extensive area (Figure 3.1), supporting the inference that our calculated seawater chemistry establishes a global signature for the major-ion composition of Mid-Neoproterozoic seawater.

The K^+ concentration of the parent seawater during deposition of the Browne Formation cannot be reconciled with that expected from the evaporation of low-SO_4^{2-} seawater with a K^+ concentration of 10 mM. Even the evaporation of the low-K^+ seawaters NP1, NP2, and NP3 overestimates the observed concentration of K^+ in all but one of the Browne Formation samples

(Table 3.1; Figure 3.3C). The most likely explanation for the low K^+ concentration is the precipitation of late-stage potash minerals such as sylvite (KCl) and carnallite ($KMgCl_3 \cdot 6H_2O$). These late-stage salts are highly soluble, and thus their preservation is unlikely. These minerals are also absent from the Gillen Member; however, Kovalevych et al. (2005) reported the presence of two- and three-phase fluid inclusions containing sylvite in recrystallized halite from the Gillen evaporites. No known primary potash deposits have been reported from the Amadeus and Officer Basins. In addition, no K^+-bearing daughter crystals were found trapped in the Browne Formation fluid inclusions. EQL/EVP predicts that carnallite would be the next mineral to precipitate after halite from the Browne Formation brine; however, only several fluid inclusions, all measured from the same sample (depth 1,492 m), fall in the predicted carnallite zone. The very low concentration and the high variability of the K^+ concentration in the Browne Formation inclusion fluids demands the removal of K^+ from the evaporating seawater in the evaporite basin.

3.8 CONCLUSION

The analyses of fluid inclusions in primary halite deposited 830 million years ago reveal that the major-ion concentrations of Mid-Neoproterozoic seawater are in the range of Phanerozoic values. Mid-Neoproterozoic seawater was similar in composition to seawater at those times in the geologic past when the concentration of Ca^{2+} was greater than that of SO_4^{2-}, such as it was in Cambrian, Silurian, Devonian, Jurassic, and Cretaceous seawater. Variations in seawater chemistry documented throughout the Phanerozoic thus most likely began much earlier in Earth history.

Our results agree with other studies that suggest that Mid-Neoproterozoic marine sulfate concentrations were considerably lower, in the range of 2-10 mM, than the present-day value of 29 mM (Shen et al., 2002; Kah et al., 2004; Canfield et al., 2004). Based on our estimates of the major ions of Mid-Neoproterozoic seawater, we can constrain marine sulfate values to ≥ 3 mM. Marine sulfate levels did not approach modern values until the Late Neoproterozoic (Brennan et al., 2004), and most likely neither did atmospheric nor oceanic oxygen (Canfield et al., 2007; Fike et al., 2006; Frei et al., 2009).

CHAPTER 4: RE-EVALUATION OF THE δ^{34}S-ISOTOPIC COMPOSITION OF MARINE SULFATES FROM MID-NEOPROTEROZOIC EVAPORITES: NEW DATA FROM THE BROWNE FORMATION (~830 MA), OFFICER BASIN, AUSTRALIA.

4.1 ABSTRACT

We present sulfur-isotope measurements from primary anhydrite crystals trapped in primary, chevron halite samples of marine origin from the Mid-Neoproterozoic Browne Formation in the Officer Basin, Western Australia. In light of this new δ^{34}S-isotopic data from primary marine sulfates, the existing $\delta^{34}S_{sulate}$ data for the Mid-Neoproterozoic (~830 Ma) needs to be reexamined to identify samples from the dataset that were either non-marine in origin or altered by diagenetic processes. Results from the Browne Formation show a much narrower range of values (+14.8‰ to +15.9‰) than previously reported. The Browne Formation consists of bedded marine evaporites with minor sandstone and was sampled by the Empress 1A and Lancer 1 wells located ~264 km apart on the western platform in the western part of the Officer Basin. Using a combined approach of petrography, sedimentology, and geochemical analysis, we can establish the primary nature and marine origin of the anhydrites from the Browne Formation used to determine δ^{34}S. Thus we present a critical revision of the complete data set to refine the isotopic signature of seawater sulfate during Mid-Neoproterozoic time.

4.2 INTRODUCTION

The global sulfur cycle consists of three major sulfur reservoirs: sulfate dissolved in seawater, sulfate in ancient evaporites, and sulfide in marine sediments. Variations in the ratio of sulfur stable isotopes ($^{34}S/^{32}S$, expressed as δ^{34}S) in marine sulfates indicate changes in the fluxes and processes of the global sulfur cycle. Several of those processes produce consistent fractionation of the stable isotopes in marine sulfur (Bottrell and Newton, 2006).

The primary source of sulfur to the marine reservoir comes from the weathering of rocks. As sulfate-bearing rocks are uplifted and exposed to continental weathering processes, sulfate minerals, which are highly soluble, dissolve and re-enter the hydrologic cycle. Buried pyrite is

stable; however, once uplifted and exposed to oxygen it becomes unstable and weathers to sulfate in the presence of oxygen. The sulfate released by the dissolution of evaporites and produced during the weathering of pyrite is eventually transported via rivers back to the ocean. The flux of sulfate to the oceans produced by continental weathering processes has an average $\delta^{34}S$ of 0-10‰, compared to present-day seawater with $\delta^{34}S$ of +21.0‰ (Paytan and Gray, 2012). Other sources of marine sulfur include magmatic sulfur from both mid-ocean ridges and hydrothermal flow related to continental volcanism, which have an isotopic composition of 0-10‰.

Sulfate leaves the marine reservoir primarily as pyrite and by evaporitic precipitation of sulfate minerals. The dominant mechanism by which sulfate is lost from seawater is bacterial reduction (BSR). This sulfide, produced by BSR, combines with iron to form FeS and ultimately FeS_2 (pyrite), which is subsequently buried. BSR preferentially removes the lighter ^{32}S isotope producing sedimentary sulfide enriched in ^{32}S and depleted in ^{34}S relative to seawater sulfate. This leaves the residual sulfate enriched in ^{34}S. BSR produces consistent fractionation between the sulfur isotope composition of dissolved sulfate and pyrite, with magnitudes reaching 40-45‰, and in certain situations up to 70‰ (Canfield et al., 2010; Sim et al., 2011).

Precipitation of sulfate evaporites (mainly gypsum and anhydrite) also removes sulfate from the ocean, but aperiodically. During times of increased evaporite precipitation, sulfate removed from the ocean could affect the sulfate content of the oceans and the isotopic composition of marine sulfate (Wortmann and Paytan, 2012).

Precipitation of the principal evaporite sulfates does not cause substantial sulfur isotope fractionation (Thode and Monster, 1965; Raab and Spiro, 1991). Presently, seawater sulfate has a uniform $\delta^{34}S$ content of +21‰ (Paytan and Gray, 2012); sulfate in evaporated seawater shows a narrow range of $\delta^{34}S$ from +21‰ at the beginning of gypsum precipitation (Thode and Monster, 1965) to +19‰ at the end of halite precipitation (Raab and Spiro, 1991). Since sulfur fractionation is not significant during the precipitation of evaporite sulfates, the isotopic composition of ancient marine evaporite sulfates has been used to infer changes in the sulfur cycle in the ancient ocean,

assuming the sulfur isotopic composition of dissolved sulfate in seawater was homogeneous for a specific interval of time (Holland, 1978), and that the isotopic composition of ancient primary marine evaporites can be representative of the seawater from which they precipitated.

Deciphering the temporal evolution of oceanic sulfate from the $\delta^{34}S_{sulfate}$ of evaporites, especially from Precambrian deposits, can be problematic. The lack of fossils in some evaporite deposits makes biostratigraphic correlations and geochronology difficult. As evaporite deposition is discontinuous, and absent in some geologic periods, the isotope-age curves are fragmented. To avoid these problems inherent with evaporites, it is possible to determine the isotopic composition of carbonate-associated sulfate (CAS) in carbonates (Burdett et al., 1990), of phosphate-bound sulfate (McArthur et al., 1986; Shields et al., 1999), or of sulfate in marine barites (Paytan et al., 1998, 2004).

CAS is the trace quantity of sulfate that replaces carbonate ions in carbonate minerals. There are several advantages of using carbonates to reconstruct the sulfur-isotope record: 1) carbonate sequences are prevalent over wide geographic and temporal ranges, 2) those sequences often contain fossil assemblages that allow precise chronostratigraphic correlation, and 3) deposition of those sequences was often rapid and continuous allowing tight temporal control. However, it can be difficult to determine if the sulfate extracted from the sample is truly representative of the original CAS and not affected by pyrite contamination during sulfate extraction or diagenetic processes (Marenco, 2007; Marenco et al., 2008). To develop a robust record of the isotopic composition ($\delta^{34}S$) of seawater sulfate through geologic time requires a multi-proxy approach (Figure 4.1) (Solomon et al., 1971; Claypool et al., 1980; Hayes et al., 1992; Gorjan et al., 2000; Azmy et al., 2001; Paytan et al., 1998, 2004; Kampschulte and Strauss, 2004; Hurtgen et al., 2004; Ries et al., 2009).

Here we report sulfur-isotope measurements from primary anhydrite crystals trapped in primary, chevron halite samples of marine origin from the Mid-Neoproterozoic Browne Formation in the Officer Basin, Western Australia. We use an integrated approach, evaluating geochemical data within the context of petrography, sedimentology, and stratigraphy. The $\delta^{34}S$ of the Browne Formation anhydrites and their primary nature suggests that widely variable $\delta^{34}S$ values from the evaporites of the coeval Bitter Springs Formation of the Amadeus Basin, Australia, may be due to either non-marine origins or diagenetic alteration.

4.3 GEOLOGIC SETTING

The Amadeus and Officer Basins are two of several Neoproterozoic intracratonic basins that cover parts of Western, Northern, and Southern Australia (Figure 4.2). The Amadeus and Officer Basins formed after the Australian craton fused from several Archean and Proterozoic crustal blocks. Continental collision occurred between 1,300 and 1,100 Ma as part of the formation of the Rodinia supercontinent (Shaw et al., 1991; Myers et al., 1996). The basins are mostly asymmetric in cross-section and have relatively deep sub-basins or relict depocenters connected by troughs along one margin and a broad shallow platform along the opposing margin (Lindsay and Leven, 1996). Sedimentary successions in these intracratonic basins show similar stratigraphy and facies distributions allowing lithologic correlations (Grey et al. 2005).

In the Amadeus Basin, a basal sandstone unit of intertidal and fluvial deposits is assigned to the Heavitree Quartzite Formation and its southwestern equivalent, the Dean Quartzite Formation (Walter et al., 1995). Both overlie the highly deformed basement of the Arunta and Musgrave Blocks (Walter et al., 1995) (Figure 4.2). The basal sandstones are in turn overlain by the widespread carbonates and evaporites of the Bitter Springs Formation, which is subdivided into two members: the Gillen and Loves Creek Members. The Gillen Member consists of a dolomite unit interbedded with evaporite and clastic rocks, whereas the Loves Creek Member

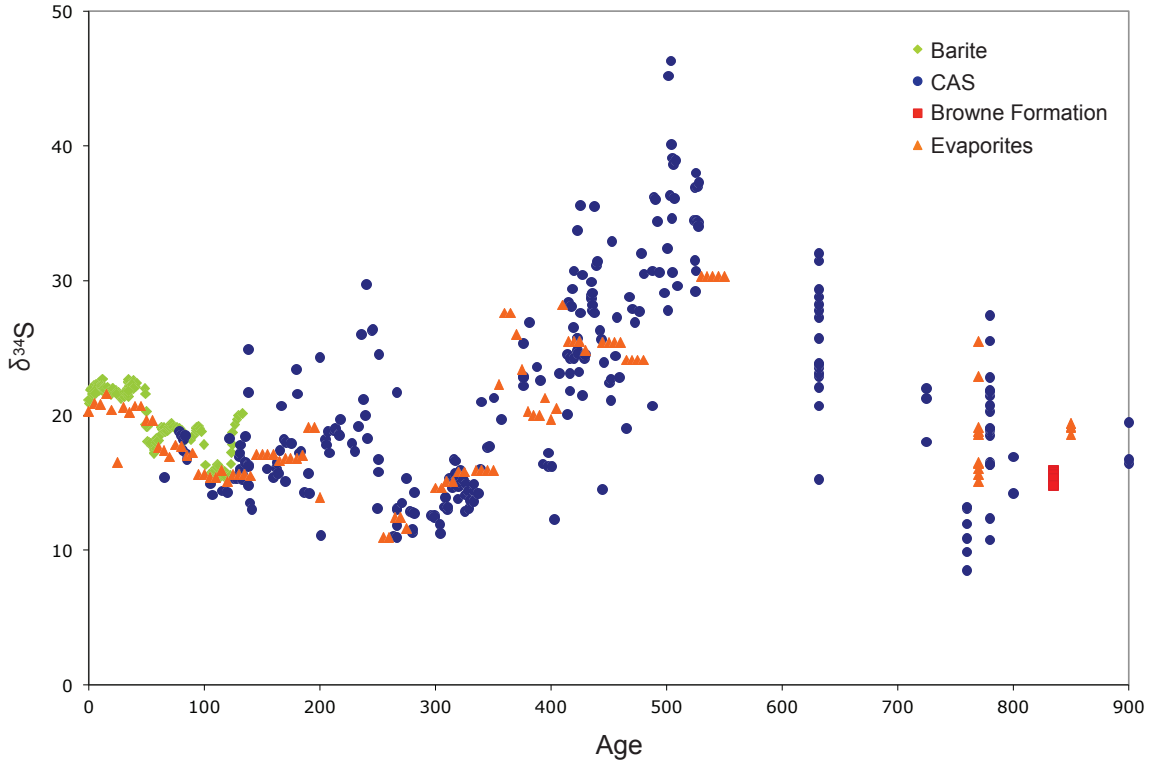

FIGURE 4.1 plots $\delta^{34}S_{sulfate}$ data from primary anhydrite trapped in halite crystals from the Browne Formation along with published sulfur isotope data determined from marine evaporites, sulfate in marine barites, and carbonate-associated sulfate (CAS). Sources: (Solomon et al., 1971; Claypool et al., 1980; Hayes et al., 1992; Gorjan et al., 2000; Azmy et al., 2001; Paytan et al., 1998, 2004; Kampschulte and Strauss, 2004; Hurtgen et al., 2004; Ries et al., 2009).

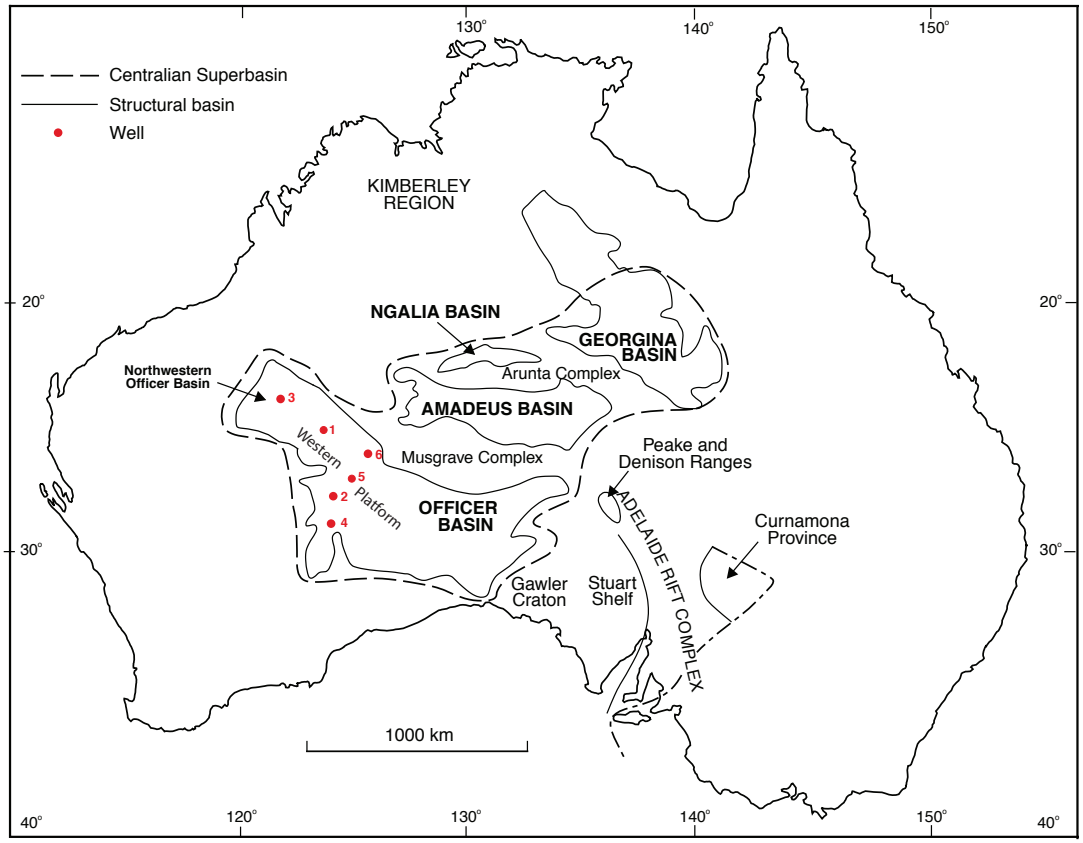

FIGURE 4.2 Locations of the Empress 1A and Lancer 1 drill cores on the tectonically stable Western Platform, Officer Basin, Western Australia. The cores are ~264 km apart. The Proterozoic intracratonic basins and Adelaide Rift Complex of Australia are outlined. Other wells identified include: (3) Boondawari 1, (4) NJD 1, (5) Kanpa 1, (6) Yowalga 3. Dashed line represents the extent of the Centralian Superbasin. Modified from Hill, 2005.

is a dolomitic unit interbedded with clastic and volcanic rocks (Wells et al., 1970). A main halite unit has been identified in several wells that intersect the Gillen Member (Lindsay, 1987; Young and Ambrose, 2007). Subsurface data indicate that salt is likely present under most, if not the entire basin. Thicknesses of salt vary significantly as a consequence of tectonic activity that caused the less-dense salt to flow between denser rocks resulting in structures such as, large salt-cored anticlines and diapirs (Lindsay, 1987). Estimates of salt thickness, based on current seismic data, range from ~200 m to a maximum of 4000 m in the Parrara Anticline (Young and Ambrose, 2007). The recovered halite is coarsely crystalline and brecciated, suggesting that it has been deformed by salt tectonics (Stewart, 1979; Dyson and Marshall, 2005; Kovalevych et al., 2006a).

In the western part of the Officer Basin, the basal sandstones consist of the Townsend Quartzite Formation, overlain by several carbonate and evaporite units: the Browne, Hussar, Kanpa, and Steptoe Formations. The Browne Formation and its lateral equivalents, the Mundadjini and Skates Formations found in the central part of the Officer Basin, consist of sandstone, dolomite, shale, and halite with minor anhydrite distributed through several transgressive and regressive cycles (Apak and Moors, 2000).

Using lithology, isotope stratigraphy, and biostratigraphy, both the Browne Formation of the Officer Basin and the Gillen Member of the Amadeus Basin have been correlated with other Neoproterozoic successions in Australia, Canada, Spitsbergen, and Namibia and assigned an age of ~830 Ma (Fanning et al, 1986; Wingate et al., 1998; Preiss, 2000; Hill et al., 2000; Hill and Walter, 2000; Walter and Hill, 1999; Grey, 2005; Eyles et al., 2007).

4.4 MATERIALS AND METHODS

Halite samples come from evaporite units recovered from the Empress 1A (27º03’13’’S, 125º09’24’’E) and Lancer 1 (25º02’44.5’’S, 123º45’20.1’’E) wells, located on the tectonically stable ‘western platform’ of the Officer Basin and separated by ~264 km (Figure 4.2). Structural dips in the western part of the Officer Basin are all less than 2°, and salt structures due to tectonic

activity are absent (Haines et al., 2004). Stratigraphic sections of the Browne Formation in both boreholes are shown in Figure 4.3. Moving northeast, toward the relict deeper portion of the basin, halite units of the Browne Formation have been intersected by the Kanpa 1A and Yowalga 3 wells; however, the halite was not recovered or preserved during the drilling process (Stevens and Apak, 1999; Apak and Moors, 2000). The samples we studied were collected from the base of the lower halite unit in the Empress 1A (from 1,472 to 1,522 m) and from the complete halite interval in the Lancer 1 well.

Mineral identification was performed by means optical and electron microscopy (SEM-EDS) and X-ray diffraction (XRD).

Because of the halite abundance and the presence of impurities, the sample treatment for isotopic analysis was as follows: core samples were cut with a diamond wire saw cooled with evaporating oil, washed with ethanol, crushed with a steel hammer, and ground to a fine powder in an agate mortar. Ten grams of powder were dissolved in 0.5 l of doubly-distilled water. The solution was filtered to eliminate insoluble impurities, acidified to pH 2 with 1 M HCl, and heated to the boiling point to remove dissolved carbonate. After cooling to room temperature, a solution of 0.25 M $BaCl_2$ was added in excess to precipitate the dissolved sulfate as $BaSO_4$. After 24 hours, the barium sulfate was filtered and washed in a vacuum flask using 0.2 μm membrane filters. The filtered powder was dried for 48 hours at 60 ºC.

SO_2 and CO_2 gas produced from $BaSO_4$ were mixed with V_2O_5 and graphite, respectively (Yanagisawa & Sakai, 1983). Analyses were done with a Mass Spectrometer (Finnigan MAT CHN 1108 Analyzer) for sulfur. The values are reported versus VCDT (Vienna Canyon Diablo Troilite) for $\delta^{34}S$. All samples were analyzed in duplicate and the analytical error (2σ), tested by the laboratory (Scientific and Technological Services of the University of Barcelona), was ~ ±0.40‰ for both determinations.

The bromine content of several rock-salt samples was determined using X-Ray Fluorescence with a Phillips PW2400 XR-Spectrometer. Samples and standards were measured on pressed powder tablets. Bromine standards were made with mixtures of KBr and NaCl ranging in concentration from 1.3 to 690 ppm. Analytical errors were below 5%. Selected halite crystals were powdered in ethanol to eliminate the contribution of the brines retained in fluid inclusions and grain boundaries (Moretto, 1988).

The major-ion chemistry of fluid inclusions in halite was analyzed using the Cryo-SEM-EDS technique (Ayora et al., 1994; Timofeeff et al., 2000; García-Veigas et al., 2009). Inclusions larger than 15 microns were analyzed for Na^+, Mg^{2+}, S (SO_4^{2-}), Cl^-, K^+, and Ca^{2+} using a SEM JEOL-840 with an EDS Si(Li) equipped with an INCA X-ray processor (Oxford Instruments Ltd.). Precision error is lower than 10%. The EQL/EVP computer program, based on the Pitzer ion-interaction model, was used to model the potential evaporation paths of the evolving parent brine (Risacher and Clement, 2001).

4.5 RESULTS

4.5.1 Mineralogy and petrology

The major rock types of the Browne Formation are dolomite, anhydrite, and halite with minor sandstone. The formation can be divided into three sections (A, B, and C), each deposited in a distinct paleoenvironment (Figure 4.3). In Empress 1A, section A (depth of 1,525-1,503 m) consists of layered dolomicrite, anhydrite, sandstone, and muddy halite. Section B (depth of 1,503-1,473 m) consists mainly of halite, interbedded with thin layers of dolomicrite and anhydrite, and thin beds of sandstone. Section C (depth of 1,473-1,460 m) of the Browne Formation consists of a chaotic mixture of large, clear halite crystals interbedded with mudstone and massive recrystallized halite, all lacking primary features.

Anhydrite is trapped as solid inclusions along growth bands of chevron halite crystals as well as along grain boundaries. Preservation of anhydrite within primary, non-recrystallized halite textures point to an original isotopic signature. Gypsum was not identified. Pyrite and other

sulfides do not occur in the Browne Formation, suggesting that bacterial sulfate reduction was not a significant mechanism during sedimentation and early diagenesis. Detrital quartz, potassium feldspar, and muscovite are also present; the clay fraction is minimal.

Horizontal surfaces may truncate the tops of the halite crystals (Figure 4.3: depth 1,482-1,472 m). These horizontal truncations are syndepositional dissolution surfaces caused by an influx of undersaturated water, and indicate that the sequence precipitated from a shallow, non-stratified brine body. If the brine were stratified, the lower density of the undersaturated water would prevent it from coming into contact with the halite located on the basin floor.

The evaporites of the Browne Formation display a general trend:

1. Deposition began in a shallow marine body in which carbonate and sulfate rocks were precipitated (Section A);
2. The marine waters became hypersaline, halite precipitated and accumulated in significant thicknesses (Section B);
3. the brine body evaporated further leading to desiccated conditions in which halite formed interstitially as mudstone accumulated (Section C) (Figure 4.3).

4.5.2 Bromine contents

The bromine (Br) values (avg. 102 ± 14 ppm) (Table 4.1) are in the range of those expected for halite precipitated from seawater (Valyashko, 1956; Holser, 1966; Braitsch, 1971; Siemann, 2003). The Empress 1A section shows a clear decreasing upward trend (from 122 to 73 ppm). Bromine content in samples from the Lancer 1 well fall in a very narrow range (from 111 to 107 ppm).

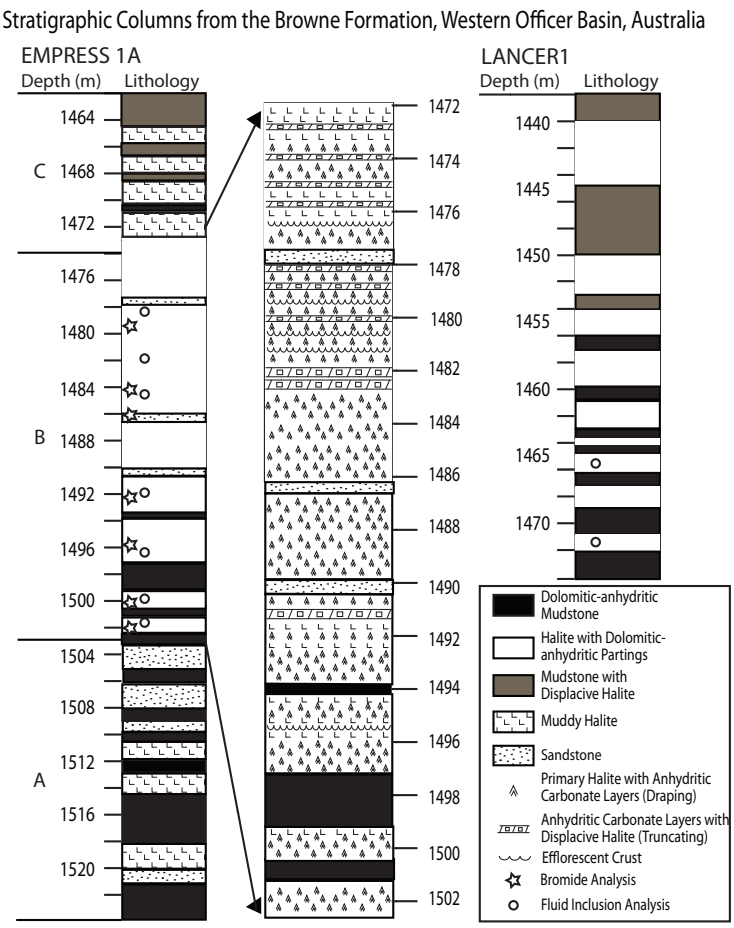

FIGURE 4.3 Measured sections of the Browne Formation from the Empress 1A well (~70 m) and from the Lancer 1 well (~44 m). The basic rock types of the Browne Formation are dolomite, anhydrite, halite, mudstone, and sandstone. Sections are divided on the basis of lithology and depositional environments.

TABLE 4.1 BROMINE VALUES FOR ROCK SALT AND SULFUR-ISOTOPE DATA FOR ANHYDRITE ($\delta^{34}S$)

Sample Depth (m)	Br (ppm)	δ34S (‰)
Empress 1A		
1479	73	15.2
1484.5	91	15.3
1486	87	15.4
1488.1		15
1488.4		15.2
1492	93	15.4
1494		15.1
1494.3		15.2
1496	103	15.5
1497		15.9
1498		15.1
1500	106	
1500.5		15.6
1501	119	
1501.4		15.1
1501.9		15.5
1502	122	
1502.1		15.3
1502.5		15.8
1504		14.9
1505		15.3
1506		15.4
1506.8		15.1
1507.8		15.2

1510		15
1513.3		15.6
1517		15.3
1523.2		14.8
Lancer 1		
1465.5	107	15.1
1471.5	111	15.5

4.5.3 Sulfate concentration (fluid inclusions)

The sulfate content of Mid-Neoproterozoic seawater can be calculated based on direct measurements of the other major-ion components present in seawater (Ca^{2+}, Mg^{2+}, Na^{+}, Cl^{-}, and K^{+}) (Spear et al., in preparation). The sulfate content of primary fluid inclusions was calculated for Empress 1A and Lancer 1 core samples (Figure 4.3). In all of the samples, the brines are sulfate-depleted with concentrations below the detection limit of the Cryo-SEM-EDS method (< 30 mM in a halite saturated brine which translates to < 3 mM in parent seawater).

This type of brine is consistent with the compositions of fluid inclusions reported by Kovalevych et al. (2006a) in recrystallized halite samples from the Bitter Springs Formation, Gillen Member in the Amadeus Basin.

4.5.4 Sulfate isotopes

Sulfur-isotope data for anhydrite ($\delta^{34}S_{sulfate}$) trapped as primary solid inclusions in halite crystals from Empress 1A and Lancer 1 drill cores (Table 4.1) fall in a very narrow range of +14.8‰ to +15.9‰ (avg. +15.3 ± 0.3 ‰, *n* = 26). There is no difference between the upper and lower part of the halite section in Empress 1A or between samples from the two wells.

4.6 INTERPRETATION AND DISCUSSION

4.6.1 Bromine

Seawater has greater Br concentrations than most non-marine waters; thus marine halite incorporates more Br and typically has higher Br values (65-300 ppm) than non-marine halite (Siemann, 2003). The Br content in halite from the Browne Formation is within the range of modern halite.

The upward-decreasing trend (Figure 4.4) recorded in the Br of the Empress 1A shows a transition from values typical of marine halite at a high degree of evaporation, close to the precipitation of potassium salts, to values expected for less concentrated marine brines. This

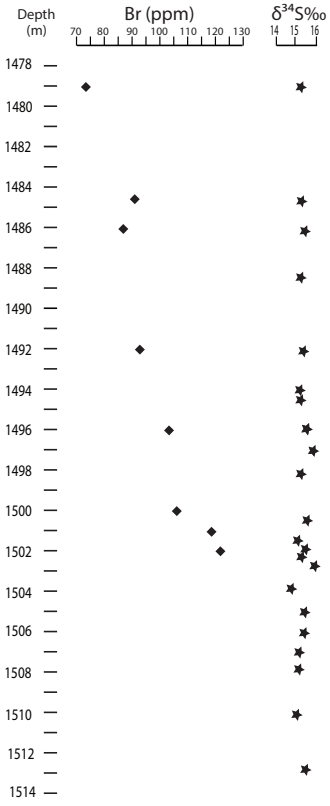

FIGURE 4.4 Geochemical profiles of the Empress 1A cored section. Br contents determined from halite and $\delta^{34}S_{sulfate}$ determined from primary anhydrite crystals.

transition could be the result of recycling by an influx of dilute water (either marine or meteoric). Petrographic evidence suggests an evolution from a hypersaline lagoon to a salt pan environment, in which previously precipitated and exposed halite was recycled by an influx of fresh water. The lack of variation in the vertical profile of the $\delta^{34}S$ isotopes indicates any incoming water had a similar sulfate-isotopic composition, thus it is likely that an influx of seawater is responsible for the recycled halite and for the decreasing Br concentration.

Kovalevych et al. (2006a) reported similar Br contents in halite from the Gillen Member of the Bitter Springs Formation, Amadeus Basin. They report three values (99, 102 and 132 ppm) supporting the interpretation that halite from the Gillen Member is of marine origin, and an anomalously low value (18 ppm) from a sample of recrystallized halite.

4.6.2 $\delta^{34}S_{sulfate}$

A compilation of previously published $\delta^{34}S_{sulfate}$ data from the Bitter Springs Formation in the Amadeus Basin (Table 4.2) shows a wide range, from +11.6‰ to +25.2‰, with an average value of +18.4‰, and a standard deviation of 3.3‰. The histogram plotting $\delta^{34}S_{sulfate}$ values from these published data (Figure 4.5) clearly illustrates that values below +13‰ and above +22‰ represent departures from the distribution. The values that fall in these outlying ranges come from samples that are non-marine or that were diagenetically altered (Wells et al., 1970; Gorjan et al., 2000; Kovalevych et al., 2006b). The locations of sampled wells are shown in Figure 4.6. We consider that a critical revision of the complete data set is necessary to evaluate the potential of the data to represent the isotopic signature of seawater during the deposition of the Browne Formation and Bitter Springs Formation. The data in question follow (Table 4.2):

1. Samples 25-26 and 29-31: Unit 3 (samples 25-26) and the lower part of Unit 2 (samples 29-31) of the Loves Creek Member of the Bitter Springs Formation (Wallara-1 well) are non-marine in origin. This determination is based on sedimentology and isotopic, elemental, and biomarker data (Wells et al., 1970; Hill et al., 2000a).
2. Samples 9 and 20-23: These samples from the Erldunda-1 and Ooraminna-1 wells yield a range of $\delta^{34}S_{sulfate}$ values that fall below +13‰ and above +22‰. These samples were diagenetically altered. Utrilla et al. (1992) and Lo Forte et al. (2005) state that the original

sulfur-isotope signal can remain unchanged during the diagenetic cycle (primary gypsum → anhydrite → secondary gypsum); however, this stability depends on the water-rock interaction of the fluids and bedrock during mineral replacement within a particular geologic context. These outlying values indicate that, during the recrystallization process, the original isotopic signature was not preserved. The altered isotopic signal could be the result of reaction with diagenetic fluids that were of a different age, origin, or chemical composition from the fluid responsible for the original sulfate precipitate.

These values listed above are either not marine or were altered by diagenetic processes and should not be considered as representative of the δ^{34}S-isotopic signature for the Bitter Springs Formation. Removal of the data described above provides a narrower range of $\delta^{34}S_{sulfate}$, from +15.3 to +20.1‰, with an average value of +17.6‰. This average value is lower than that previously proposed, and is closer to those obtained in this paper for the contemporary Browne Formation ($\delta^{34}S_{sulfate}$: +15.3 ± 0.3[1] ‰). Based on the above considerations and the petrologic and geochemical characteristics of the primary anhydrite crystals preserved in the primary rock salt of the Browne Formation, we propose to modify the data assigned to the Bitter Springs Formation from +11.6‰ to +25.2‰, with an average value of +18.4‰, to +15.3 to +20.1‰, with an average value of +17.6‰. We would then include the Browne Formation data (+14.8‰ to +15.9‰) in the isotope age curve (Figure 4.1[2]). With the inclusion of the Browne Formation, the average value becomes 16.4‰.

Assigning a specific $\delta^{34}S_{sulfate}$ value as a signature for any interval of geologic time requires analyses of samples from contemporaneous evaporite basins, as well as analyses of profiles from each deposit that are laterally and vertically representative (Nielsen, 1989). This poses a particular problem in Precambrian evaporites, which are relatively scarce and poorly dated. Thus, distinguishing between local and global isotope signals can be difficult. The evaporites of the Browne Formation and Bitter Springs Formation are indicative of a global signal

TABLE 4.2 PUBLISHED $\delta^{34}S_{SULFATE}$ DATA FROM THE BITTER SPRINGS FORMATION IN THE AMADEUS BASIN

Well	Depth (m)	Mineralogy	δ34S (‰)	**Reference**
Alice Springs AS-3				
1	64.9	Anhydrite?	17.4	Solomon et al., 1971
2	78.6	Secondary Gypsum	18.2	Gorjan et al., 2000
3	124.7	Anhydrite?	17.5	Solomon et al. 1971
4	218.2	Anhydrite?	20.1	Solomon et al. 1971
5	233.1	Secondary Gypsum	19.1	Gorjan et al., 2000
6	131.0	Gypsum	18.6	Hayes et al., 1992
7	131.0	Anhydrite	18.0	Hayes et al., 1992
Erldunda-1				
8	1460.0	Anhydrite?	16.6	Solomon et al. 1971
9	1600.2	Anhydrite?	11.6	Solomon et al. 1971
Mt. Charlotte-1				
10	1567.0	Secondary Gypsum	18.0	Claypool et al., 1980
11	1567.3	Secondary Gypsum	18.1	Gorjan et al., 2000
12	1614.2	Dolomite/Anhydrite	17.3	Gorjan et al., 2000
13	1652.0	Dolomite/Anhydrite	16.7	Gorjan et al., 2000
14	1652.0	Dolomite/Anhydrite	17.7	Gorjan et al., 2000
15	1944.0	Dolomite/Anhydrite	15.3	Gorjan et al., 2000
16	1946.0	Dolomite/Anhydrite	15.6	Gorjan et al., 2000
17	1777.0	Anhydrite?	19.0	Solomon et al., 1971
18	2011.7	Anhydrite?	16.6	Solomon et al., 1971
Ooraminna-1				
19	1353.3	Anhydrite?	19.7	Solomon et al., 1971
20	1505.7	Anhydrite?	25.2	Solomon et al., 1971
21	1505.0	Limestone/Anhydrite	24.3	Claypool et al., 1980
22	1592.0	Gypsiferous Shale	23.4	Claypool et al., 1980

23	1592.0	Gypsiferous Shale	23.1	Claypool et al., 1980
24	1858.0	Sulfate in Halite	16.4	Claypool et al., 1980
Wallara-1				
25	1538.3	Sulfate in Dolomite	21.7	Gorjan et al., 2000
26	1548.6	Sulfate in Dolomite	20.5	Gorjan et al., 2000
27	1796.5	Dolomite/Anhydrite	19.1	Gorjan et al., 2000
28	1910.3	Dolomite	17.3	Gorjan et al., 2000
29	1969.9	Anhydrite Nodule	25.1	Gorjan et al., 2000
30	1996.7	Siltstone/Anhydrite	11.8	Gorjan et al., 2000
31	2000.9	Dolomite/Anhydrite	12.7	Gorjan et al., 2000

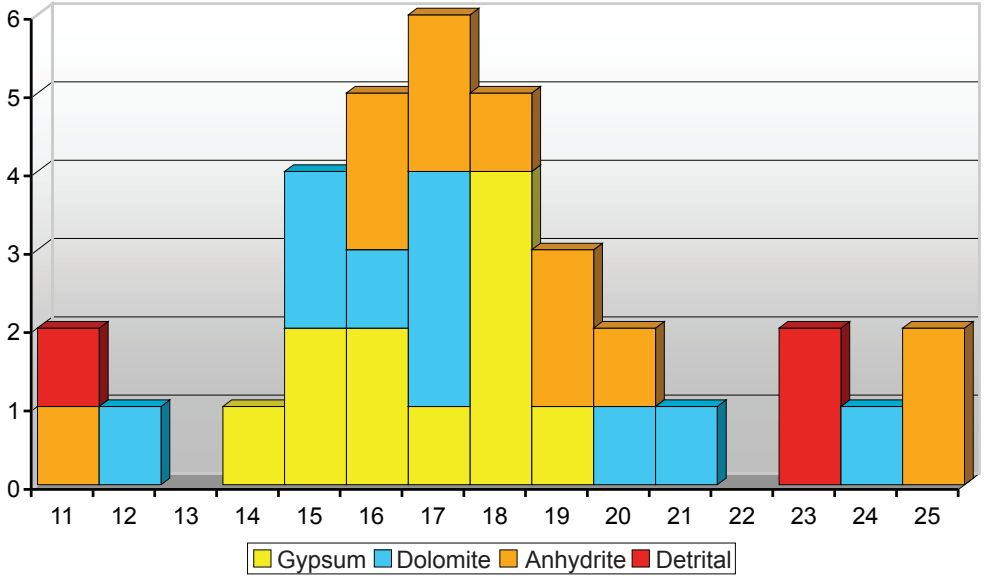

FIGURE 4.5 Histogram of sulfur isotopic $\delta^{34}S_{sulfate}$ of sulfate samples from the Bitter Springs Formation, Amadeus Basin. Data compiled by Solomon et al. (1971), Claypool et al. (1980), Hayes et al. (1992), and Gorjan et al. (2000).

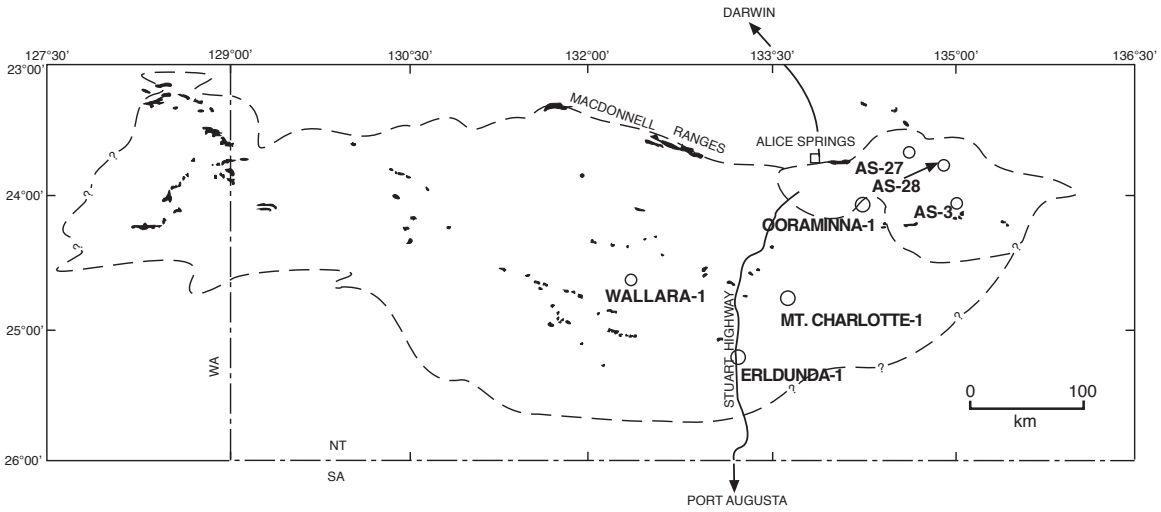

FIGURE 4.6 Location of the sampled wells for the Bitter Springs Formation, Amadeus Basin. Modified from Hill and Walter, 2000.

because of their widespread distribution (~500,000 km^2) and the remarkable similarities in characteristics and thicknesses of facies. Gorjan et al. (2000) report a value of +20‰ as representative of the sulfate isotopic signature of the Bitter Springs Formation and thus of Mid-Neoproterozoic time. Based on our new data from the Browne Formation and the revised data from the Bitter Springs Formation, an average value of +16‰ represents the $\delta^{34}S$-isotopic composition of Mid-Neoproterozoic seawater more accurately than the wider range previously reported.

4.7 SULFATE CONCENTRATION IN THE NEOPROTEROZOIC OCEAN

Reconstructing the size of the marine sulfate reservoir through geological time is important for interpreting the oxygenation history of the Earth, as the oxygen, carbon, and sulfur cycles are inextricably linked. The biogeochemistry of oxygen is directly related to that of sulfate, as low atmospheric oxygen levels suppress the oxidative weathering of sulfides and, ultimately, the delivery of sulfate to the oceans (Canfield et al., 2000). The timing and circumstances surrounding the growth of the sulfur and oxygen reservoirs through Proterozoic time are particularly intriguing, as they resulted in an irreversible increase in atmospheric oxygen and led to the emergence of complex life forms.

Recent studies of isotopic composition of coeval sulfides and sulfates through Archaean time (4,000 – 2,500 Ma) reveal small levels of fractionation between sulfate and sulfide, expressed as $\Delta^{34}S$ ($\delta^{34}S_{sulfate}$ - $\delta^{34}S_{pyrite}$), of generally <10‰ (Figures 4.7 and 4.8) (Canfield, 1998; Canfield, 2004; Hurtgen et al., 2005; Farquhar et al., 2010). Since fractionation becomes suppressed at low sulfate concentrations, Habicht et al. (2002) proposed that the lower levels of fractionation in the sulfur isotopes before 2,500 Ma was most likely the result of the activity of sulfate-reducing organisms in an ocean with a sulfate concentration lower than 200μM. The demise of mass-independent fractionation (MIF) of sulfur in early Paleoproterozoic time (~2,420 Ma) in sulfides and sulfates indicates that molecular O_2 levels had risen to several ppm during the "great oxygenation event" (Bekker et al., 2004; Guo et al., 2009; Holland, 2009). The oxygen

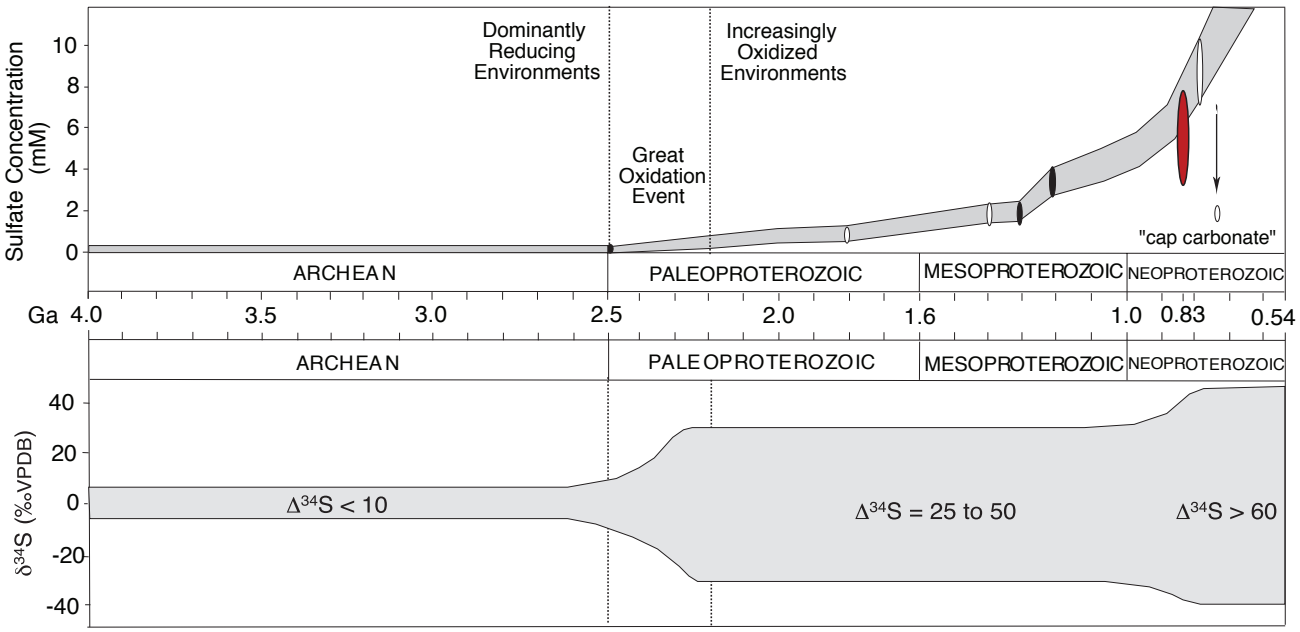

FIGURE 4.7 Proterozoic seawater sulfate concentrations based on model by Kah et al. (2004) to describe the variability of CAS-sulfur isotopes. Sulfate concentration for 0.84 Ga based on fluid-inclusion measurements. Maximum fractionations between sedimentary sulfide and sulfate minerals based on the compilation of Shen et al. (2001). From Kah et al., (2004) and Lyons et al., (2006).

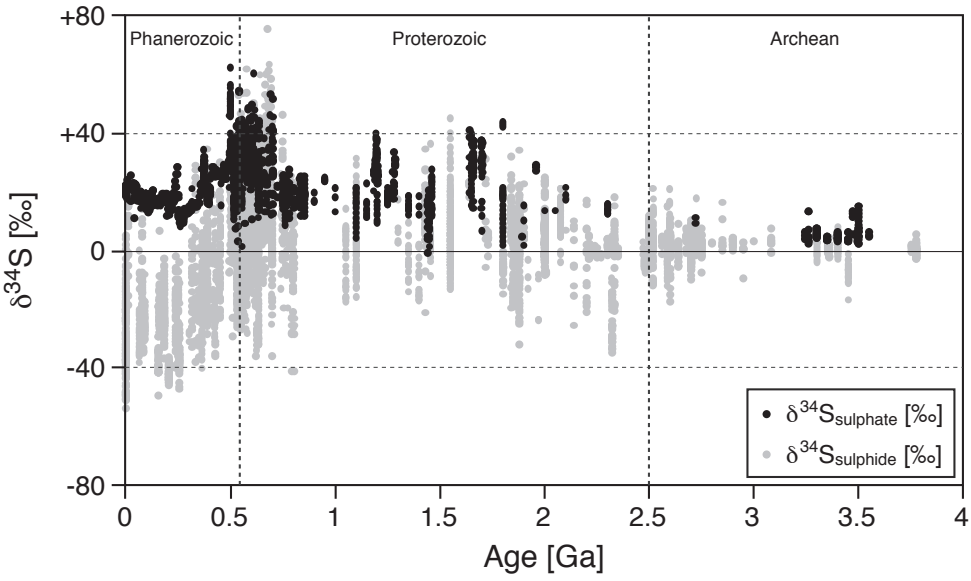

FIGURE 4.8 Compilation of sulfur isotopes measured in sulfate and sulfide minerals (values are not necessarily from coeval marine sulfates and sulfides). Archean $\Delta^{34}S$ values are <20‰, Paleo- and Mesoproterozoic $\Delta^{34}S$ values are <45‰, and Neoproterozoic $\Delta^{34}S$ values range between 40-70‰. From Och and Shields-Zhou, (2012) (Data references within).

produced by photosynthetic organisms was removed from the atmosphere by the weathering of reduced minerals, that upon delivery to the oceans, reacted with dissolved iron and formed the "banded iron formations". This increase in O_2 is further documented by the presence of sulfate-bearing marine evaporites in the sulfur reservoir after that time, accompanied by an in increase in $\Delta^{34}S$, reaching values as high as 40‰ (Shen et al., 2002; Pope and Grotzinger, 2003; Holland, 2009). Fractionation of this magnitude requires sulfate concentrations greater than 1mM, as sulfate fractionation and reduction rates are suppressed at sulfate concentrations below that level (Habicht et al., 2002). Oxygen levels were most likely high enough to bring about the weathering of pyrite to sulfate in soils, thus producing an enhanced source of sulfate to the oceans and a post-Archean rise in the sulfate content of seawater (Canfield, 2005).

The disappearance of banded iron formations in late Paleoproterozoic time (~1,800 Ma) is thought to signify a transition into an intermediary marine phase, neither completely anoxic nor completely oxic (Holland, 2006). Surface water was oxygenated at that time, while water in the deeper portions of the ocean remained anoxic and sulfidic, conditions persisted until the beginning of Neoproterozoic time (~1,000 Ma) (Farquhar et al., 2010; Planavsky et al., 2011; Poulton and Canfield, 2011; Rasmussen et al., 2012).

Pope and Grotzinger (2003) have compiled examples of Precambrian carbonate sequences up to 1,500 Ma in which deposition of evaporites proceeded directly from carbonate precipitation to halite precipitation, with no evidence of intervening gypsum or anhydrite precipitation. They hypothesize that, at low seawater-sulfate concentrations, halite may have precipitated before, or simultaneously with, gypsum. Sometime after 1,500 Ma, marine sulfate levels rose to levels sufficiently high enough to change the order of precipitation and support deposition of bedded sulfates.

Gypsum precipitation begins when the brine is concentrated by a factor of ~3.8, and halite precipitation begins when the brine is concentrated by a factor of ~10.6 (McCaffrey et al., 1987). The product of $(mCa^{2+})(mSO_4^{2-})$ in modern seawater is ~290 mM. The precipitation of

gypsum/anhydrite occurs at greater degrees of evaporation as the product of (mCa^{2+})(mSO_4^{2-}) decreases (Holland, 1984). If the product of (mCa^{2+})(mSO_4^{2-}) is reduced to < 25 mM, then saturation with respect to gypsum and halite is reached simultaneously (Holland, 1984). This is approximately the minimum possible value of the product of (mCa^{2+})(mSO_4^{2-}) in seawater with salinity similar to that of the modern ocean (35 gm/kg solution), in which gypsum will precipitate before halite (Holland, 1984). Since gypsum/anhydrite deposits occur in the rock record before halite in both the Browne Formation and the Gillen Member, we estimate that the product of (mCa^{2+})(mSO_4^{2-}) in Mid-Neoproterozoic (~850 Ma) seawater was greater than 25 mM.

We measured the major-ion composition (Ca^{2+}, Na^{+}, Mg^{2+}, K^{+}, and Cl^{-}) of Mid-Neoproterozoic seawater trapped in primary fluid inclusions in primary halite of the Browne Formation. Based on our direct measurements and the evaporation paths generated by the equilibrium chemical program EQL/EVP (Risacher and Clement, 2001) that best fit the fluid-inclusion data, we estimate that the sulfate concentration in Mid-Neoproterozoic seawater was ≥ 3 mM (Spear et al., in preparation). This is in the range of other studies that use isotopic evidence to support the inference that low levels of marine sulfate prevailed over much of Neoproterozoic time (Shen et al., 2002; Kah et al., 2004; Canfield, 2004; Fike et al., 2006; Hurtgen et al., 2006).

Carbonate Associated Sulfate (CAS) isotope data and fractionation ratios between coeval sulfate and sulfides were reported by Kah et al. (2004) to construct the SO_4^{2-} concentration curve through the Proterozoic ocean. Kah et al. (2004) calculate that marine-sulfate concentrations remained below 2 mM until about 1,300 Ma, rose to ~4.5mM by 1,200 Ma, and rose as high as 6-8 mM by Mid-Neoproterozoic time, with the possibility of a sudden drop during the Neoproterozoic glacial intervals (750-580 Ma), which are proposed to have been represented by a near-complete reduction of oceanic sulfate. CAS data from carbonates older than 1,000 Ma and carbonates deposited close to the glacial intervals reveal large, systematic shifts in $\delta^{34}S$ of up to 15‰ through several hundred meters of rock section (Kah et al. 2004). Isotopic variation as rapid as this is less common in Neoproterozoic and younger strata, suggesting that seawater-sulfate levels were high

enough to buffer against this type of isotopic variation. The narrow range of $\delta^{34}S_{sulfate}$ values measured from the Browne Formation suggests that, while seawater-sulfate levels during deposition of the Browne Formation were lower than present-day values, seawater-sulfate concentrations were high enough to buffer against the rapid isotopic variation documented by Kah et al. (2004) in older rock sections.

The parameters in the model used by Kah et al. (2004) were chosen to maximize the marine sulfate concentration for any given time[3]. Thus their predicted values of 6-8 mM for Mid-Neoproterozoic seawater represent maximum sulfate levels and allow us to place a tight constraint of ≥ 3 mM but ≤ 8mM on sulfate values for Mid-Neoproterozoic seawater. This is in the range of values previously predicted for Neoproterozoic seawater based on geochemical proxies such as CAS (Shen et al., 2002; Kah et al., 2004; Canfield et al., 2004; Fike et al., 2006; Hurtgen et al., 2006).

Fractionation data for Proterozoic rocks is scarce. This lack of data has been attributed to several possible factors, including increased pyrite burial, subduction of buried pyrite, and limited pyrite formation in low-sulfate oceans (Canfield, 2004; Lyons, 2008; Shen et al., 2008; Farquhar et al., 2010). $\Delta^{34}S$ values of ~40‰ are reported for much of Neoproterozoic time, including 840-830 Ma (Shen et al., 2001). Pyrite has not been found in the Browne Formation. Gorjan et al. (2000) report $\delta^{34}S_{pyrite}$ values between -13.5‰ and -0.3‰, with a mean value of -7.1‰ for the Gillen Member and values between -14‰ and +23.4‰, with a mean value of +8.1‰, for the Loves Creek Member. This puts the range of $\Delta^{34}S$ for the Bitter Springs Formation, and thus the Browne Formation, between 30-40‰.

Sometime after ~600 Ma, fractionation values increase to a range of 40-70‰ (Farquhar et al., 2010; Och and Shields-Zhou, 2012). Fluid-inclusion data indicate that around this time, marine sulfate levels increased. Direct measurements from primary halite of the Ara Formation in Oman indicate higher sulfate levels in the terminal Proterozoic oceans (~550 Ma) (Horita et al., 2002; Brennan et al., 2004). Sulfate levels were much lower in the Mid-Neoproterozoic oceans

(~830 Ma). Based on $\delta^{34}S_{sulfate}$ values from the Browne Formation (+15.3 to +20.1‰) and $\delta^{34}S_{sulfide}$ values from the Bitter Springs Formation (-14‰ to +23.4‰) (Gorjan et al., 2000), we can confirm that sulfide-sulfate fractionation had not yet approached the levels documented for the end of Proterozoic time (~550 Ma).

4.8 CONCLUSION

By using an approach that integrates geochemical with petrographic, sedimentologic, and stratigraphic analyses, the range of $\delta^{34}S_{sulfate}$ isotope data can be refined to accommodate all constraining analytical parameters. According to the petrographic and geochemical information provided in the literature, we propose here to remove from consideration some of the published isotopic data that have been affected by diagenesis, are not of marine origin, and are of uncertain age; therefore they are not representative of the isotopic composition of Mid-Neoproterozoic seawater. Based on these considerations, we propose to modify the sulfur-isotope data assigned to the Bitter Springs Formation from +11.6‰ to +25.2‰, with an average value of +18.4‰, to +15.3‰ to +20.1‰, with an average value of +17.6‰. Based on the petrologic and geochemical characteristics of the primary anhydrite crystals preserved in the primary rock salt of the Browne Formation, we add the Browne Formation data (+14.8‰ to +15.9‰) to the isotope age curve along (Figure 4.1). Based on our new data from the Browne Formation and the revised data from the Bitter Springs Formation, an average value of +16‰ more accurately represents the average $\delta^{34}S$-isotopic composition of Mid-Neoproterozoic seawater. These values allow us to impose a tighter constraint on the $\delta^{34}S_{sulfate}$ isotope signature for Mid-Neoproterozoic time.

CHAPTER 5: CONCLUDING REMARKS

5.1 OVERVIEW

In this project, I completed a comprehensive sedimentologic, petrographic, and geochemical analysis of the evaporite rocks of the Mid-Neoproterozoic Browne Formation. This is the first study to use a comparative sedimentological approach to describe the evaporites of the Browne Formation. With this multi-tiered approach, I was able to confirm the marine origin of the evaporites and that the halite was primary and not altered by diagenetic processes.

It was essential to establish the primary nature of the halite of the Browne formation to complete my primary research goals 1) to determine the major-ion composition of Mid-Neoproterozoic seawater, and 2) to determine the isotopic signature of seawater sulfate for this time period.

I showed that seawater chemistry during Mid-Neoproterozoic time was very different from present-day seawater chemistry; the concentration of Ca^{2+} exceeded that of SO_4^{2-}, such as it did in Cambrian, Silurian, Devonian, Jurassic, and Cretaceous seawater. I extended the record of seawater chemistry from ~544 Ma to ~830-840 Ma. My research confirms that the Neoproterozoic was a time low marine sulfate with concentrations around 3mM. I determined the isotopic signature of seawater sulfate for Mid-Neoproterozoic time is in the range of +14.8‰ to +15.9‰. I identified a range of values in the literature that do not represent a primary, marine $\delta^{34}S_{sulfate}$-signature (+11.6‰ to +25.2‰, with an average value of +18.4‰), and by removing those values that were diagenetically altered or not indicative of a marine environment, I narrowed the range of acceptable values for the Mid-Neoproterozoic to +14 to +21‰, with an average value of +16.8 ± 1.3‰.

5.2 SIGNIFICANCE OF WORK

My research offers far-reaching implications for students of Proterozoic marine-sulfate and oxygen levels, and for those who study the chemical co-evolution of the early oceans, atmosphere, and biosphere. Because most of the sulfate in the ocean is derived from continental weathering of sulfide minerals beneath an atmosphere containing free oxygen, the systematic rise of sulfate concentrations in seawater tracks the oxygenation of the Proterozoic atmosphere. These data make it possible to explore the relationships between the major-ion chemistry of seawater and the evolution of marine life during this important interval of Earth history.

5.3 FUTURE WORK

5.3.1 Seawater Chemistry

I recently obtained a sample of halite from Dr. Dick Holland from a drill core in the Onega structure, Karelia, Russia. The halite unit lies below the Paleoproterozoic Ulitin Formation, both of which are newly discovered. The halite unit is 194 m thick; its age is estimated to be 2.13 Ga. Initial petrographic analysis with electron microscopy determined the presence of K-bearing minerals. Based on this discovery, I plan to work with Dr. Harrison of UCLA to date the sample using ^{40}K-^{40}Ca dating methods. The sample I currently have is completely recrystallized and not suitable for fluid-inclusion analysis. I plan to obtain more samples to describe the sedimentology and petrography in hopes of finding samples appropriate for fluid-inclusion analysis.

5.3.2 Isotopic Composition of Seawater Sulfate

I was able to significantly constrain the range of values for the isotopic composition of seawater sulfate for Mid-Neoproterozoic time. I am interested to see if values from carbonate associated sulfate (CAS) in coeval carbonate deposits fall in the same range. I plan to determine the $\delta^{34}S$-isotopic composition using CAS of coeval carbonate deposits from suitable samples obtained from the Officer and Amadeus Basins of Australia, and from the Shaler Supergroup of Canada.

APPENDIX I: SUPPLEMENTARY METHODS

1.1 SUPPLEMENTARY METHODS FOR CHAPTER 2

1.1.1 X-Ray Diffraction

I used X-Ray-powder diffraction to identify crystalline materials. Samples were prepared using an agate mortar and pestle. The fine powder was mounted on a slide and analyzed using the Phillips X-pert MPD instrument located at the University of Binghamton. The samples were scanned at a step size of 0.05° and 75.00° (2θ), λ 1.54055 Å. X'Pert High Score software was used to determine peak parameters.

1.1.2 Thick and Thin Section Preparation

I prepared thick and thin sections at the University of Binghamton, NY, using a .310mm diamond wire saw; I mounted the thin sections on glass slides with a clear epoxy.

1.1.3 Optical and Electron Microscopy

I used conventional optical and environmental scanning electron microscopy (ESEM FEI Quanta) with an energy-dispersive microanalysis attachment (EDAX-Genesis) to determine textural characteristics and mineral associations. I used the thin and thick sections I prepared at the University of Binghamton for all microscopy work. I performed the ESEM work at the Scientific and Technological Centers at the University of Barcelona, Spain.

1.1.3 Constructing the Measured Section

I constructed a detailed measured section on the cm-m scale using data and observations gained from study of core samples, core photos, XRD analysis, and optical and electron microscopy. I sampled 70 m of core from the Empress 1A well and 50 m of core from the Lancer 1 well; both cores were drilled by the Geological Survey of Western Australia.

1.2 SUPPLEMENTARY METHODS FOR CHAPTER 3

1.2.1 Fluid-Inclusion Analysis

I determined the major-ion chemistry of fluid inclusions in halite using the Cryo-SEM-EDS (scanning electron microscopy with energy dispersive spectrum) technique (Ayora et al., 1994; Timofeeff et al., 2000; García-Veigas et al., 2009). Inclusions larger than 15 microns were analyzed for Na^+, Mg^{2+}, S (SO_4^{2-}), Cl^-, K^+, and Ca^{2+} using a SEM JEOL-840 with an EDS Si(Li) coupled with a Cryostage Oxford CT-1500 C and equipped with an INCA X-ray processor (Oxford Instruments Ltd.). I performed these analyses at the Scientific and Technological Centers at the University of Barcelona, Spain.

I placed a slice of halite containing chevron fluid inclusions and measuring about 1 cm^2 by 1 mm thick, together with four microdroplets of standard solutions, in a sample holder. I immersed the sample holder in liquid N_2 and introduced it, with a cryo-transfer system under vacuum, to the cryostage at − 170 °C. I then cleaved the halite slice inside the cryochamber, exposing a flat and pristine cross section of halite with frozen fluid inclusions. I coated the frozen droplets of standard solutions and the halite slice with aluminum (b10 nm) in order to prevent electric charging. Next, I transferred the sample holder to the main chamber of the SEM at a temperature lower than −190 °C in high vacuum conditions (10^{-4} Pa). EDS analyses were carried out under optimized working conditions (accelerating voltage: 15kV; beam current intensity: 1.5 nA; counting time: 200 s). Quantitative analysis of each element was based on the peak-to-background X-ray intensity ratio of the EDS corresponding K_α line. I obtained fluid-inclusion concentrations by comparing the peak-to-background ratio of each individual inclusion with the linear regression calculated for the four standard solutions. The standard solutions were prepared gravimetrically with NaCl, KCl, $MgCl_2.6H_2O$, $MgSO_4.7H_2O$, and $CaCl_2.2H_2O$ and distilled water within the range of composition expected in the inclusions. Calculated errors include the precision error (standard deviation with regard to the mean) and the error derived from the regression method (correlation coefficients N 0.90). The analytical error was lower than 10% (Ayora et al., 1994), and the detection limits (in mol/kg H_2O) for the present study were determined to be 0.01 for K and Ca, 0.03 for SO_4 and Mg, and 0.35 for Na.

1.3 SUPPLEMENTARY METHODS FOR CHAPTER 4

1.3.1 Methods for Isotopic Analysis

Because of the halite abundance and the presence of impurities, the sample treatment for isotopic analysis was as follows: core samples were cut with a diamond wire saw cooled with evaporating oil, washed with ethanol, crushed with a steel hammer, and ground to a fine powder in an agate mortar. Ten grams of powder were dissolved in 0.5 l of doubly-distilled water. The solution was filtered to eliminate insoluble impurities, acidified to pH 2 with 1 M HCl, and heated to the boiling point to remove dissolved carbonate. After cooling to room temperature, a solution of 0.25 M $BaCl_2$ was added in excess to precipitate the dissolved sulfate as $BaSO_4$. After 24 hours, the barium sulfate was filtered and washed in a vacuum flask using 0.2 µm membrane filters. The filtered powder was dried for 48 hours at 60 ºC. Dr. Javier García-Veigas performed the isotopic analyses at the Scientific and Technological Centers at the University of Barcelona, Spain.

1.3.2 Method to determine Bromine Contents in Halite

Selected halite crystals were powdered in ethanol to eliminate the contribution of the brines retained in fluid inclusions and along grain boundaries (Moretto, 1988). Bromine contents in salt samples were determined by X-ray fluorescence with a Phillips PW2400 XR-Spectrometer. Samples and standards were measured on pressed-powder tablets. Bromine standards were made with mixtures of KBr and NaCl ranging in concentration from 1.3 to 690 ppm. Analytical errors were below 5%.

1.3.2 Method to determine $\delta^{34}S_{sulfate}$

Anhydrite dispersed in halite from the bedded units was dissolved and precipitated as $BaSO_4$ from boiling water at pH ~3. The $\delta^{34}S_{V\text{-}CDT}$ was determined with a Carlo Erba 1108 elemental analyzer coupled to an IRMS Thermo Finnigan Delta Plus XP. The analytical error (2σ) was ±0.2‰ for $\delta^{34}S$.

SO_2 and CO_2 gas produced from $BaSO_4$ were mixed with V_2O_5 and graphite, respectively (Yanagisawa & Sakai, 1983). Analyses were done with a Mass Spectrometer (Finnigan MAT CHN 1108 Analyzer) for sulfur. The values are reported versus VCDT (Vienna Canyon Diablo Troilite) for $\delta^{34}S$. All samples were analyzed in duplicate and the analytical error (2σ), tested by the laboratory (Scientific and Technical Services of the University of Barcelona), was ~ ±0.4‰.

APPENDIX II: SUPPLEMENTARY DATA

2.1 SUPPLEMENTARY DATA FOR CHAPTER 2

2.1.1 Table with results from XRD and ESEM analysis.

Depth (m)	Sample	XRD	ESEM
1467.3	307-4-5	Quartz, Anhydrite, Dolomite	
	307-4-5	Halite, Quartz, Anhydrite, Kaolinite	
	307-4-9	Halite, Quartz, Anhydrite, Kaolinite	
1471	307-5-2		Fe-oxide, Quartz, K-Feldspar, Anhydrite
1471.8	308-2-6	Halite	
	308-3-4	Quartz, Dolomite, Kaolinite	
	308-5-7	Anhydrite, Kaolinite-Montmorillonite, Halite, Quartz	
1476	308-5-8		Quartz, K-Feldspar, Anhydrite, Fe-oxide
1479	309-4-1		Zircon, K-Feldspar, Fe-oxide, Dolomite, Anhydrite, Quartz
	310-2-8	Dolomite, Anhydrite, Quartz	
1482	310-3-1	Halite	
		Quartz, Halite, Kaolinite	Quartz, Fe-oxide, Anhydrite, K-Feldspar, Dolomite
1485	310-5-4		Fe-oxide, Quartz, Anhydrite, K-Feldspar
1485.5	311-1-1		Dolomite, Quartz, Silicates, Anhydrite, Fe-oxide
	311-2-3	Halite, Anhydrite	
	311-2-3	Anhydrite, Quartz, Dolomite, Halite	

	311-2-4	Halite, Anhydrite	
1489.9	312-3-3	Anhydrite, Quartz, Dolomite, Halite	
	312-3-1	Halite, Dolomite, Anhydrite	
		Quartz, Anhydrite, Dolomite	
1494.6	E26	Halite, Anhydrite	
	E20		K-Feldspar, Quartz, Anhydrite, Dolomite
	E10	Halite, Quartz, Dolomite	
	E6	Anhydrite, Dolomite	
	E6	Anhydrite, Hal, Quartz, Dolomite	
1499.5	D15		Quartz, Mica, K-Feldspar, Anhydrite
	D10	Halite, Anhydrite, Dolomite, Quartz	
1500	D9		Anhydrite, Dolomite
	D3	Anhydrite, Quartz, Dolomite	
1501.7	C8	Anhydrite, Dolomite, Quartz	
	C4	Anhydrite, Quartz	
	C2		Dolomite, Anhydrite, Zircon, K-Feldspar, Illite
1511.3	B7	Halite, Anhydrite, Dolomite, Quartz	
1520	A20		Anhydrite, Dolomite, Quartz, K-Feldspar

2.1.2 X-Ray Diffractograms

Corresponding sample depths are labeled in the top left corner of each diffractogram.

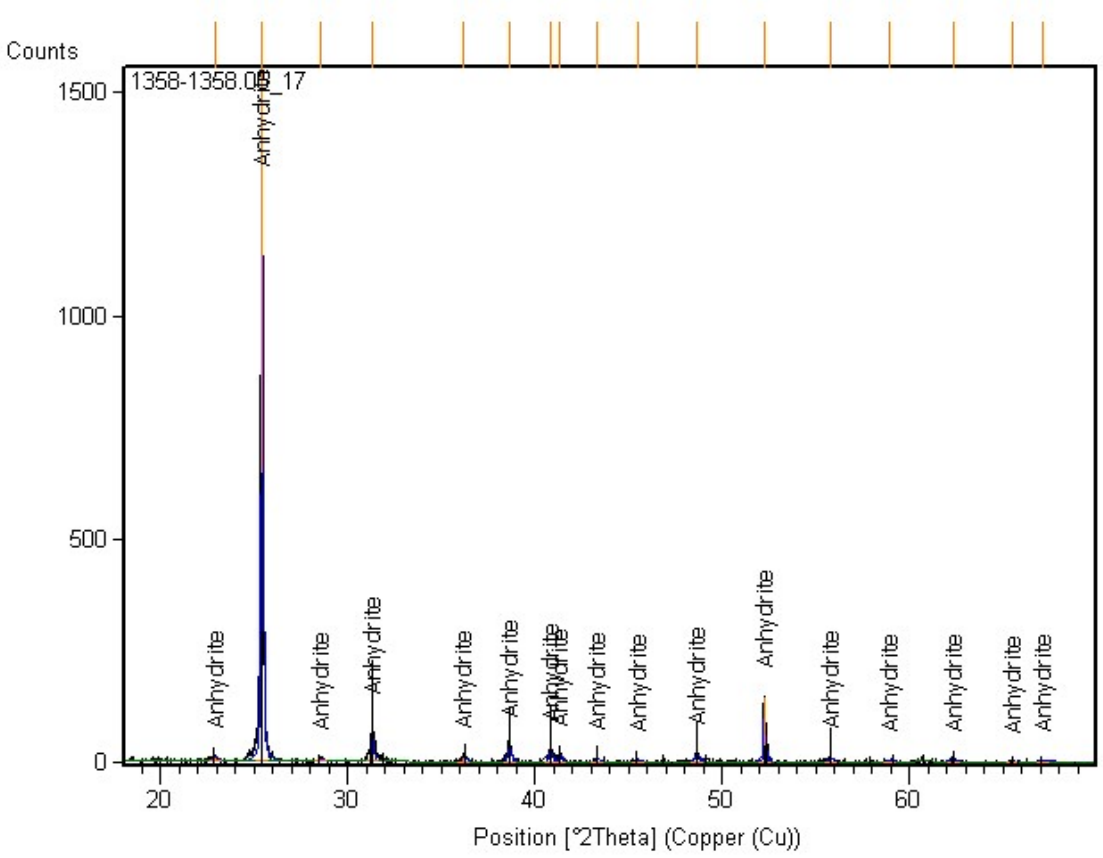

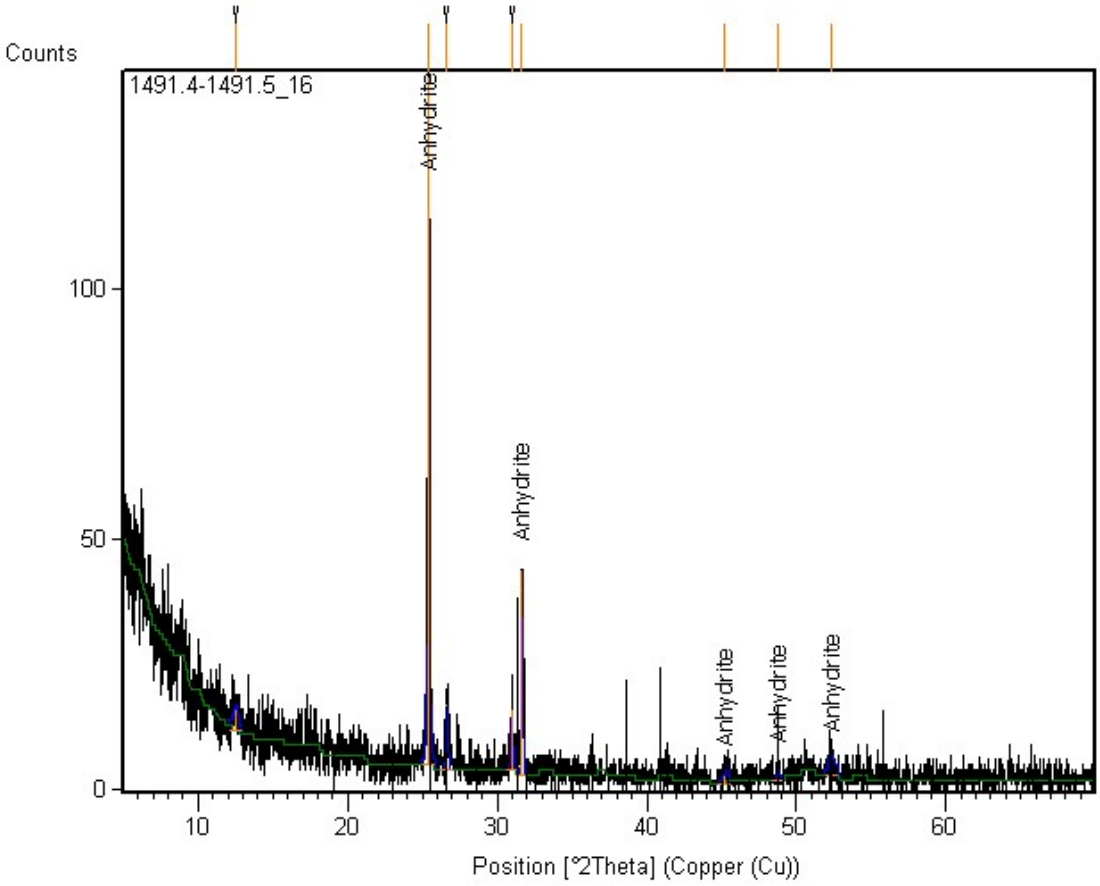
Counts
1491.4-1491.5_16
Anhydrite
Anhydrite
Anhydrite
Anhydrite
Anhydrite
100
50
0
10
20
30
40
50
60
Position [°2Theta] (Copper (Cu))

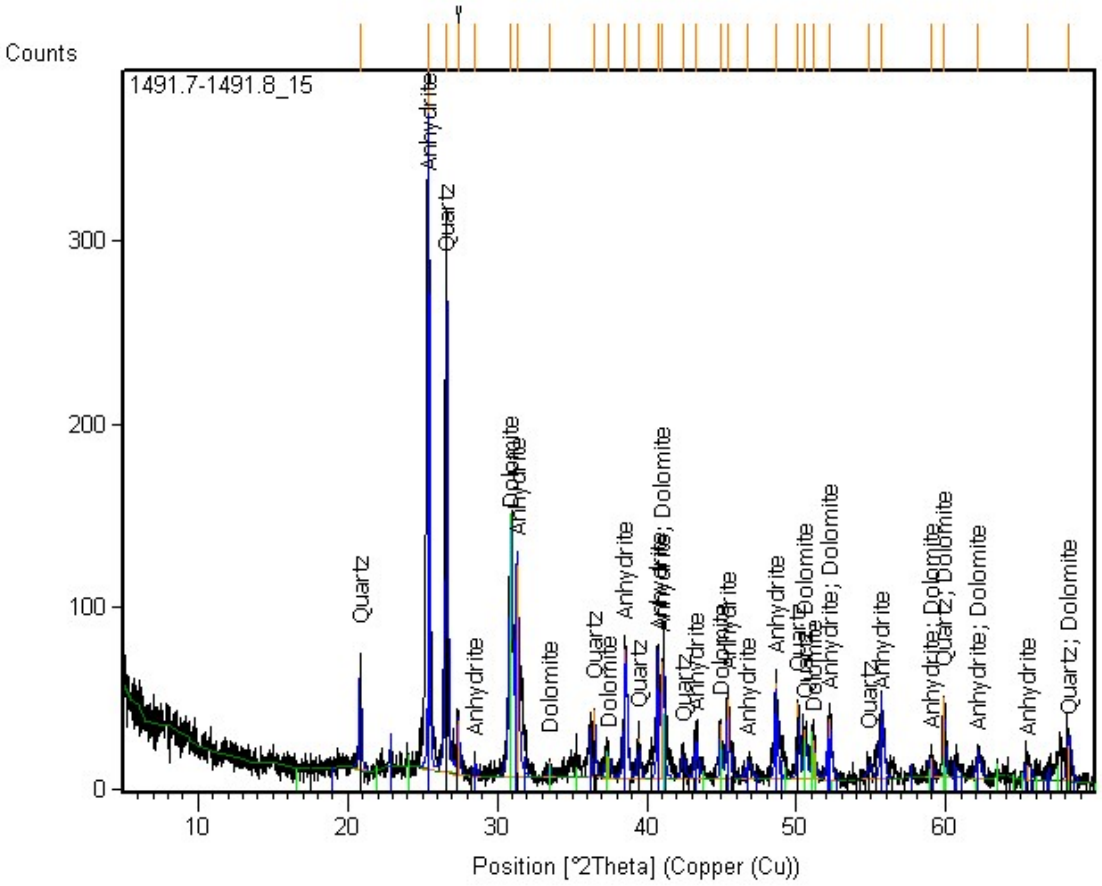
Counts
1491.7-1491.8_15
300
200
100
0
10
20
30
40
50
60
Position [°2Theta] (Copper (Cu))
Quartz
Anhydrite
Dolomite
Anhydrite; Dolomite
Quartz; Dolomite

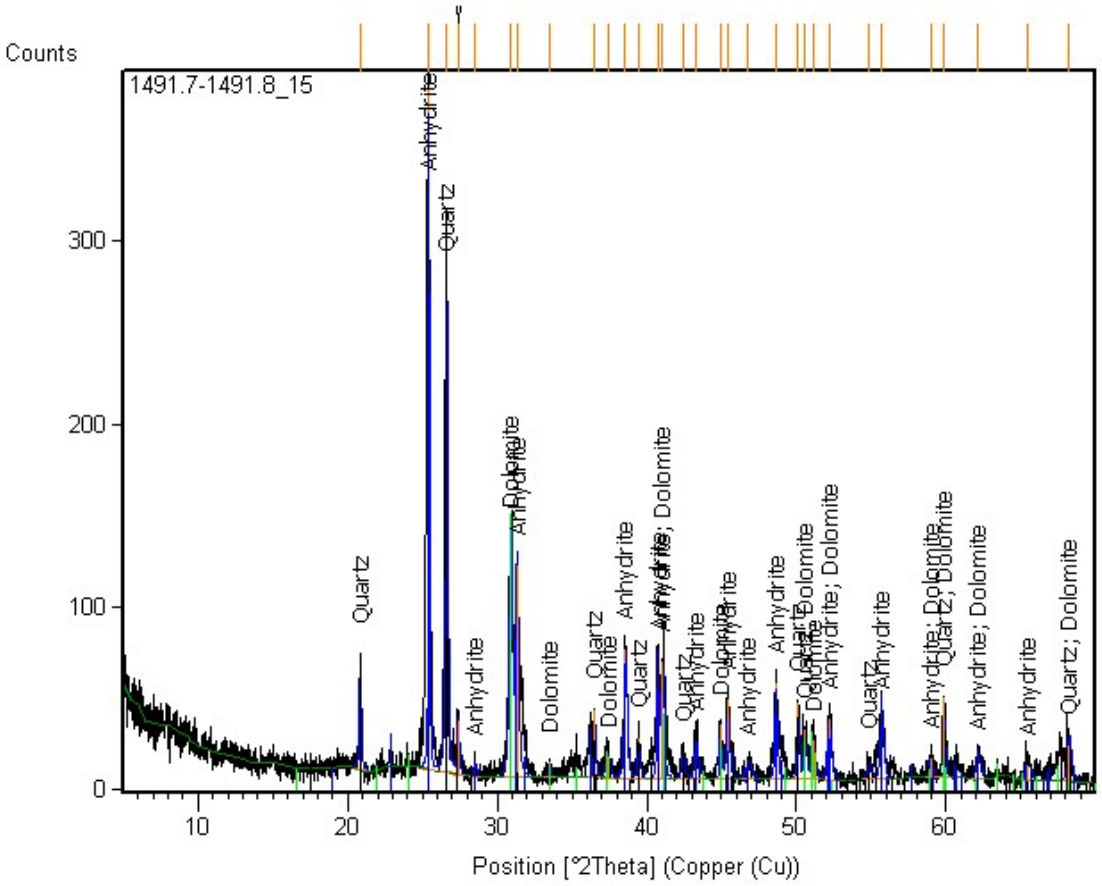
Counts
1491.7-1491.8_15
300
200
100
0
10
20
30
40
50
60
Position [°2Theta] (Copper (Cu))
Quartz
Anhydrite
Dolomite
Anhydrite; Dolomite
Quartz; Dolomite
Anhydrite; Dolomite

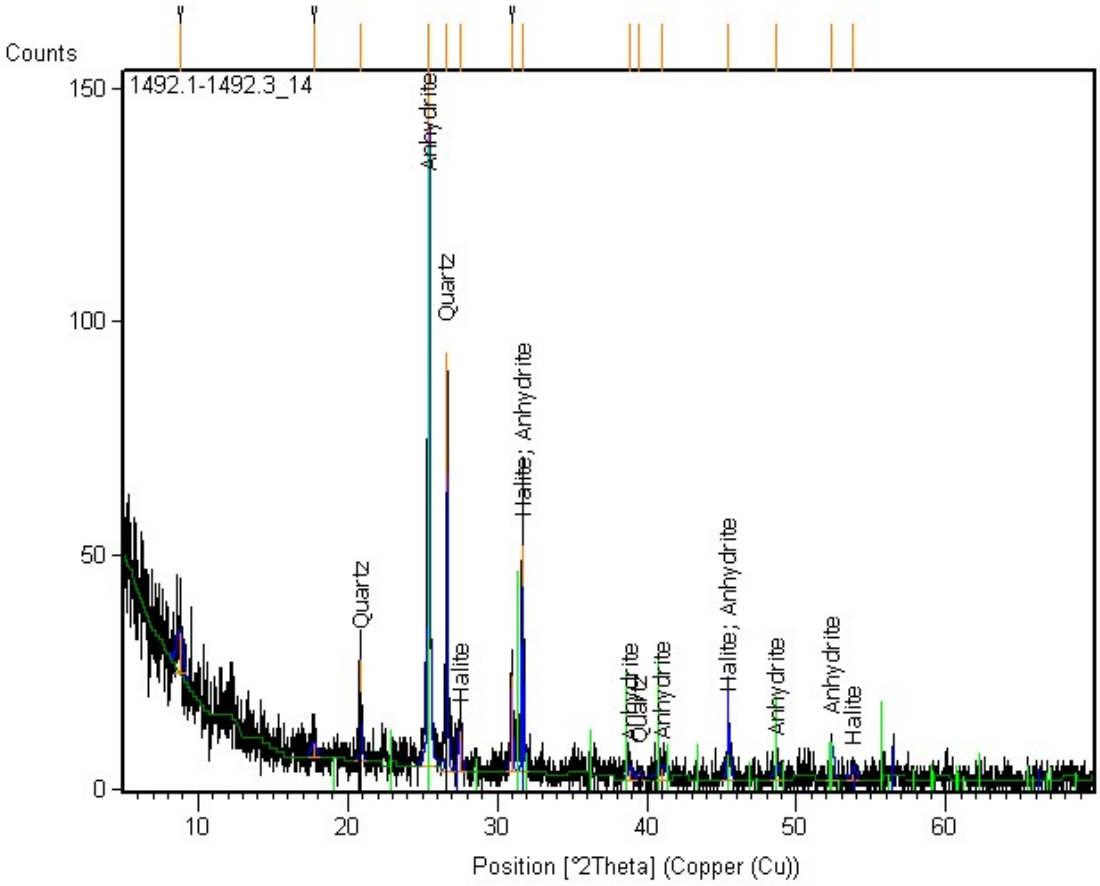
Counts
1492.1-1492.3_14
150
100
50
0
10
20
30
40
50
60
Position [°2Theta] (Copper (Cu))
Anhydrite
Quartz
Halite; Anhydrite
Quartz
Halite
Anhydrite
Halite; Anhydrite
Anhydrite
Anhydrite
Halite

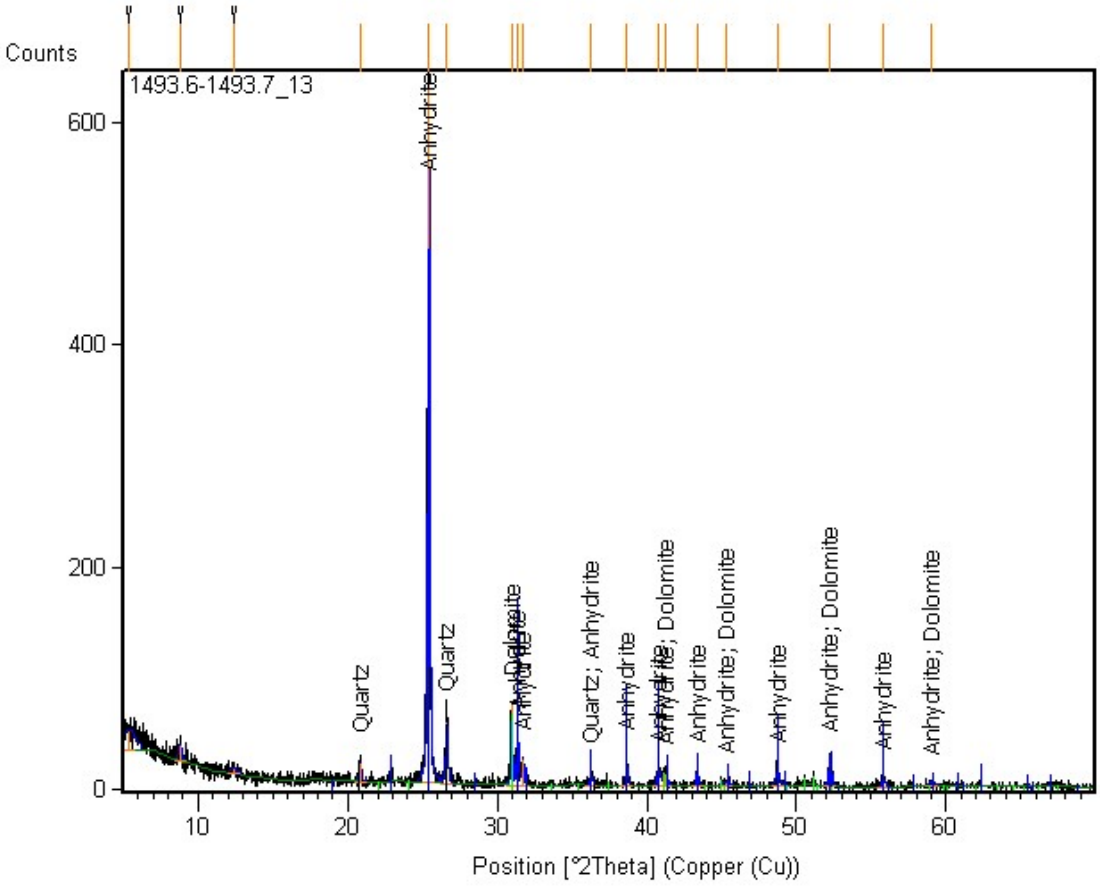
Counts
1493.6-1493.7_13
600
400
200
0
10
20
30
40
50
60
Position [°2Theta] (Copper (Cu))
Anhydrite
Quartz
Quartz
Quartz; Anhydrite
Anhydrite
Anhydrite; Dolomite
Anhydrite
Anhydrite; Dolomite
Anhydrite
Anhydrite; Dolomite
Anhydrite
Anhydrite; Dolomite

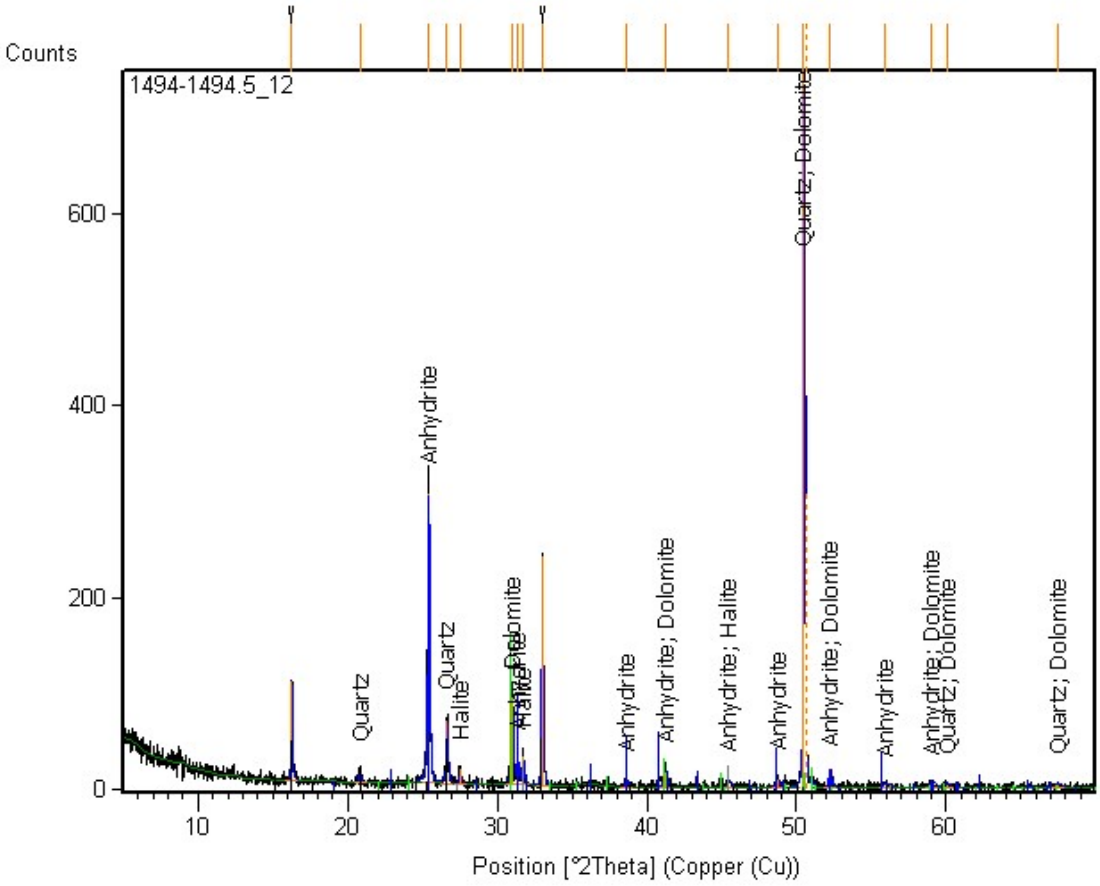
Counts
1494-1494.5_12
600
400
200
0
10
20
30
40
50
60
Position [°2Theta] (Copper (Cu))
Quartz
Anhydrite
Quartz
Halite
Dolomite
Anhydrite
Anhydrite; Dolomite
Anhydrite; Halite
Anhydrite
Quartz; Dolomite
Anhydrite; Dolomite
Anhydrite
Anhydrite; Dolomite
Quartz; Dolomite
Quartz; Dolomite

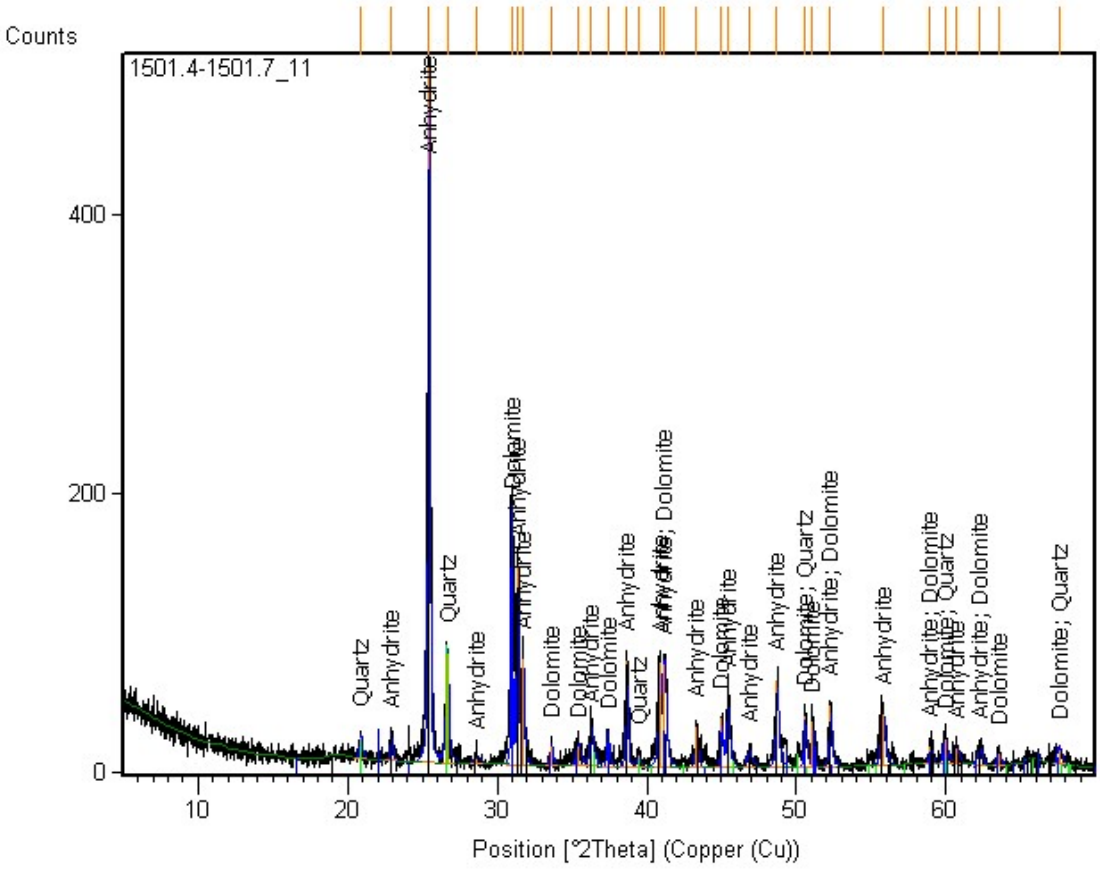
Counts
1501.4-1501.7_11
400
200
0
10
20
30
40
50
60
Position [°2Theta] (Copper (Cu))
Quartz
Anhydrite
Dolomite
Anhydrite; Dolomite
Anhydrite; Quartz
Dolomite; Quartz
Anhydrite; Dolomite
Dolomite; Quartz

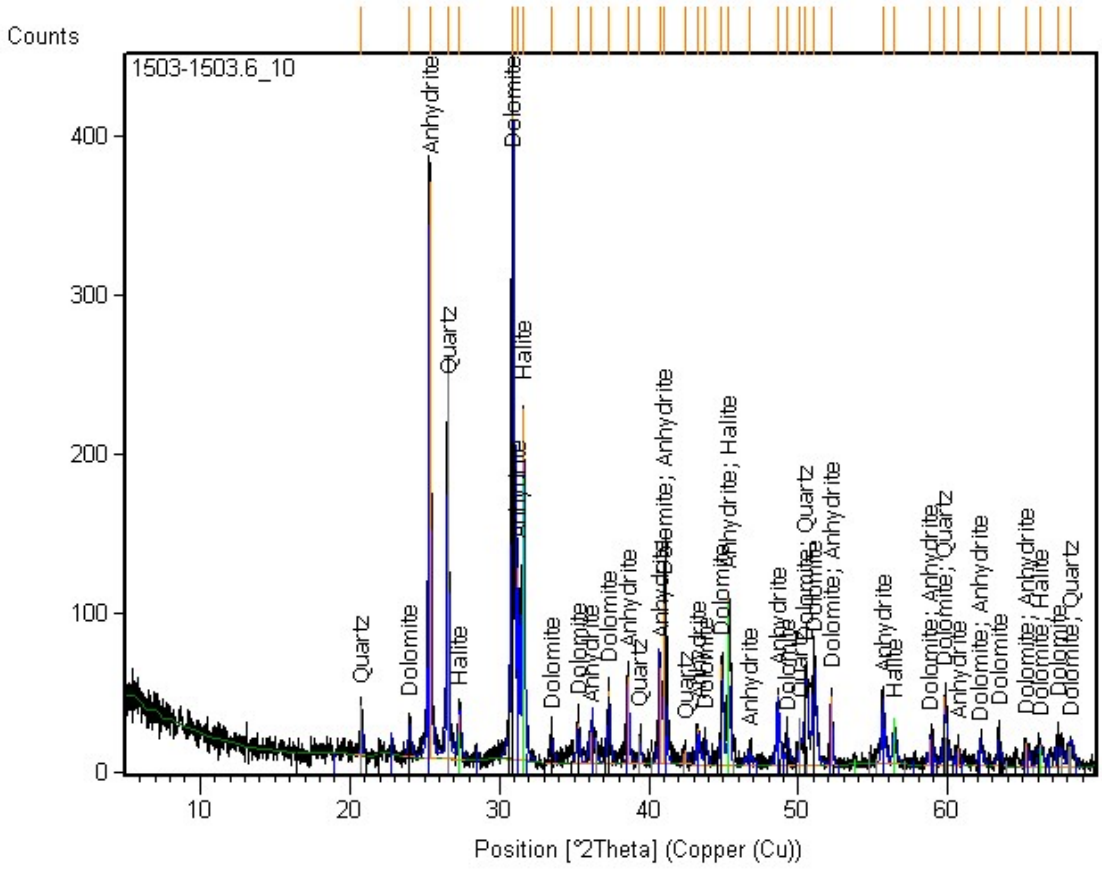
Counts
1503-1503.6_10
400
300
200
100
0
10
20
30
40
50
60
Position [°2Theta] (Copper (Cu))
Anhydrite
Dolomite
Quartz
Halite
Dolomite; Anhydrite
Anhydrite; Halite
Dolomite; Quartz
Dolomite; Anhydrite; Quartz

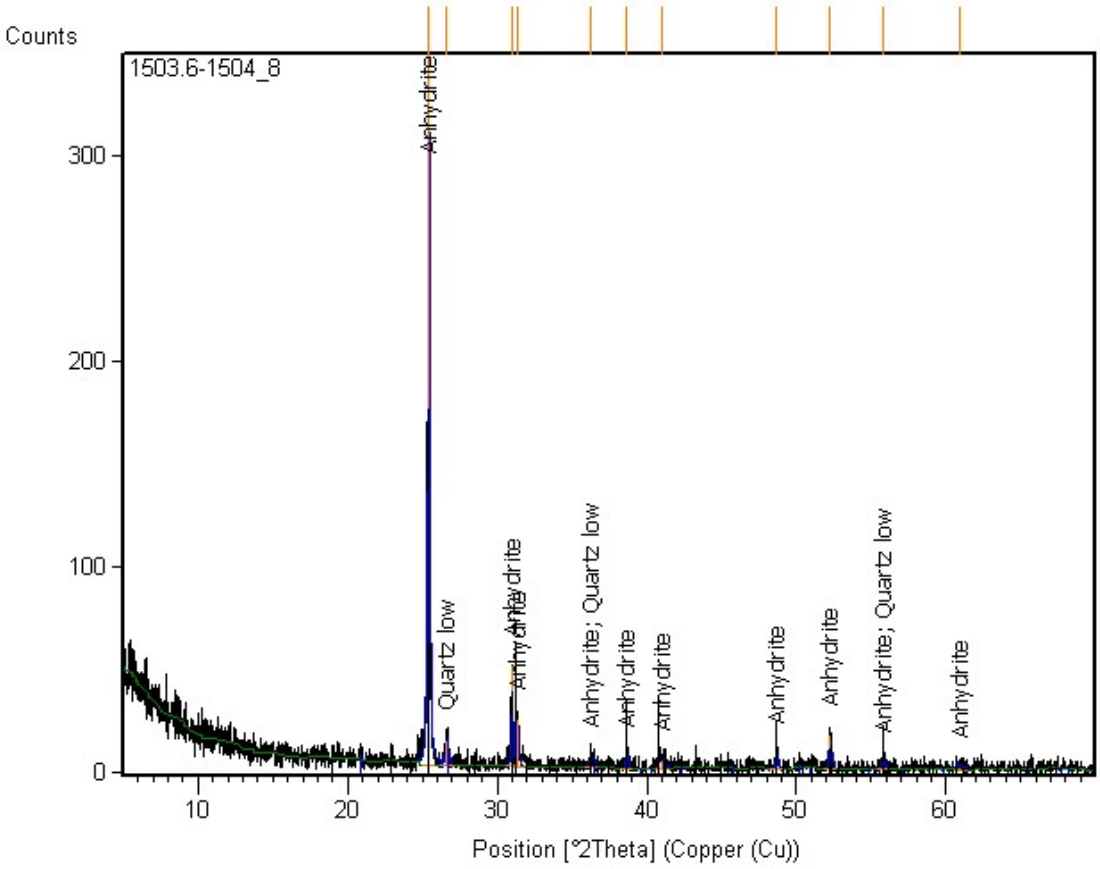
Counts
1503.6-1504_8
300
200
100
0
10
20
30
40
50
60
Position [°2Theta] (Copper (Cu))
Anhydrite
Quartz low
Anhydrite
Anhydrite; Quartz low
Anhydrite
Anhydrite
Anhydrite
Anhydrite
Anhydrite; Quartz low
Anhydrite

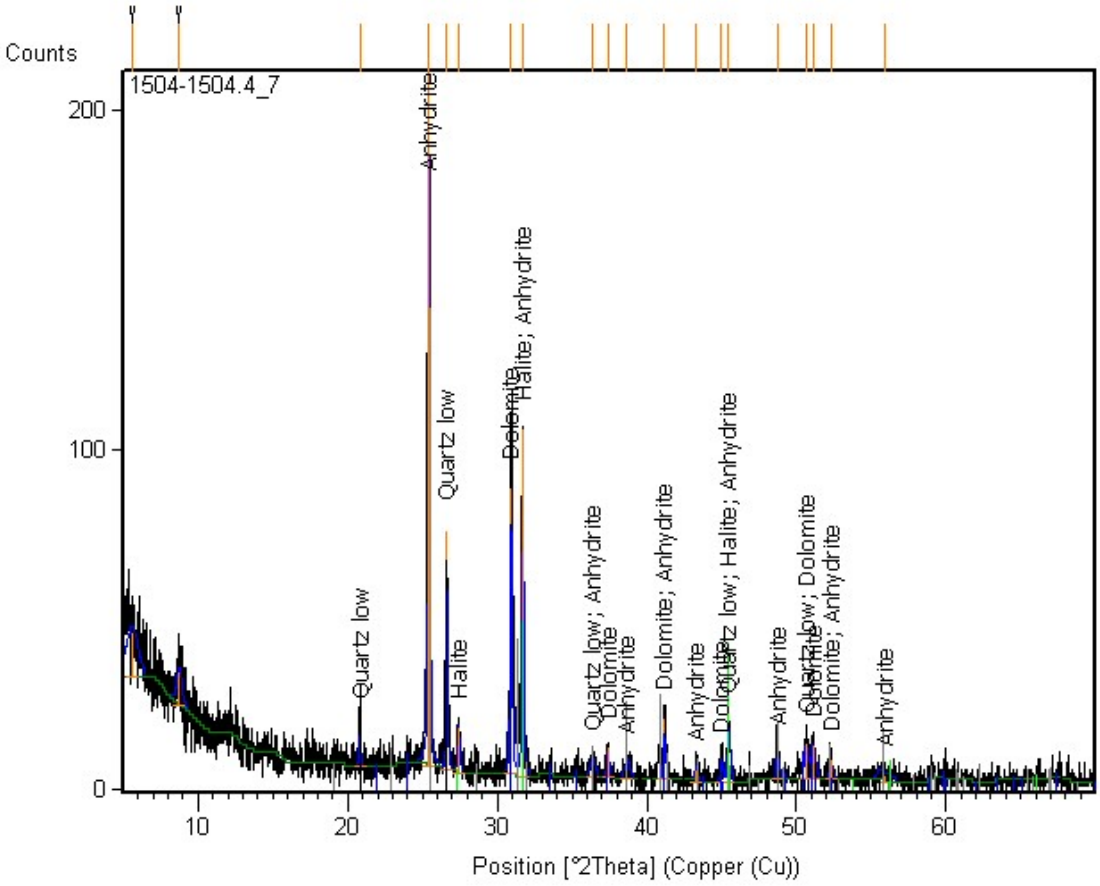
Counts
1504-1504.4_7
200
100
0
10
20
30
40
50
60
Position [°2Theta] (Copper (Cu))
Anhydrite
Quartz low
Halite; Anhydrite
Dolomite
Quartz low; Anhydrite
Dolomite; Anhydrite
Halite
Quartz low; Halite; Anhydrite
Quartz low; Dolomite

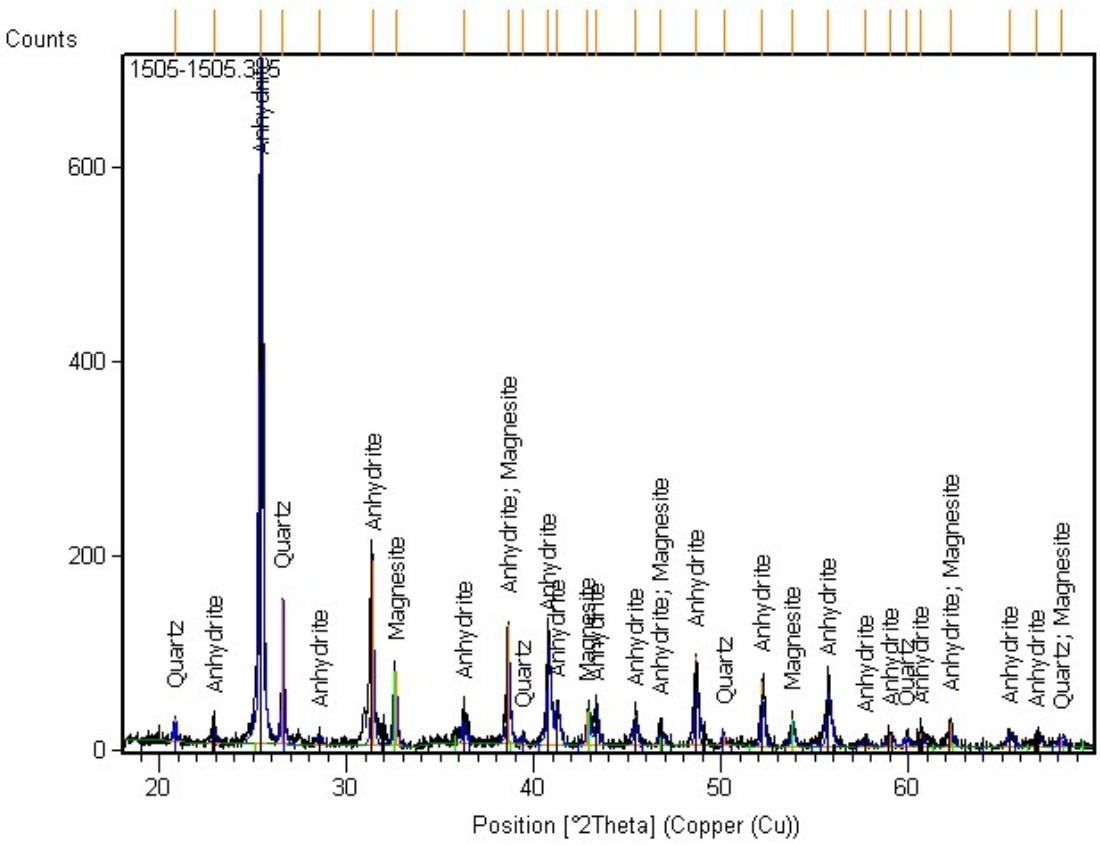
Counts
1505-1505.35
600
400
200
0
20
30
40
50
60
Position [°2Theta] (Copper (Cu))
Quartz
Anhydrite
Quartz
Anhydrite
Anhydrite
Magnesite
Anhydrite
Anhydrite; Magnesite
Quartz
Anhydrite
Anhydrite
Anhydrite; Magnesite
Anhydrite
Quartz
Anhydrite
Magnesite
Anhydrite
Anhydrite
Quartz
Anhydrite
Anhydrite; Magnesite
Anhydrite
Anhydrite
Quartz; Magnesite

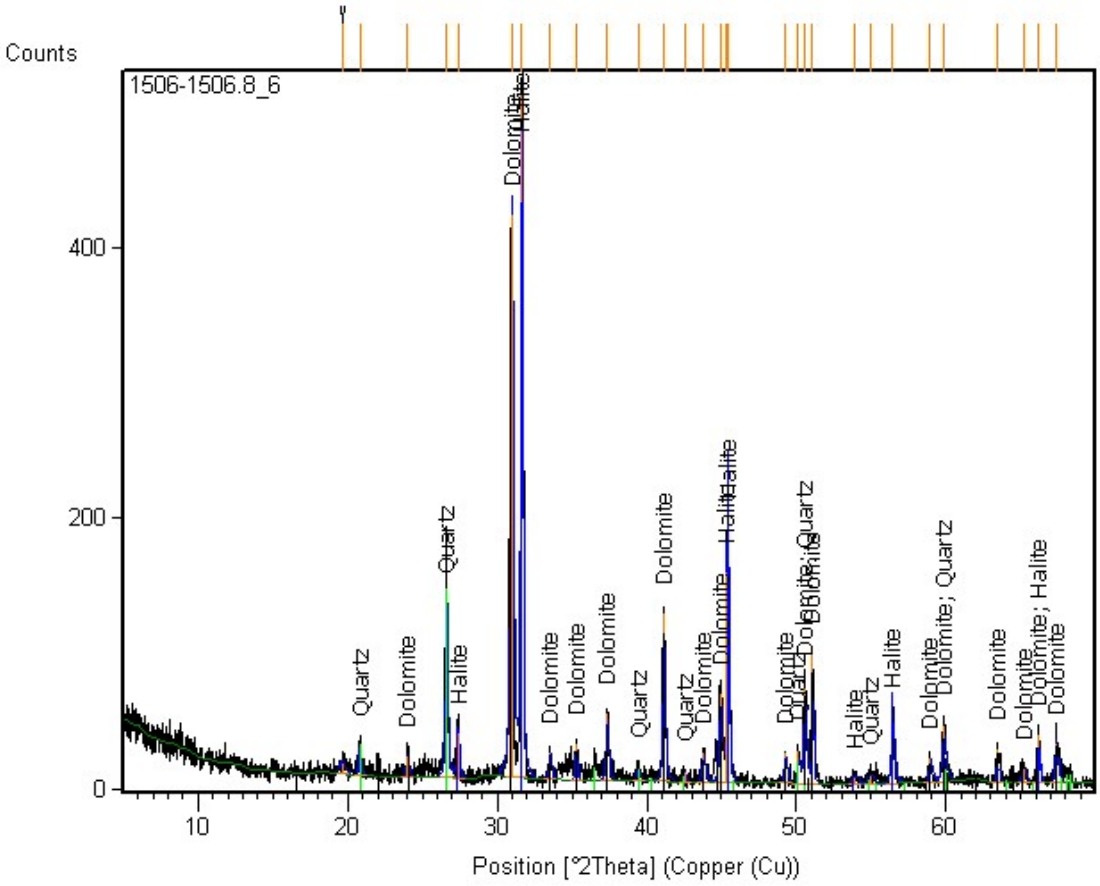
Counts
1506-1506.8_6
400
200
0
10
20
30
40
50
60
Position [°2Theta] (Copper (Cu))
Quartz
Dolomite
Halite
Dolomite; Quartz
Dolomite; Halite

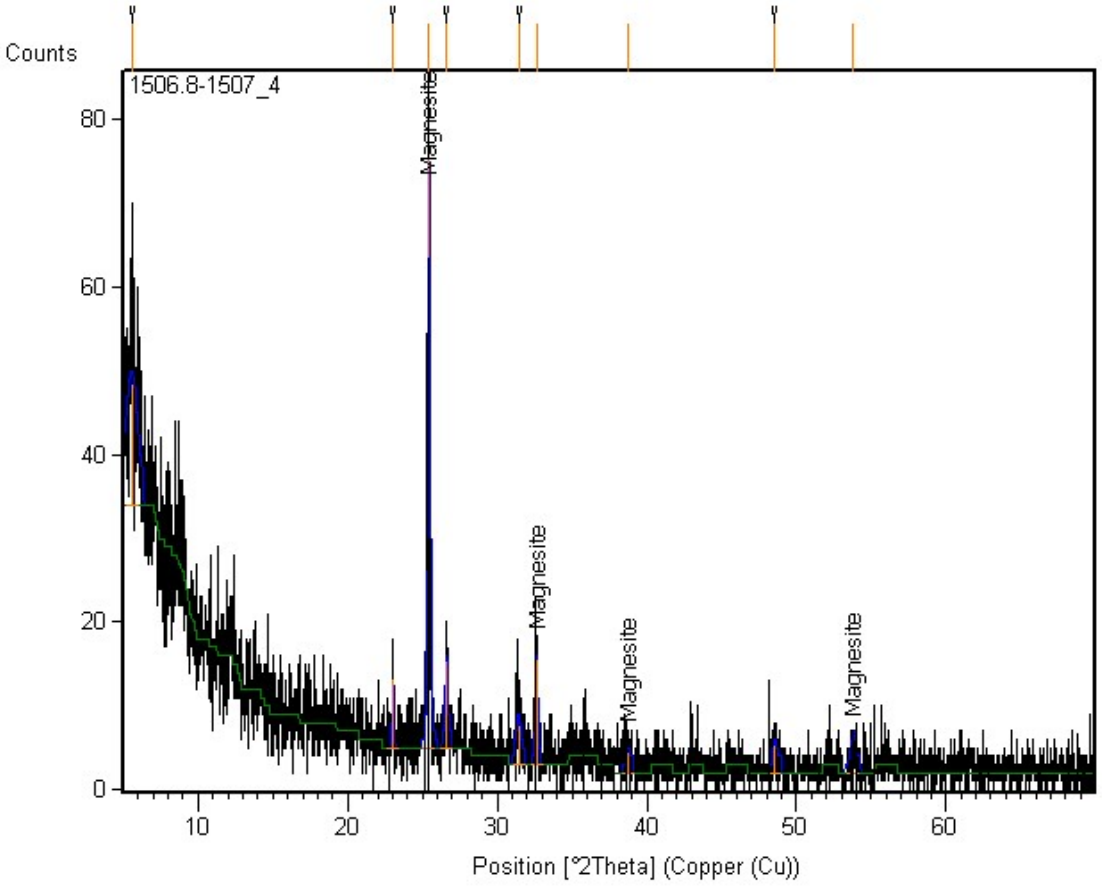
Counts
1506.8-1507_4
Magnesite
Magnesite
Magnesite
Magnesite
80
60
40
20
0
10
20
30
40
50
60
Position [°2Theta] (Copper (Cu))

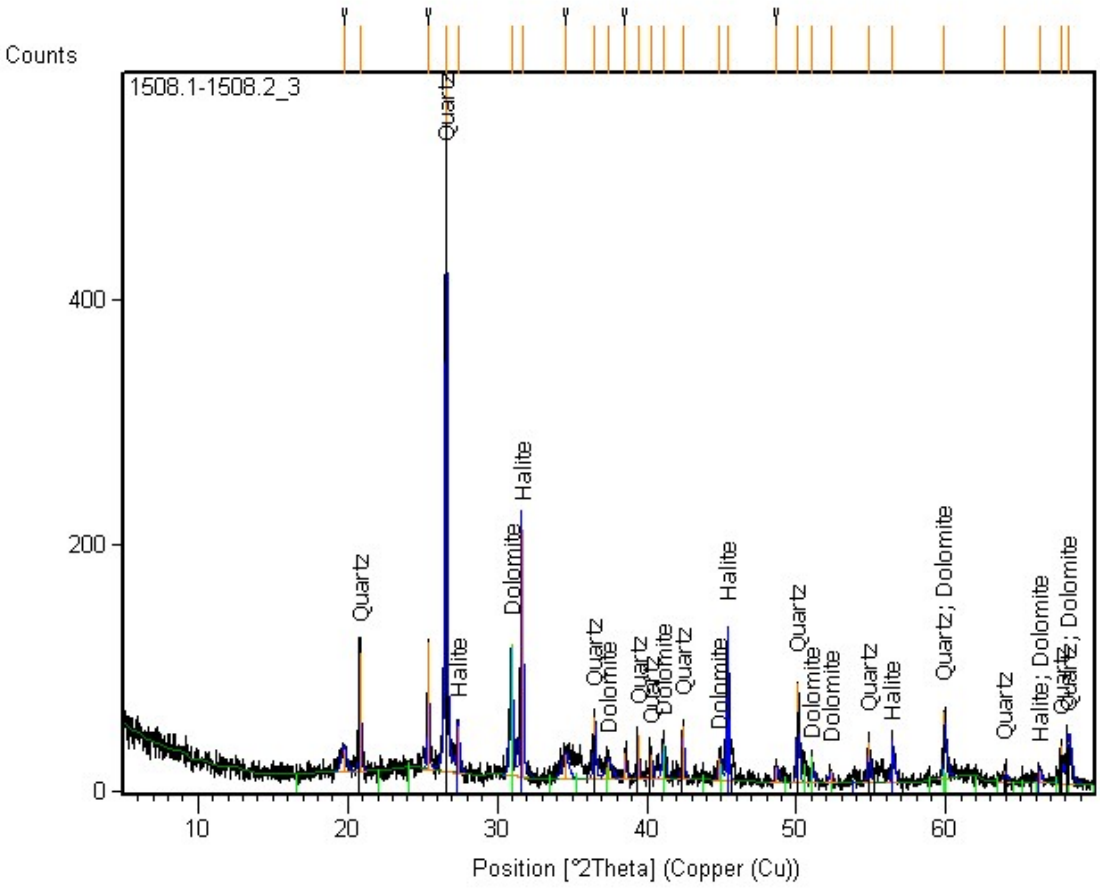
Counts
1508.1-1508.2_3
400
200
0
10
20
30
40
50
60
Position [°2Theta] (Copper (Cu))
Quartz
Halite
Dolomite
Quartz; Dolomite
Halite; Dolomite

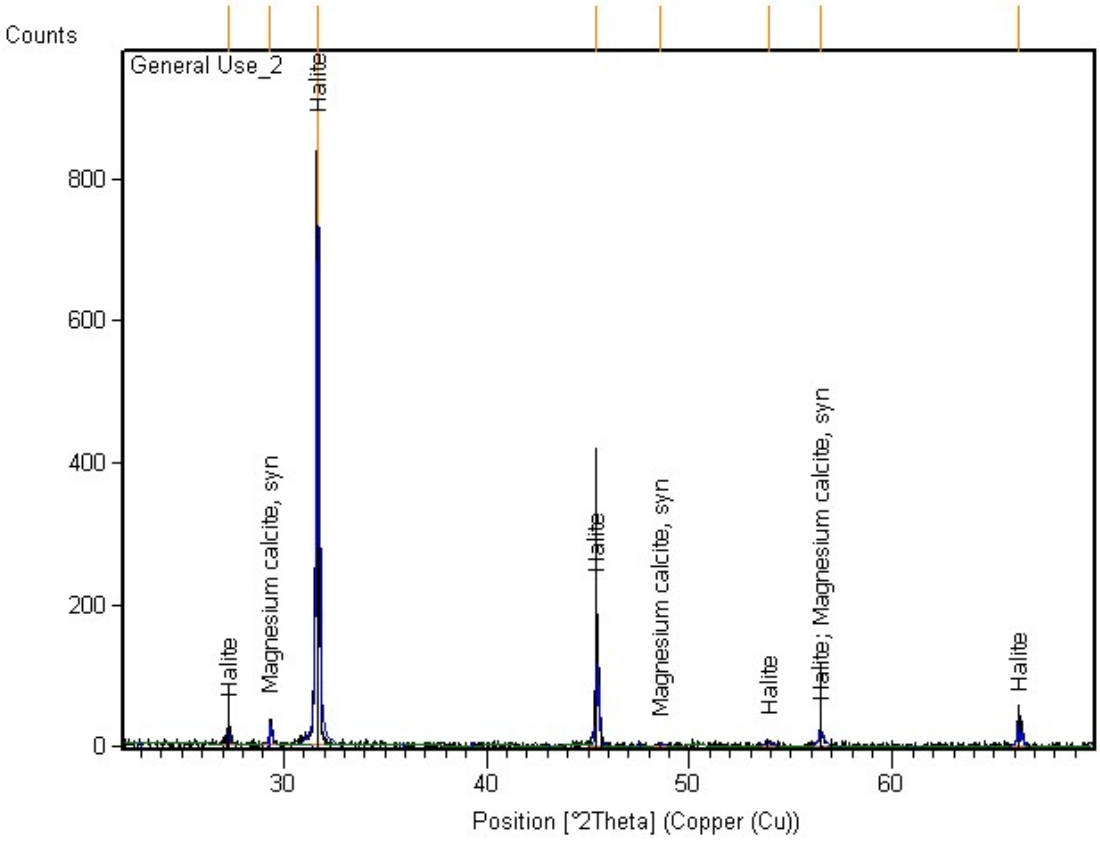
Counts
General Use_2
800
600
400
200
0
30
40
50
60
Position [°2Theta] (Copper (Cu))
Halite
Magnesium calcite, syn
Halite
Halite
Magnesium calcite, syn
Halite
Halite; Magnesium calcite, syn
Halite

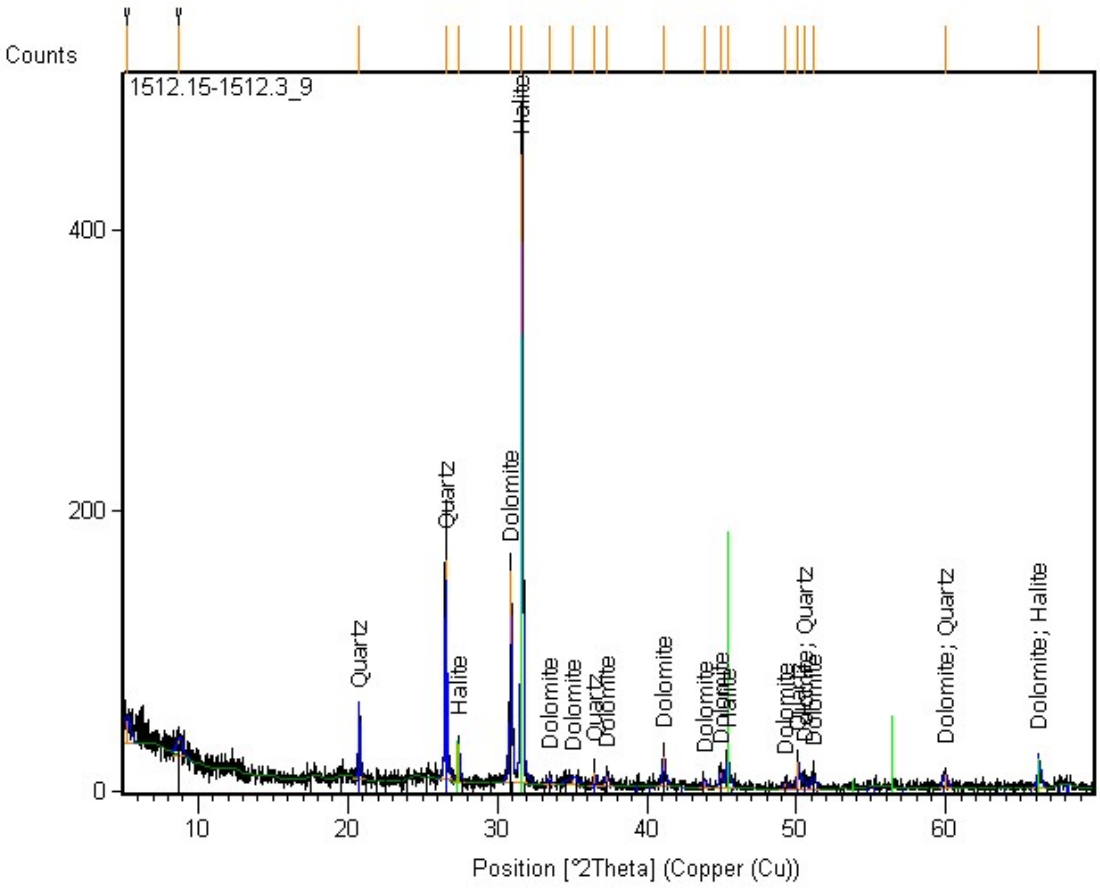
Counts
1512.15-1512.3_9
400
200
0
10
20
30
40
50
60
Position [°2Theta] (Copper (Cu))
Halite
Quartz
Dolomite
Quartz
Halite
Dolomite
Dolomite
Quartz
Dolomite
Dolomite
Dolomite
Dolomite; Quartz
Dolomite; Quartz
Dolomite; Halite

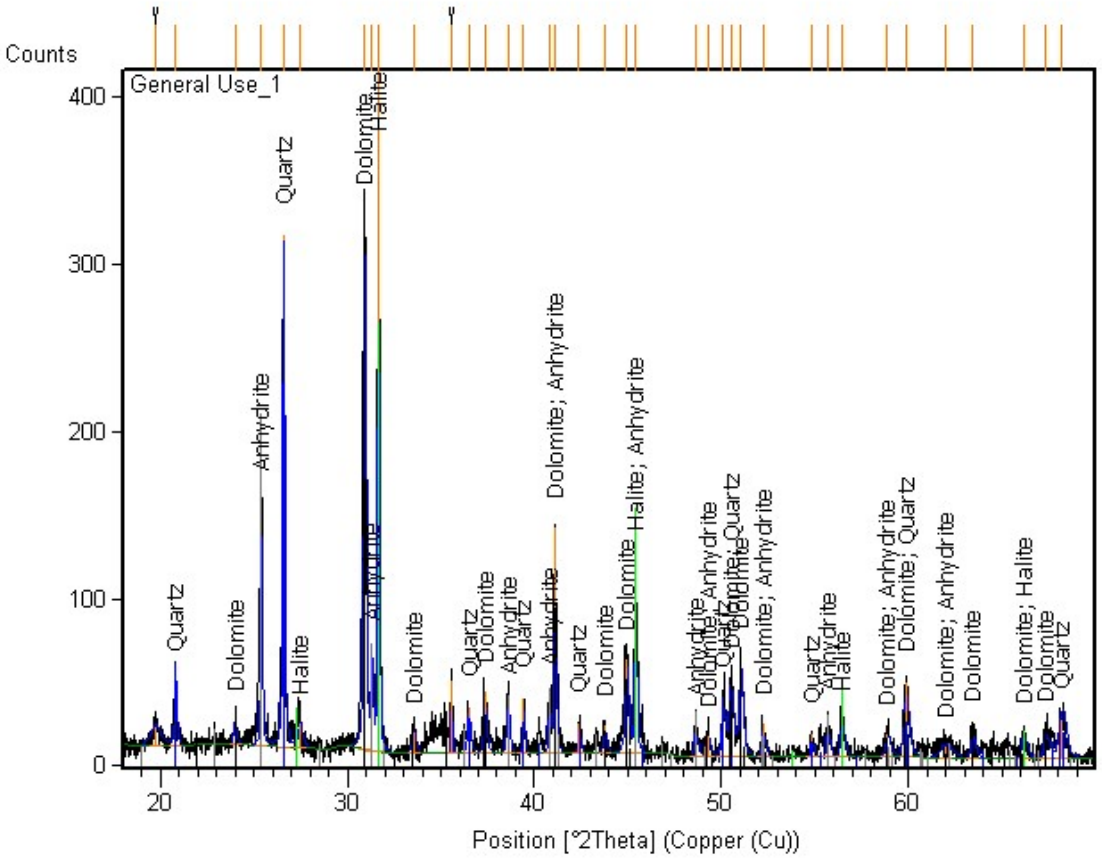
Counts
General Use_1
400
300
200
100
0
20
30
40
50
60
Position [°2Theta] (Copper (Cu))
Quartz
Dolomite
Anhydrite
Halite
Dolomite; Anhydrite
Halite; Anhydrite

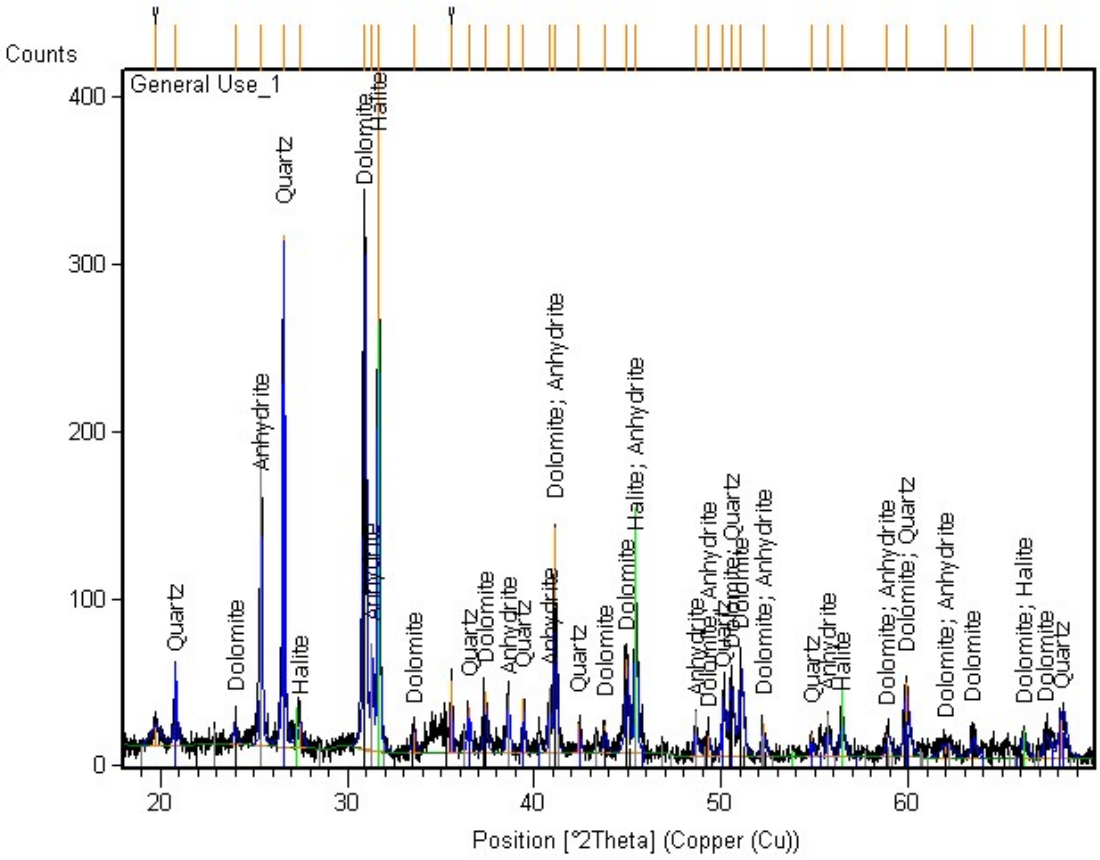
Counts
General Use_1
400
300
200
100
0
20
30
40
50
60
Position [°2Theta] (Copper (Cu))
Quartz
Dolomite
Anhydrite
Halite
Dolomite; Anhydrite
Halite; Anhydrite
Dolomite; Quartz
Dolomite; Halite

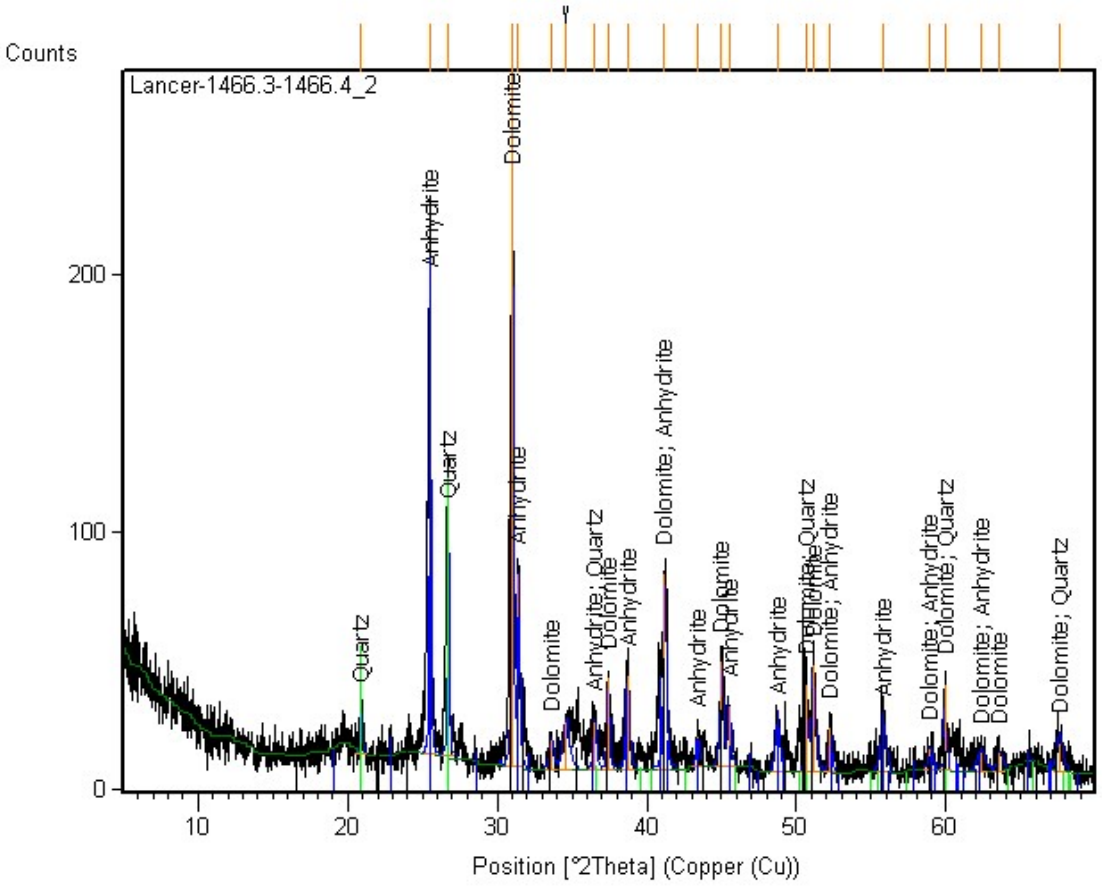
Counts
Lancer-1466.3-1466.4_2
200
100
0
10
20
30
40
50
60
Position [°2Theta] (Copper (Cu))
Quartz
Anhydrite
Dolomite
Anhydrite; Quartz
Dolomite; Anhydrite
Dolomite; Quartz

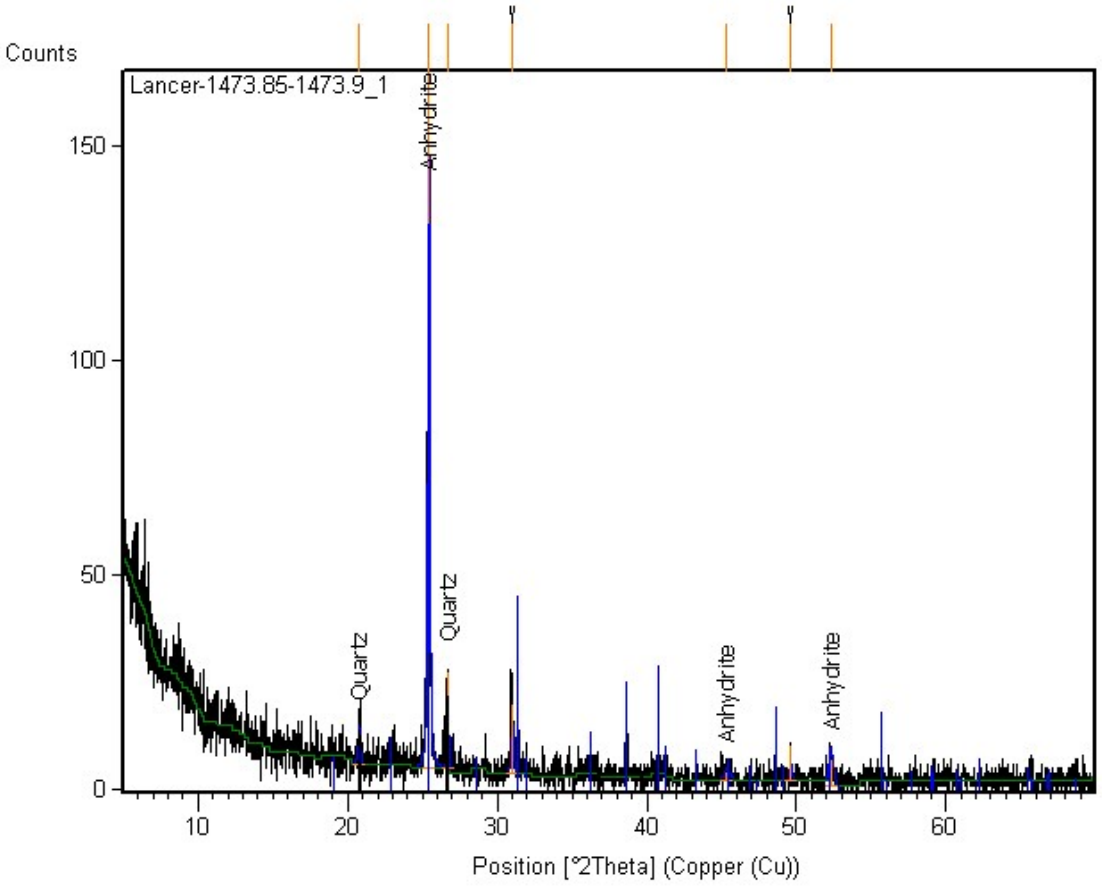
Counts
Lancer-1473.85-1473.9_1
Anhydrite
Quartz
Quartz
Anhydrite
Anhydrite
150
100
50
0
10
20
30
40
50
60
Position [°2Theta] (Copper (Cu))

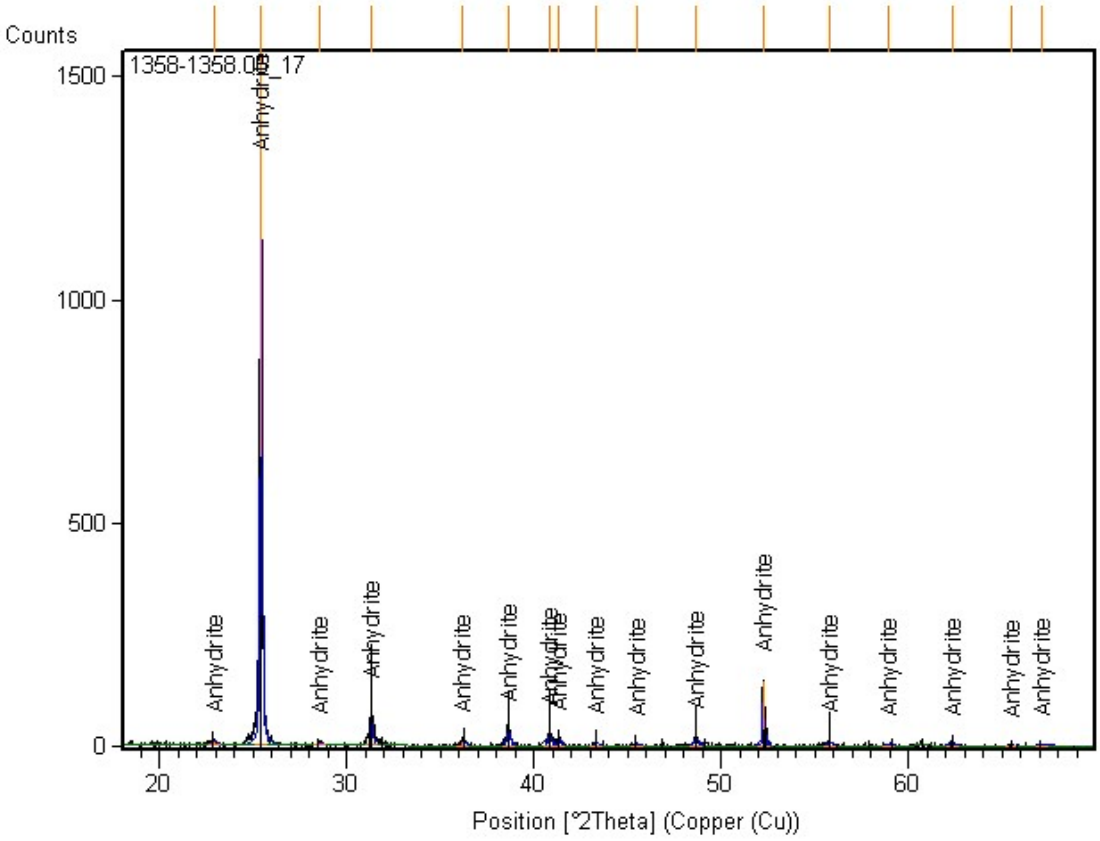
Counts
1358-1358.0[illegible]_17
1500
1000
500
0
Anhydrite
20
30
40
50
60
Position [°2Theta] (Copper (Cu))

2.2 SUPPLEMENTARY DATA FOR CHAPTER 3

2.2.1 Photomicrographs of thin sections selected to show primary versus non-primary features of halite crystals used to identify samples for fluid-inclusion analysis.

A) Photomicrograph of fluid inclusions arranged in a chevron formation. The preservation of chevron structures shows that the halite has not recrystallized, and that the brines analyzed were trapped as primary fluid inclusions at the time of crystal growth. This photo is of a thin section I prepared from a core sample from the Empress 1A well, depth ~1502 m.

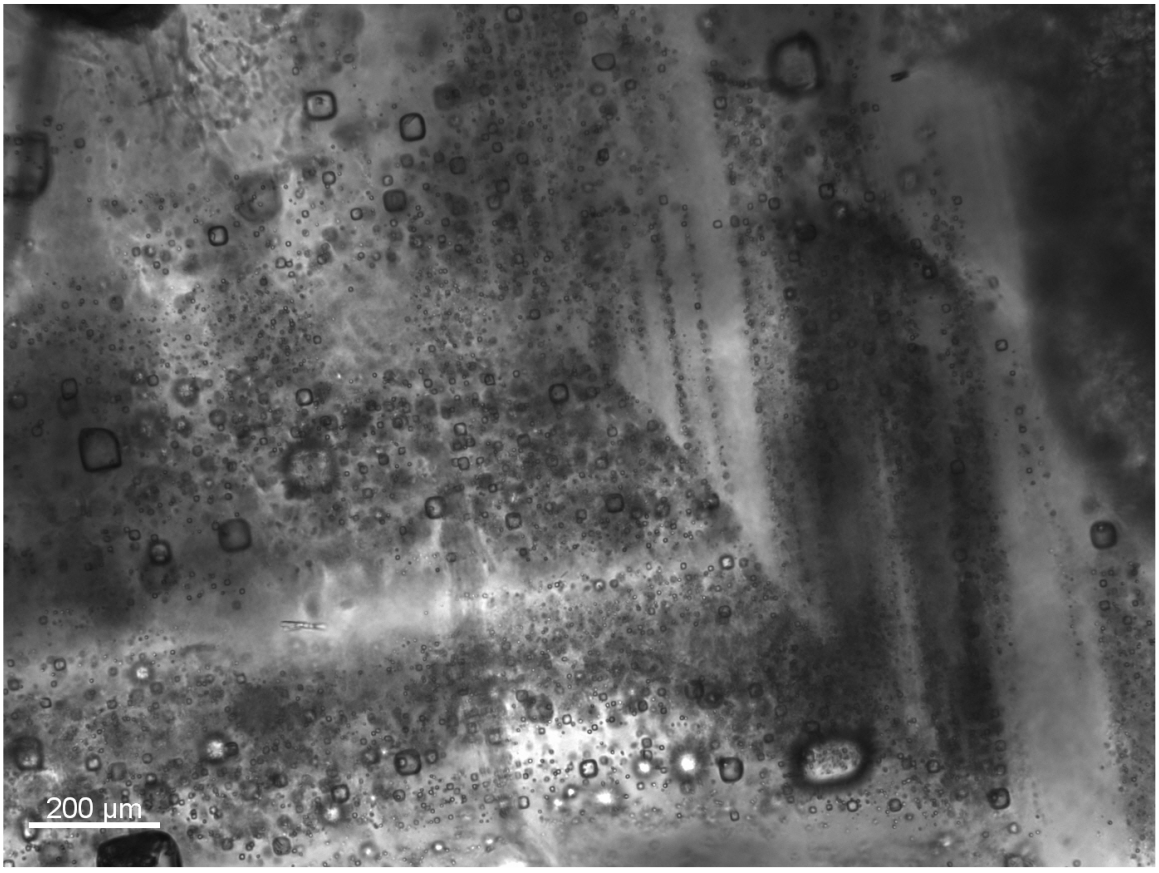

B) Photograph of a thin section showing draping mud that follows the halite crystal structure. Draping mud layers are indicative of subaqueous deposition without dissolution, and are associated with primary halite. This photo is of a thin section I prepared from a core sample from the Empress 1A well, depth ~1502 m.

C) Photograph of a thin section showing mud layers that truncate the underlying halite crystal. Truncating mud layers are indicative of an influx of diluted brine and subaqueous deposition, and are associated with clear voids filled with recrystallized halite. These areas of recrystallized halite appear vertically integrated with halite containing chevron fluid-inclusion structures. I prepared this thin section from a sample from the Empress 1A well, depth 1500 m.

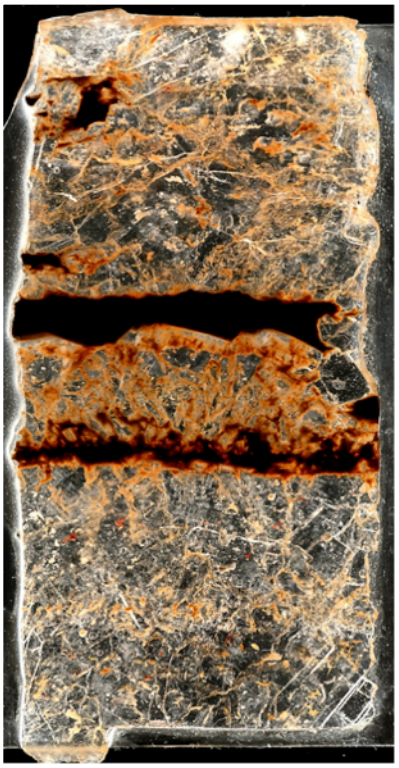

D) Photograph of a thin section showing halite that grows displacively in mud. The halite is precipitated from halite-saturated ground water and does not contain primary structures. I prepared this thin section from a sample from the Empress 1A well, depth ~1495 m.

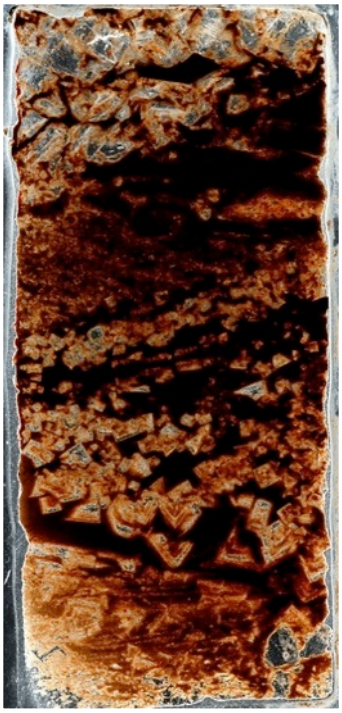

E) Photograph of a thin section showing the textures indicative of an efflorescent crust. Efflorescent crusts form in the cracks left by the fracturing of salt crusts due to the pressure of displacive halite growing in the subsurface. These are indicative of a salt-pan environment and are not associated with primary fluid-inclusion textures. I prepared this thin section from a sample from the Empress 1A well, depth ~1477 m.

2.2.12 Results from Fluid-Inclusion Analysis as determined by Cryo-SEM-EDS

Depth (m)	Na^+	K^+	Ca^{2+}	Mg^{2+}	Cl^-
1478 (E)	530	40	350	3550	8370
1478 (E)	410	40	420	3720	8730
1478 (E)	650	30	370	3590	8400
1478 (E)	720	20	450	3210	8060
1478 (E)	660	20	350	3680	8770
*1482 (E)	320	10	600	4640	9900
*1482 (E)	370	20	520	4510	10450
1482 (E)	220	20	520	4030	9340
*1482 (E)	260	20	600	4540	10560
1482 (E)	310	20	530	3970	9330
1482 (E)	260	10	550	4010	9390
1492 (E)	630	110	370	3650	8780
1492 (E)	630	100	400	3450	8490
1492 (E)	520	120	420	3570	8620
1492 (E)	440	110	380	3090	7490
1497 (E)	620	20	420	3650	8780
1497(E)	590	30	450	3580	8680
1497 (E)	710	40	380	3390	8290
1497 (E)	490	40	520	3210	7990
1497 (E)	650	40	410	3710	8930
1497 (E)	530	20	360	3450	8170
1501.8 (E)	630	20	280	3500	8630

1501.8 (E)	540	20	280	3750	8620
1501.8 (E)	570	10	280	3840	8820
1501.8 (E)	580	10	250	3870	8830
1501.8 (E)	490	10	260	3690	8400
1501.8 (E)	580	10	240	3900	8870
1502.2 (E)	530	20	360	3700	8670
1502.2 (E)	430	20	280	3600	8210
1502.2 (E)	530	10	310	3810	8780
1502.2 (E)	470	10	350	3720	8620
1502.2 (E)	500	20	300	3730	8580
1502.2 (E)	540	30	340	3780	8810
1502.2 (E)	540	10	320	3850	8890
1466.25 (L)	520	20	550	3910	9460
1466.25 (L)	440	10	520	3670	8830
1466.25 (L)	560	10	450	3780	9030
1466.25 (L)	470	10	520	4030	9580
*1466.25 (L)	360	20	500	4230	9840
1443.6(L)	440	10	440	4250	9940
1443.6(L)	410	10	380	4420	9480
1443.6(L)	390	20	420	4490	10520

Note: Concentrations in mmol/kg H_2O. Samples from Empress 1A designated by (E) and from Lancer 1 by (L).

*Depths correspond to fluid-inclusions that fall in the potash zone.

2.3 SUPPLEMENTARY DATA FOR CHAPTER 4

2.3.1 $\delta^{34}S_{sulfate}$ Results

Sample Depth (m)	δ34S (‰)
Empress 1A	
1479	15.2
1484.5	15.3
1486	15.4
1488.1	15
1488.4	15.2
1492	15.4
1494	15.1
1494.3	15.2
1496	15.5
1497	15.9
1498	15.1
1500.5	15.6
1501.4	15.1
1501.9	15.5
1502.1	15.3
1502.5	15.8
1504	14.9
1505	15.3
1506	15.4
1506.8	15.1
1507.8	15.2
1510	15
1513.3	15.6
1517	15.3

1523.2	14.8
Lancer 1	
1465.5	15.1
1471.5	15.5

2.3.2 Bromine Results

Sample Depth (m)	Br (ppm)
Empress 1A	
1479	73
1484.5	91
1486	87
1492	93
1496	103
1500	106
1501	119
1502	122
Lancer 1	
1465.5	107
1471.5	111

REFERENCES

Apak, S.N., Ghori, K.A.R., Carlsen, G.M., Stevens, M.K., 2002. Basin development with implications for petroleum trap styles of the Neoproterozoic Officer Basin, Western Australia, in: Keep, M. and Moss, S.J. (Eds.), The sedimentary basins of Western Australia. Petroleum Exploration Society of Australia Symposium, Perth, W.A., 2003, Proceedings, 914-926.

Apak, S.N., Moors, H.T., 2000. A sequence stratigraphic depositional model of Neoproterozoic strata, Yowalga area, Officer Basin, Western Australia. APPEA Journal, v. 40, p. 15-25.

Azmy, K., Veizer, J., Misi, A., Flávio de Oliveira, T., Sanches, A.L., Dardenne, M.A., 2001. Dolomitization and isotope stratigraphy of the Vazante Formation, São Francisco Basin, Brazil. Precambrian Research 112, 303-329.

Ayora, C., García-Veigas, J., Pueyo, J.J., 1994. X-ray Microanalysis of frozen fluid inclusions and its application to geochemical modeling of evaporite basins. Geochimica et Cosmochimica Acta 58, 43-55.

Bekker, A., Holland, H.D., Wang, P.L., Rumble, D., Stein, H.J., Hannah, J.L., Coetzee, L.L., Beukes, N.J., 2004. Dating the rise of atmospheric oxygen. Nature 427, 117-120.

Bottrell, S.H., Newton, R.J., 2006. Reconstruction of changes in global sulfur cycling from marine sulfate isotopes. Earth-Sciences Reviews 75, 59-83.

Braitsch, O., 1971. Salt deposits. Their origin and composition. Springer-Verlag. Berlin-Heilderberg-New York.

Brennan, S.T., Lowenstein, T.K., Horita, J., 2004. Seawater chemistry and the advent of biocalcification. Geology, v. 32, p. 473-476.

Burdett, J.W., Grotzinger, J.P., Arthur, M.A., 1990. Did major changes in stable-isotope composition of Proterozoic seawater occur? Geology 296, 227-230.

Camacho, A., Hensen, B.J., Armstrong, R., 2002. Isotopic test of a thermally driven intraplate orogenic model, Australia. Geology 30, 887-890.

Canfield, D.E., 1998. A new model for Proterozoic ocean chemistry. Nature 396, 450-453.

Canfield, D.E., 2004. The evolution of the Earth Surface Sulfur Reservoir. American Journal of Science, v. 304, p. 839-861.

Canfield, D.E, 2005. The early history of atmospheric oxygen: Homage to Robert M. Garrels. Annual Review of Earth and Planetary Sciences 33, 1-36.

Canfield D. E., Farquhar J., 2009. Animal evolution, bioturbation, and the sulfate concentration of the oceans. Proceedings of the National Academy of Science 106, 8123-8127.

Canfield D. E., Farquhar J., and Zerkle A. L. (2010) High isotope fractionations during sulfate reduction in a low-sulfate euxinic ocean analog. Geology 38, 415–418.

Canfield, D.E., Habicht, K. S., Thamdrup, B. 2000. The Archean Sulfur Cycle and the Early History of Atmospheric Oxygen. Science 288, 658-661.

Canfield, D.E., Poulton, S.W., Narbonne, G.M., 2007. Late-Neoproterozoic deep-ocean oxygenation and the rise of animal life. Science, v. 315, p. 92-94.

Carlsen, G.M., Apak, S.N., Ghori, K.A.R., Grey, K., Stevens, M.K., 1999. Petroleum potential of the Neoproterozoic western Officer Basin, Western Australia, based on a source-rock model from Empress 1A; The APPEA Journal 39, 322-342.

Claypool, G.E., Holser, W., Kaplan, I., Sakai, H., Zak, I., 1980. The ages curves of sulfur and oxygen isotopes in marine sulfate and their mutual interpretation. Chemical Geology, v. 28, p. 199-260.

Dickson, J.A.D., 2002. Fossil echinoderms as monitor of the Mg/Ca ratio of Phanerozoic oceans. Science, v. 298, p. 1222-1224.

Dyson, I.A., Marshall, T.R., 2005. The influence of salt tectonics on Neoproterozoic to Early Palaeozoic sedimentation, Amadeus Basin. Central Australian Basin Symposium.

Eyles, C.H., Eyles, N., Grey, K., 2007. Paleoclimate implications from deep drilling Neoproterozoic strata in the Officer Basin and Adelaide Rift Complex of Australia; a marine record of wet-based glaciers. Palaeogeography, Palaeoclimatology, Palaeoecology 248, 291-312.

Fanning, C.M., Ludwig, K.R., Forbes, B.G., Preiss, W.V., 1986. Single and multiple grain U-Pb zircon analyses for the Early Adelaidean Rook Tuff, Willouran Ranges, South Australia. Geological Society of Australia Abstracts 15, 71.

Farquhar, J., Wu, N., Canfield, D.E., Oduro, H., 2010. Connections between Sulfur Cycle Evolution, Sulfur Isotopes, Sediments, and Base Metal Sulfide Deposits. Economic Geology 105, 509-533.

Fike, D.A., Grotzinger, J.P., Pratt, L.M., Summons, R.E., 2006. Oxidation of the Ediacaran ocean: Nature, v. 444, p. 744-747.

Frei, R., Gaucher, C., Poulton, S.W., Canfield, D.E., 2009. Fluctuations in Precambrian atmospheric oxygenation recorded by chromium isotopes. Nature, v. 461, p. 250-253.

García-Veigas, J., Rosell, L., Zak, I., Playà, E., Ayora, C., Starinsky, A., 2009. Evidence of potash salt formation in the Pliocene Sedom Lagoon (Dead Sea Rift, Israel). Chemical Geology, v. 265, p. 499-511.

Goldstein, R.H., Reynolds, T.J., 1994. Systematic of fluid inclusions in diagenetic minerals. SEPM Short Course 31, Tulsa.

Gorjan, P., Veevers, J.J., Walter, M.R., 2000. Neoproterozoic sulfur-isotope variation in Australia and global implications. Precambrian Research 100, 151-179.

Grey, K., 2005. Ediacaran palynology of Australia. Memoir of the Association Australasian Paleontologists 31.

Grotzinger, J.P., James, N.P., 2000. Precambrian Carbonates: Evolution of Understanding. In: Carbonate Sedimentation and Diagenesis in the Evolving

Precambrian World: SEPM, Special Publication 67, 3-20.

Guo, Q., Strauss, H., Schröder, S., Gutzmer, J., Wing, B.A., Baker, M.A., Kaufman, A.J., Kim, S.T., and Farquhar, J., 2009. Reconstructing Earth's surface oxidation across the Archean-Proterozoic transition. Geology 37, 399-402.

Habicht, K.S., Gade, M., Thamdrup, B., Berg, P, Canfield, D. 2002. Calibration of sulfate levels in Archaean Ocean. Science 298, 2372-2374.

Haines, P.W., Mory, A.J., Stevens, M.K., Ghori, K.A.R., 2004. GSWA Lancer 1 well completation report (basic data), Officer and Gunbarrel Basins: Western Australia Geologycal Survey, Record 2004/10.

Hardie, L.A., Lowenstein, T.K., Spencer, R.J., 1985. The problem of distinguishing between primary and secondary features in evaporites. In: Sixth Symposium on Salt: Alexandria, Virginia, Salt Institute, 11-39.

Hardie, L.A., 1996. Secular variation in seawater chemistry: An explanation for the coupled variation in the mineralogies of marine limestones and potash evaporites over the past 600 my. Geology v. 24, p. 279-283.

Hayes, J.M., Lambert, I.B., Strauss, H., 1992. The sulfur isotopic records. In: Schopf, J.W., Klein, C. (Eds.), The Proterozoic Biosphere: A multidisciplinary Study. Cambridge University Press, Cambridge, 129-132.

Hill, A.C., Arouri, K., Gorjan, P., Walter, M.R., 2000a. Geochemistry of marine and nonmarine environments of a Neoproterozoic cratonic carbonate/evaporite: The Bitter Springs Formation, Central Australia. Society for Sedimentary Geology Special Publication v. 67, p. 327-344.

Hill, A.C., Cotter, K.L., Grey, K., 2000b. Mid-Neoproterozoic biostratigraphy and isotope stratigraphy in Australia. Precambrian Research v. 100, p. 281-298.

Hill, A.C., Walter, M.R., 2000. Mid-Neoproterozoic (~830-750 Ma) isotope stratigraphy of Australia and global correlation. Precambrian Research v. 100, p. 181-211.

Holland, H.D., 1978. The chemistry of the atmosphere and oceans: John Wiley and Sons Inc. (Eds.), New York.

Holland, H.D., 1984. The Chemical Evolution of the Atmosphere and Oceans. Princeton Univ. Press, Princeton, NJ.

Holland H. D. (2009) Why the atmosphere became oxygenated: A proposal. Geochimica Cosmochimica Acta 73, 5241-5255.

Holser, W.T., 1966. Bromide geochemistry on salt rocks. In: Rau, J.L. (Ed.), Second Symposium on salt. Northern Ohio Geological Society, 248-275.

Horita, J., Zimmerman, H., Holland, H.D., 2002. Chemical evolution of seawater during the Phanerozoic: Implications from the record of marine evaporites. Geochimica Cosmochimica Acta, v. 66, p. 3733-3756.

Hurtgen, M. T., Arthur, M. A., Prave, A. R., 2004. The sulfur isotope composition of carbonate-associated sulfate in Mesoproterozoic to Neoproterozoic carbonates from Death Valley, California. In: Amend, J. P., Edwards, K. J., Lyons, T. W.

(Eds.), Sulfur Biogeochemistry: Past and Present. The Geo. Soc. of Amer., Special Paper 379: 177-194.

Hurtgen, M.T., Arthur, M.A., Halverson, G.P., 2005. Neoproterozoic sulfur isotopes, the evolution of microbial sulfur species, and the burial efficiency of sulfides as sedimentary pyrite. Geology 33, 41-44.

Hurtgen, M.T., Halverson, G.P., Arthur, M.A., Hoffman, P.F., 2006. Sulfur cycling in the aftermath of a 635-Ma snowball glaciation: Evidence for a syn-glacial sulfidic deep ocean. Earth and Planetary Science Letters 245, 551-570.

Johnson,W.J., Goldstein, R.H., 1993. Cambrian sea water preserved as inclusions in marine low-magnesium calcite cement. Nature ,v. 362, p. 335-37.

Kah, L. C., Lyons, T.W., Frank, T.D., 2004. Low marine sulfate protracted oxygenation of the Proterozoic biosphere. Nature, v. 431, p. 834-838.

Kampschulte, A., Strauss, H., 2004. The sulfur isotopic evolution of Phanerozoic seawater based on the analysis of structurally substituted sulfate in carbonates. Chemical Geology 204, 255-286.

Kovalevych, V.M., Marshall, T., Peryt, T.M., Petrychenko, O.Y., Zhukova, S., 2006a. Chemical composition of seawater in Neoproterozoic: Results of fluid inclusion study of halite from Salt Range (Pakistan) and Amadeus Basin (Australia). Precambrian Research 144, 39-51.

Kovalevych, V.M., Marshall, T., Peryt, T.M., Petrychenko, O.Y., Zhukova, S., 2005. Chemical composition of seawater in Neoproterozoic: Results of fluid inclusion study of halite from Salt Range (Pakistan) and Amadeus Basin (Australia). Precambrian Research, v. 144, p. 39-51.

Kwong, M.H., 1995. Salinity and stable isotope constraints for the composition of Devonian seawater, evidence from marine calcite cement sequences in Upper Devonian reef complexes, Canning Basin, Western Australia. M.Sc. thesis, University of Texas at Austin, p. 140.

Lear, C.H., Elderfield, H., Wilson, P.A., 2000. Cenozoic deep-sea temperatures and global ice volumes from Mg/Ca in benthic foraminiferal calcite. Science, v. 287, p. 269-272.

Lindsay, J.F., 1987. Upper Proterozoic evaporites in the Amadeus basin, central Australia, and their role in basin tectonics. Geological Society of American Bulletin 99, 852-865.

Lindsay, J.F., Korsch, R.J., 1989. Interplay of tectonics and sea-level changes in basin evolution: an example from the intracratonic Amadeus Basin, central Australia. Basin Rsearch 2, 3-25.

Lindsay, J.F., Leven, J.H., 1996. Evolution of a Neoproterozoic to Paleozoic intracratonic setting, Officer Basi, South Australia. Basin Research 8, 403-424.

Lo Forte, G.L., Ortí, F., Rosell, L., 2005. Isotopic characterization of Jurassic evaporites. Aconcagua-Neuquén Basin, Argentina. Geologica Acta 3, 155-161.

Longinelli, A., 1989. Oxygen-18 and sulphur-34 in dissolved oceanic sulphate and phosphate. In: Fritz, P., Fontes, J.Ch. (Eds.), Handbook of Environmental Isotope Geochemistry, vol. 3, Elsevier, Amsterdam, 219-255.

Lowenstein, T.K., Hardie, L.A., 1985. Criteria for the recognition of salt-pan evaporites. Sedimentology, v. 32, p. 627-644.

Lowenstein, T.K., Timofeeff, M.N., Brennan, S.T., Hardie, L.A., Demicco, R.V., 2001. Oscillations in Phanerozoic Seawater Chemistry: Evidence from Fluid Inclusions. Science, v. 294, p. 1086-1088.

Lowenstein, T.K., Hardie, L.A., Timofeeff, M.N, Demicco, R.V., 2003. Secular variation in seawater chemistry and the origin of calcium chloride basinal brines. Geology, v. 31, p. 857-860.

Lowenstein, T.K., Timofeeff, M.N., Kovalevych, V.M., Horita, J., 2005. The major-ion composition of Permian seawater. Geochimica Cosmochimica Acta, v. 69, p. 1701-1719.

Lyons, T.W., 2008. Ironing out ocean chemistry at the dawn of animal life. Science 321, 923-924.

Lyons, T.W., Gellatly, A.M., McGoldrick, P.J., Kah, L.C., 2006. Proterozoic sedimentary exhalative (SEDEX) deposits and links to evolving global ocean chemistry. Geological Society of America Memoir 198, 169-184.

Marenco, P.J., 2007. Sulfur isotope geochemistry and the End Permian mass extinction. Dissertation Thesis, University of Southern California, Los Angeles, 189 pp.

Marenco, P.J., Corsetti, F.A., Hammond, D.E., Kaufman, A.J., Bottjer, D.J., 2008. Oxidation of pyrite during extraction of carbonate associated sulfate. Chemical Geology 247, 124-132.

McArthur, J.M., Benmore, R.A., Coleman, M.L., Soldi, C., Yeh, H.W., O'Brien, G.W., 1986. Stable isotopic characterization of francolite formation. Earth and Planetary Science Letters 77, 20-34.

McCaffrey, M.A., Lazar, B., Holland, H.D., 1987. The evaporation path of seawater and coprecipitation of Br^- and K^+ with halite. Journal Sedimentary Petrology 57, 928-937.

Moretto, R., 1988. Observation on the incorporation of trace elements in halite of Oligocene salt beds, Bourg-en-Bresse Basin. Geochimica et Cosmochimica Acta 53, 2809-2814.

Myers, J.S., Shaw, R.D., Tyler, I.M., 1996. Tectonic evolution of Proterozoic Australia: Tectonics 10, 1431-1446.

Paytan, A., Kastner, M., Campbell, D., Thiemens, M.H., 1998. Sulfur isotope composition of Cenozoic seawater sulfate. Science 282, 1459-1462.

Paytan A., Kastner M., Campbell D., and Thiemens M.H. (2004) Seawater sulfur isotope fluctuations in the Cretaceous. Science 304, 1663-1665.

Paytan A., and Gray E.T., 2012. Sulfur isotope stratigraphy, in: Gradstein, F., Ogg, J., Schmitz, M., Ogg, G.), The Geologic Time Scale 2012, Elsevier, New York.

Planavsky N. J., McGoldrick P., Scott C. T., Li C., Reinhard C. T., Kelly A. E., Chu X., Bekker A., Love G. D., and Lyons T. W. (2011) Widespread iron-rich conditions in the mid-Proterozoic ocean. Nature 477, 448-451.

Pope, M.C, Grotzinger, J.P., 2003. Paleoproterozoic Stark Formation, Athapuscow Basin, Northwest Canada: Record of cratonic-scale salinity crisis. Journal ofSedimentary Research 73, 280-295.

Poulton S. W. and Canfield D. E. (2011) Ferruginous conditions: A dominant feature of the ocean through Earth's history. Elements 7, 107-112.

Preiss, W.V., 2000. The Adelaide Geosyncline of South Australia and its significance in Neoproterozoic continental reconstruction. Precambrian Research, 100, 21-63.

Prokoph, A., Shields, G.A., Veizer, J., 2007. Compilation and time-series analysis of a marine carbonate delta O-18, delta C-13, Sr-87/Sr-86 and delta S-34 database through Earth history. Earth-Science Reviews 87, 113-133.

Raab, M., Spiro, B., 1991. Sulfur isotopic variations during seawater evaporation with fractional crystallization. Chemical Geology 86, 323-333.

Rasmussen B., Fletcher I. R., Bekker A., Muhling J. R., Gregory C. J., and Thorne A. M. (2012) Deposition of 1.88-billion-year-old iron formations as a consequence of rapid crustal growth. Nature 484, 498-501.

Ries, J.B., Fike, D.A., Pratt, L.M., Lyons, T.W., Grotzinger, J.P., 2009. Superheavy pyrite ($\delta^{34}S_{pyr}$ > $\delta^{34}S_{CAS}$) in the terminal Proterozoic Nama Group, southern Namibia: A consequence of low seawater sulfate at the dawn of animal life. Geology 37, 743-746.

Risacher, F., Clement, A., 2001. A computer program for the simulation of evaporation of natural waters to high concentration. Computers & Geosciences 27, 191-201.

Sandberg, P.A., 1983. An oscillating trend in Phanerozoic non-skeletal carbonate mineralogy. Nature 305, 19-22.

Sanford, W.E., Wood, W.W., 1991. Brine evolution and mineral deposition in hydrologically open evaporite basins. American Journal of Science 291, 687-710.

Shaw, R.D., Etheridge, M.A., Lambeck, K., 1991. Development of the late Proterozoic to mid-Paleozoic, intracratonic Amadeus basin in central Australia: A key to understanding tectonic forces in plate interiors: Tectonics 10, 688-721.

Shen, Y., Buick, R., Canfield, D.E., 2001. Isotopic evidence for microbial sulphate reduction in the early Archaean era. Nature 410, 77-81.

Shen, Y., Canfield, D.E., and Knoll, A.H., 2002. Middle Proterozoic ocean chemistry: Evidence from the McArthur Basin, Northern Australia. American Journal of Science, v. 302, p. 81-89.

Shen, B., Xiao, S. Kaufman, A.J., Bao, H. Zhou, C. Wang, H., 2008. Stratification and mixing of a post-glacial Neoproterozoic ocean: Evidence from carbon and sulfur isotopes in a cap dolostone from northwest China. Earth and Planetary Science Letters, 265. 209-228.

Shields, G.A., Strauss, H., Howe, S.S., Siegmund, H., 1999. Sulphur isotope compositions of sedimentary phosphorites from the basal Cambrian of China – implications for Neoproterozoic-Cambrian biogeochemical cycling. Journal of the Geological Society 156, 943-955.

Siemann, M.G., 2003. Extensive and rapid changes in seawater chemistry during the Phanerozoic: evidence from Br contents in basal halite. Terra Nova 15, 243-248.

Sim M.S., Bosak T., and Ono S. (2011) Large sulfur isotope fractionation does not require disproportionation. Science 333, 74-77.

Simeonova, A.P., Iasky, R.P., 2005. Seismic mapping, salt deformation, and hydrocarbon potential of the central western Officer Basin, Western Australia: Western Australia Geological Survey, Report 98.

Solomon, M., Rafter, T.A., Dunham, K.C., 1971. Sulfur and oxygen isotope studies in the northern Pennines in relation to ore genesis. Transactions of the Institute of Mining and Metallurgy 80, 259-275.

Spear, N., Holland, H.D., Garcia-Veígas, J., Lowenstein, T.K., Giegengack, R. Peters, H., 2012. Evidence from fluid inclusions extends the record of seawater chemistry by ~300 million years from ~544 Ma to 830 Ma. Submitted, Geology

Stanley, S.M., Hardie, L.A., 1998. Secular oscillations in the carbonate mineralogy of reef-building and sediment-producing organisms driven by tectonically forced shifts in seawater chemistry. Paleogeography, Paleoclimatology, Paleoecology 144, 3-19.

Stevens, M.K., Apak, S.N., 1999. GSWA Empress 1 and 1A Well Completion Report, Yowalga Sub-basin, Officer Basin, Western Australia. Western Australia Geological Survey, Record 1999/4.

Thode, H.G., Monster, J., 1965. Sulfur-isotope geochemistry of petroleum, evaporites, and ancient seas. American Association Petroleum Geologist, Memories 4, 367- 377.

Timofeeff, M.N., Lowenstein, T.K., Blackburn, W.H., 2000. ESEM-EDS: An improved technique for major element chemical analysis of fluid inclusions. Chemical Geology 164, 171-182.

Timofeeff, M.N., Lowenstein, T.K., Martins da Silva, M.A, Harris, N.B., 2006. Secular variation in the major-ion chemistry of seawater: Evidence from fluid inclusions in Cretaceous halites. Geochimica Cosmochimica Acta, 70,1977-1994.

Townson, W.G., 1985. The subsurface geology of the western Officer Basin: Results of Shell's 1980-1984 petroleum exploration campaign. The APEA Journal 25, 34-51.

Utrilla, R., Pierre, C., Ortí, F., Pueyo, J.J., 1992. Oxygen and sulphur isotope composition as indicators of the origin of Mesozoic and Cenozoic evaporites from Spain. Chemical Geology 102, 229-244.

Valyashko, M.G., 1956. Geochemistry of bromine in the processes of salt deposition and the use of the bromine content as a genetic and prospecting criterion. Geochemistry 6, 570-589.

Vinogradov, V.I., 2007. Was there a conflict at the Neoproterozoic-Cambrian boundary: evidence from sulphur isotope composition? Lithology and Mineral Resources 42, 1-14.

Walter, M.R., Hill, A.C., 1999. Isotope Geochemical Sampling of Drillhole Empress-1A (unpublished report). Geological Survey of Western Australia file report, S2042, A7.

Walter, M.R., Veevers, J.J., Calver, C.R., Grey, K., 1995. Neoproterozoic stratigraphy of the Centralian Superbasin, Australia. Precambrian Research 73, 173-195.

Ward, W.B., 1996. Evolution and diagenesis of Frasnian carbonate platforms, Devonian reef complexes, Napier Range, Canning Basin, Western Australia, Ph.D. dissertation, State University of New York at Stony Brook, p. 540.

Wells, A.T., Forman, D.J., Ranford, L.C., Cook, P.J., 1970. Geology of the Amadeus Basin, Central Australia. Bureau of Mineral Resources, Australia, Bulletin 100.

Wingate, M.T.D., Campbell, I.H., Compston,, W., Gibson, G.M., 1998. Ion microprobe U-Pb ages for Neoproterozoic basaltic magmatism in south-central Australia and implications for the breakup of Rodinia. Precambrian Research 87, 135-159.

Wortmann, U.G., Paytan, A., 2012. Rapid variability of seawater chemistry over the past 130 Million Years. Science 337, 334-336.

Yanagisawa, F., Sakai, H., 1983. Thermal decomposition of barium sulfate-vanadium pentaoxide-silica glass mixture for preparation of sulfur dioxide in sulfur isotope ratio measurements. Analytical Chemistry 55, 985-987.

Young, I.F., Ambrose, G.J., 2007. Petroleum geology of the southeastern Amadeus Basin: the search for sub-salt hydrocarbons. In: Munson, T.J. and Ambrose, G.J. (Editors), Proceedings of the Central Australian Basins Symposium (CABS), Alice Springs, Northern Territory, 2005. Northern Territory Geological Survey, Special Publication nº2, 183-204.

INDEX